Response surface modelling and investigation into release kinetics and *in vivo* toxicity of nanocellulose-based slow-release devices for delivery of quercetin

by
Hannah Keirsgieter

Thesis presented in partial fulfilment of the requirements for the degree of Master of Science in Engineering (Biomedical) in the Faculty of Engineering at Stellenbosch University

Supervisor: Prof Annie Chimphango
Co-supervisor: Prof Carine Smith

December 2022

Declaration

By submitting this thesis electronically, I declare that the entirety of the work contained therein is my own, original work, that I am the sole author thereof (save to the extent explicitly otherwise stated), that reproduction and publication thereof by Stellenbosch University will not infringe any third-party rights and that I have not previously in its entirety or in part submitted it for obtaining any qualification.

Date: November 2022

Abstract

The delivery of many anti-inflammatory and anti-cancer drugs is hindered due to their low solubility in water, leading to poor bioavailability and therapeutic efficacy. The high specific surface area and customisable properties of nanoscale materials have established them as innovative solutions in many biomedical applications, such as wound healing, tissue engineering and drug delivery. Nanocellulose (NC) in particular is of special interest as a drug carrier, due to its inherent biocompatibility, biodegradability, and low toxicity. This study focused on cellulose nanocrystals (CNC) and nanofibres (CNF), as potential drug delivery systems (DDSs) for slow-release of the model hydrophobic drug, quercetin. NC is naturally hydrophilic and anionic, and was therefore first modified with the cationic surfactant, cetyltrimethylammonium bromide (CTAB), in order to facilitate effective drug binding through hydrophobic interaction. The effect of surfactant and drug concentration on particle size (Z), polydispersity index (PdI), zeta potential (ζ) and binding efficiency (BE) was investigated by response surface methodology (RSM), an empirical modelling technique in parametric optimisation. A design of experiments (DOE) approach was taken to obtain the experimental data, through a full factorial design (FFD), followed by a central composite design (CCD). The regressed Z and PdI models for both designs reported R^2 values < 75%, while the ζ and BE models reported mean R^2 values of 78% and 90%, respectively, indicating good model fits. The optimal responses for CNC were reported as Z = 5436 nm, PdI = 0.56, ζ = – 18.3 mV, and BE = 76.9%, at a CTAB and quercetin concentration of 3.3 mM and 4.2 mg/mL, respectively. The optimal responses for CNF were reported as Z = 4183 nm, PdI = 0.56, ζ = – 14.3 mV, and BE = 80.8%, at a CTAB and quercetin concentration of 2.0 mM and 5.1 mg/mL, respectively. Design validation resulted in experimental errors of 18.2% for CNC and 9.9% for CNF. Characterisation of the DDSs was performed by dynamic light scattering (DLS) using a Malvern Zetasizer, and further investigation into particle morphology was carried out by scanning electron microscopy (SEM). The *in vitro* quercetin release profile of a CNC-CTAB-QT formulation was tested using the dialysis bag method, and best fitted by the Korsmeyer-Peppas model (R^2 = 99.9%), with a release exponent $n > 1$ suggesting super case II (non-Fickian) transport. In the first hour, the DDS exhibited a delayed cumulative release of 29%, compared to the cumulative release of 62% by the free drug. The *in vivo* safety profile of this formulation was evaluated by performing a toxicity assay on zebrafish larvae, but was constrained by excessive aggregation in the incubation medium.

Opsomming

Die lewering van talle anti-inflammatoriese en anti-kankermiddele word verhinder deur hul lae oplosbaarheid in water, wat tot swak biobeskikbaarheid en terapeutiese doeltreffendheid lei. Die hoë spesifieke oppervlakte en pasmaakbare eienskappe van nanoskaalmateriale beteken dat hulle innoverende oplossings in talle biomediese toepassings, soos wondgenesing, weefselontwikkeling en middellewering, is. Nanosellulose is spesifiek van belang as 'n middeldraer weens die inherente bioversoenbaarheid, bio-afbreekbaarheid en lae toksisiteit daarvan. Hierdie studie het gefokus op sellulose nanokristalle (SNK) en sellulose nanovesels (SNV) as moontlike middelleweringstelsels (MLS'e) vir stadige vrystelling van die model- hidrofobiese middel kwersetien. Nanosellulose is van nature hidrofilies en anionies, en is dus eerste met die kationiese surfaktant setieltrimetielammoniumbromied (STAB) gemodifiseer om doeltreffende middelbinding deur hidrofobiese interaksie in die hand te werk. Die uitwerking van surfaktant- en middelkonsentrasie op deeltjiegrootte (Z), polidispersiteitsindeks (PdI), zeta-potensiaal (ζ) en bindingdoeltreffendheid (BD) is met behulp van responseoppervlakmetodologie, 'n empiriese modelleringstegniek in parametriese optimering. 'n Eksperimentontwerptegniek word toegepas om die eksperimentele data te verkry, deur 'n volledige faktoriale ontwerp, gevolg deur 'n sentrale saamstellingsontwerp. Die geregresseerde Z en PdI modelle vir albei ontwerpe het R^2 waardes < 75% gelewer, terwyl die ζ en BD modelle gemiddele R^2 waardes van onderskeidelik 78% en 90% gelewer het, wat goeie modelpassings toon. Die optimale response vir SNK was Z = 5436 nm, PdI = 0.56, ζ = – 18.3 mV en BD = 76.9% teen 'n STAB- and kwersetien-konsentrasie van onderskeidelik 3.3 mM en 4.2 mg/mL. Die optimale response vir SNV was Z = 4183 nm, PdI = 0.56, ζ = – 14.3 mV en BD = 80.8% teen 'n STAB- and kwersetien-konsentrasie van onderskeidelik 2.0 mM en 5.1 mg/mL. Ontwerpbekragtiging het gelei tot eksperimentele foute van 18.2% vir SNK en 9.9% vir SNV. Karakterisering van die MLS'e is uitgevoer deur dinamiese ligverstrooiing met behulp van 'n Malvern Zetasizer, en verdere ondersoek na deeltjiemorfologie is deur skanderingselektronmikroskopie uitgevoer. Die *in vitro*-kwersetien-vrystellingsprofiel van 'n SNK-STAB-QT-formulering is met die dialisesakmetode getoets, en was die beste passing vir die Korsmeyer-Peppas-model (R^2 = 99.9%), met 'n vrystellingseksponent van $n > 1$ wat supergeval II (nie-Fickiaanse) transport aan die hand doen. In die eerste uur het die MLS 'n vertraagde kumulatiewe vrystelling van 29% getoon, in vergelyking met die kumulatiewe vrystelling van 62% deur die vrye middel. Die *in vivo*-veiligheidsprofiel van hierdie formulering is geëvalueer deur die uitvoer van 'n toksisiteitstoets op sebravis-larwes, maar is deur uitermatige klomping in die inkubasiemedium beperk.

Acknowledgements

Firstly, I would like to say an endless thank you to my family and parents, Annalise Zemlin and Hein Keirsgieter, not only for this academic opportunity, but for their continuous love and support throughout my studies.

A special feeling of gratitude to my mother, you inspire me every day and I would not have journeyed down this road if it were not for you.

The warmest of thanks to my brother, Wim, who I would be lost without. Thank you for all the laughter and encouragement, that carried me through good times and bad.

I would like to thank my supervisor, Prof Annie Chimphango from the Department of Process Engineering, for her critique and guidance over the last two years.

Also, to my co-supervisor, Prof Carine Smith from the Department of Clinical Pharmacology at The Faculty of Medicine and Health Sciences, Tygerberg Campus, thank you for your knowledge and support.

Lastly, I would like to extend my appreciation to the following people, for their assistance and contribution to this study:

- The analytical staff (Mr Jaco van Rooyen, Mrs Hanlie Botha) and the technical staff (Mr Alvin Peterson, Mr Oliver Jooste) from the Process Engineering Department, for their help with analysis and instrumentation, respectively.
- Mrs Madelaine Frazenburg, Mrs Lize Engelbrecht, and Dr Alicia Botes from the Central Analytical Facility, for all their assistance with SEM analysis.
- Friends and colleagues, for their support, motivation and friendship!

Table of Contents

List Of Figures

List Of Tables

List Of Abbreviations

ADME	Absorption, distribution, metabolism and excretion
AFM	Atomic force microscopy
ANOVA	Analysis of variance
BBB	Blood-brain barrier
BE	Binding efficiency
BNC	Bacterial nanocellulose
CAF	Central analytical facilities
CCD	Central composite design
CMC	Critical micelle concentration
CNC	Cellulose nanocrystals
CNF	Cellulose nanofibrils
CrI	Crystallinity index
CTAB	Cetyltrimethylammonium bromide
DDS	Drug delivery system
DLS	Dynamic light scattering
DMSO	Dimethyl sulfoxide
DOE	Design of experiments
DS	Degree of substitution
ELS	Electrophoretic light scattering
EPR	Enhanced permeation and retention
FFD	Full factorial design
FT-IR	Fourier transform infrared
HCl	Hydrochloric acid
HLB	Hydrophilic-lipophilic balance
hpf	Hours post fertilisation
HPLC	High performance liquid chromatography
H_2SO_4	Sulphuric acid
ICP-MS	Inductively coupled plasma mass spectrometry
ISO	International standards organisation
LbL	Layer-by-layer
MCC	Microcrystalline cellulose
MEC	Minimum effective concentration

MTC	Minimum toxic concentration
MWCO	Molecular weight cut off
NC	Nanocellulose
NMR	Nuclear magnetic resonance
NP	Nanoparticle
NSAID	Non-steroidal anti-inflammatory drug
OECD	Organisation for Economic Co-operation and Development
OFAT	One-factor-at-a-time
PC	Protein corona
PdI	Polydispersity index
PEG	Polyethylene glycol
PLA	Polylactic acid
PTU	1-Phenyl 2-Thiourea
PVA	Poly(vinyl alcohol)
QT	Quercetin
RES	Reticuloendothelial system
rpm	Revolutions per minute
RSM	Response surface methodology
SDS	Sodium dodecyl sulphate
SEM	Scanning electron microscopy
TEM	Transmission electron microscopy
TEMPO	2,2,6,6-tetramethylpiperidine-1-oxyl
TIRF	Total Internal Reflection Fluorescence
US	United States
XRD	X-ray diffraction

Chapter 1: Introduction

1.1 Background

A rapidly growing field of research in biotechnology and nanomedicine is devoted towards improving the therapeutic performance of drug delivery systems (DDSs) (Hasan et al., 2020). As of 2006, drug delivery had dominated as much as 76% of all scientific papers in the field of nanomedicine (Wagner et al., 2006), and has continued growing. Limitations of conventional DDSs (e.g. tablets, capsules, ointments, syrups) include poor absorption from the site of administration, low drug bioavailability, high first-pass metabolism and premature excretion from the body (Adepu & Ramakrishna, 2021). Controlled DDSs are developed to improve drug bioavailability and target specificity, and provide protection from chemical/enzymatic hydrolysis, all while releasing the drug in a controlled or defined manner (Adepu & Ramakrishna, 2021). By having control over the therapeutic window of the drug in this manner, better patient compliance together with improved drug safety and effectiveness can be achieved.

A common challenge in the delivery of non-steroidal anti-inflammatory drugs (NSAIDs) is their low water solubility and their too-rapid release (Gericke, Schulze & Heinze, 2020). Nanoscale materials can be engineered to carry and transport these drugs, increasing their bioavailability and circulation time, and facilitating slow-release kinetics. Nanoparticles (NPs) can carry up to 45% of their weight in a particular drug, with an entrapment efficiency of over 95% (Siepmann & Siepmann, 2009). Encapsulation or adsorption protects the drug until its release, allowing the physiochemical properties of the DDS rather than the drug to determine its fate in the body (Siepmann & Siepmann, 2009).

Environmental and socio-economic issues are forcing companies and governments to promote sustainable practices by using cost-effective and renewable resources (Yahya et al., 2019). Natural polymers are of special interest in biomedicine, due to their inherent biocompatibility, biodegradability, low toxicity and widespread availability (Pachuau, 2017; Lunardi et al., 2021). Cellulose is the most abundant carbohydrate in nature, making up over 1.5 trillion tons of the world's total annual biomass production (Moon et al., 2016). Moreover, it is one of the main components present in waste-paper sludge generated by pulp and paper mills (Dwiarti et al., 2012). The paper industry in South Africa generates half a million dry tons of waste-paper sludge annually, with a high moisture content raising the cost of disposal and driving companies to search for green alternatives (Bester, 2018).

Cellulosic nanomaterials have already been established as an effective low-cost and renewable resource in the fields of food packaging, electronics, textiles, surface coatings and water treatment (Moon et al., 2011; Deepa et al., 2015; Khine & Stenzel, 2020). However, in recent years, there has been significant scientific interest in the modification of nanocellulose (NC) for a variety of biomedical applications, including tissue engineering, wound healing, medical implants and drug delivery (Dufresne, 2013; Raghav, Sharma & Kennedy, 2021; Das, Ghosh & Sarkar, 2022). NC materials have distinctive properties that make them ideal candidates for drug delivery, such as their high surface-to-volume ratio, aiding in cellular binding and uptake, and their abundant surface hydroxyl groups, allowing for functionalisation and modification (Kupnik et al., 2020).

This study focused on cellulose NPs, in the form of nanocrystals (CNC) and nanofibrils (CNF), as potential carrier systems for slow-release of the anti-inflammatory plant flavanol and model hydrophobic drug, quercetin. As NC is naturally hydrophilic and quercetin is hydrophobic, modification with an amphiphilic surfactant is necessary for effective drug loading (Abitbol, Marway & Cranston, 2014). This was achieved using cetyltrimethylammonium bromide (CTAB), a quaternary ammonium salt with a cationic hydrophilic head and a hydrophobic alkyl chain tail. The formulated DDSs were characterised using spectrophotometric methods and microscopic imaging, and response surface methodology (RSM) was used to investigate the effect of surfactant and drug concentration on particle morphology and drug binding efficiency. Moreover, the *in vitro* release kinetics and *in vivo* safety profile were studied through use of the dialysis bag method and zebrafish model, respectively.

1.2 Problem statement

Quercetin, one of the most abundant plant flavonoids, found in many common fruits and vegetables, has been shown to possess desirable biological and pharmaceutical activity, such as anti-oxidant, anti-inflammatory, anti-anaemia, anti-anaphylaxis and even anti-cancer effects (Hollman & Katan, 1999). However, the clinical application of quercetin is heavily restricted, due to its low solubility that leads to minimal absorption in the gastrointestinal tract (Li et al., 2009). In fact, its oral bioavailability has been reported to be less than 17% in rats (Khaled, El-Sayed & Al-Hadiya, 2003), and less than 1% in humans (Gugler, Leschik & Dengler, 1975). Therefore, an effective nanoformulation for the transportation of quercetin is desirable, to facilitate sufficient absorption and allow pharmaceutical action to take place (Khursheed et al., 2020).

The role that NC materials are carving out amongst other popular biopolymers, such as polylactic acid (PLA), chitosan and alginate, is still relatively undefined. An exploratory and comparative analysis of the two most common cellulosic nanofibres in terms of physiochemical characterisation, release kinetics modelling and evaluation of *in vivo* toxicity could provide useful insight for developing a suitable DDS for the release of hydrophobic anti-inflammatory and anti-cancer drugs. Furthermore, response surface visualisation and optimisation of drug and surfactant concentration for measurable response variables, by means of RSM and design of experiment (DOE) techniques, could help improve the efficiency of existing NP preparation methods.

Both CNC and CNF have been widely studied as potential drug carriers, prepared in various formulations with several different copolymers, surfactants and model drugs (Pachuau, 2017; Hasan et al., 2020; Khine & Stenzel, 2020; Kupnik et al., 2020; Lunardi et al., 2021; Raghav et al., 2021). Although there are a few studies that have focused on the modification of NC materials with CTAB (Padalkar et al., 2010; Abitbol et al., 2014; Alila et al., 2005; Syverud et al., 2011; Xhanari et al., 2011), particularly for the loading of hydrophobic drugs (Jackson et al., 2011; Qing et al., 2016; Zainuddin et al., 2017; Raghav et al., 2020; Gupta & Raghav, 2020), there is a paucity of studies that employ quercetin (Li et al., 2019; Liu et al., 2021). Moreover, zebrafish as an *in vivo* model have only in the recent decade been established as an effective intermediate step between *in vitro* and conventual rodent testing (Lee et al., 2017; Sieber et al., 2019), and contributing work towards this field of research might help it gain acceptance in the scientific community.

1.3 Research questions

The following were identified as key research questions of the study:

- How suitable are CNC and CNF for quercetin drug delivery?
- How do CTAB and quercetin affect particle size, surface charge, polydispersity and binding efficiency, and what is their interaction with NC?
- How does the effect of CTAB and quercetin differ between CNC and CNF?
- What are the predicted process conditions for optimal binding of quercetin onto CNC and CNF and the formation of uniform, stable DDSs?
- What release model best describes the bound drug release kinetics of the developed DDS, and how do they compare to that of the free drug?
- What is the exhibited *in vivo* safety profile of the DDS in zebrafish?

1.4 Aim and objectives

The aim of this study was to develop, characterise, and investigate the parametric effect of synthesis variables during the production of NC-based DDSs for delivery of quercetin, as well as further investigate the *in vitro* release kinetics and *in vivo* toxicity.

The following were the objectives of the study:

1. Investigate the effect of surfactant and drug concentration on particle morphology (size, charge, dispersity) and drug binding efficiency, by modelling and optimisation of the response surfaces using DOE methodology
2. Modify and characterise nanocellulose for the binding and release of quercetin
3. Investigate and model quercetin *in vitro* release kinetics from the NC DDSs by fitting zero-order, first-order, Higuchi and Korsmeyer-Peppas models
4. Evaluate the *in vivo* toxicity of the DDS using the zebrafish model

1.5 Thesis outline

Chapter 1: Introduces the background and problem statement, as well as the main aims, objectives and research questions of the study.

Chapter 2: Presents literature findings on the preparation and functionalisation of NC, release kinetics models, zebrafish as *in vivo* models, and DOE for process improvement.

Chapter 3: Describes the materials and experimental methodology, as well as the analytical and statistical procedures undertaken during the study.

Chapter 4: Discusses the results and outcomes of the study.

Chapter 5: Summarises general conclusions and recommendations for future work.

Chapter 2: Literature review

2.1 Nanomaterials in medicine

According to Wagner et al., "A global survey of companies pursuing 'nanomedicine' indicates that nanotechnology is taking root in the drug and medical device industry" (Wagner et al., 2006). In the last decade, the diversity of pathological conditions associated with diseases has led to a growing demand for innovative pharmacokinetic solutions (Macchione, Biglione & Strumia, 2018). In 2019, the global pharmaceutical industry was estimated to have spent 83 billion US dollars on the research and development of novel pharmaceutical products (Owida et al., 2022). Nano-sized formulations have been established as exciting candidates for improved therapeutic and diagnostic approaches (Macchione et al., 2018), with applications in tissue engineering, regenerative medicine, implant coatings and drug delivery (Owida et al., 2022).

2.1.1 Drug delivery systems

As discussed in Chapter 1, controlled drug delivery formulations aim to minimise harmful side-effects, while reducing both dosage amount and frequency and maximising therapeutic performance (Siepmann & Siepmann, 2009). Nanomaterials exhibit physiochemical and biological properties different to bulk or molecular materials with the same composition, with high specific surface areas that make them ideal for drug delivery (Kupnik et al., 2020). Despite their many advantages, nanomaterials still present challenges surrounding their toxicity, biodistribution, accumulation, and clearance (Pachuau, 2017).

Metal/metal-oxide and silica NPs, as well as carbon nano-tubes are examples of inorganic nanomaterials, whereas biopolymers (polysaccharides, DNA, proteins) and synthetic polymers (polylactide, polyvinylchloride, polyethyleneglycol) are examples of organic nanomaterials (Gericke et al., 2020). Polysaccharides, in particular, have an advantage over artificial NPs in that they are inherently nontoxic, biocompatible and often exhibit desirable bioactivities (Pachuau, 2017; Gericke et al., 2020). Adepu & Ramakrishna published an extensive review on the current status and future of controlled DDSs, and provide detailed descriptions of the different types of nanocarrier systems, including liposomes, dendrimers, micelles, exosomes, polymersomes, nanospheres, nanocapsules, nanoemulsions, solid-lipid NPs, and hydrogels (Adepu & Ramakrishna, 2021). NC formulations are a class of polymeric, polysaccharide DDSs, and their various methods of preparation and structures are discussed in Section 2.2.1.

Research in drug delivery is an interdisciplinary effort, and has resulted in the interesting finding that a non-spherical NP geometry has many advantages over a spherical geometry in the cellular uptake, biodistribution and biological activity of a developed DDS (Pachuau, 2017; Khine & Stenzel, 2020). Non-spherical nanocarriers, such as elongated liposomes or carbon nanotubes, have been reported to exhibit prolonged circulation in the body and delayed clearance (Simone, Dziobla & Muzykantov, 2008). In fact, it has been shown that polymeric micelles of flexible filament types exhibit a circulation time up to 10 times longer and an increased cellular uptake in comparison to their spherical counterparts (Geng et al., 2007). This discovery coupled with the high specific surface area of NC inspired research into novel cellulosic DDSs (Pachuau, 2017).

2.1.2 Cellulose

Cellulose, the major component of all plant matter (lignocellulosic biomass), is the most abundant renewable, biodegradable and non-toxic carbohydrate available in nature (Crespo et al., 2012). Unprocessed lignocellulose consists of carbohydrate polymers (cellulose and hemicellulose) and an aromatic polymer (lignin), with a ratio of approximately 30–50% cellulose, 20–35% hemicellulose, 10–25% lignin, and the remaining trace elements (Poletto, Ornaghi Júnior & Zattera, 2014). These lignocellulosic components are contained in macrofibrils within the plant cell wall, structured according to Figure 2.1 (Zhang, Yang & Blasiak, 2011).

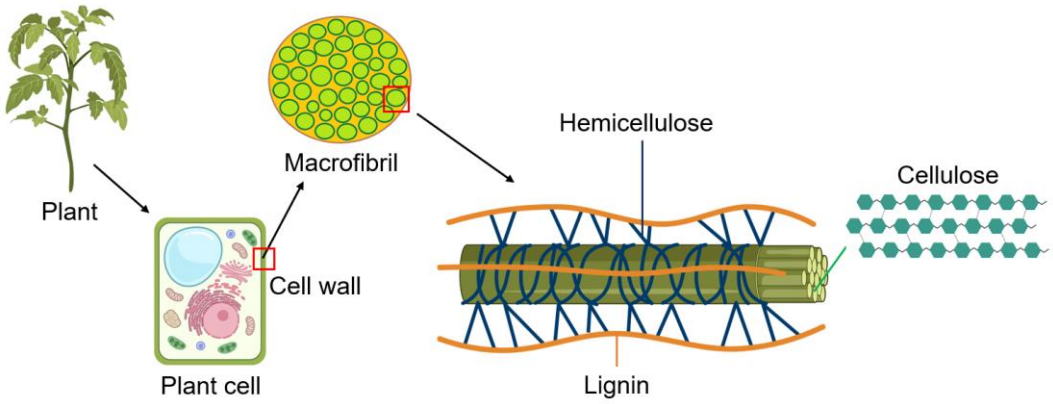

Figure 2.1: Different components of lignocellulose, created with BioRender.com

The microfibrillated cellulose structure is composed of both crystalline and amorphous regions, as well as paracrystalline regions of intermediate crystallinity (Mosier et al., 2005). The degradation rate of amorphous cellulose is much higher than that of crystalline cellulose, and therefore more susceptible to enzymatic or acid hydrolysis

(Mosier et al., 2005). Cellulose is an amphiphilic, linear homo-polysaccharide made up of D-anhydroglucopyranose units, linked by β-(1→4)-glycosidic bonds; the structure of its repeating unit is given in Figure 2.2. A network of hydrogen bonds between hemicellulose and cellulose forms the structural backbone of the plant cell wall (Zhang et al., 2011).

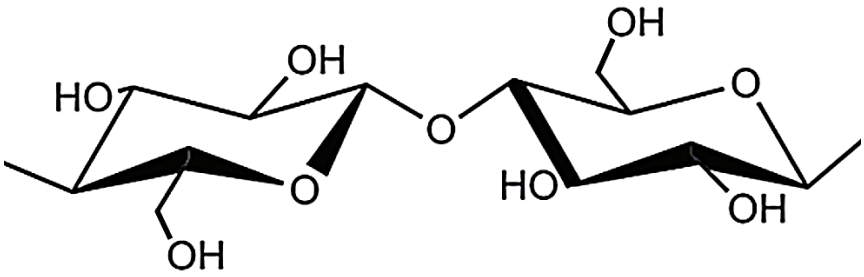

Figure 2.2: Chemical structure of the repeating unit of cellulose, drawn with PowerPoint (Microsoft Office®, 2022)

2.1.3 Nanocellulose

Cellulose is widely used in oral drug delivery as microcrystalline cellulose (MCC) in tablets (Thoorens et al., 2014), but MCC has poor surface area and drug loading in comparison to its nanoscale counterpart (Khine & Stenzel, 2020). Depending on the cellulose source and preparation method, as well as the drying route used, NC can possess a specific surface area above 30 m^2/g (Mautner et al., 2018), whereas the specific surface area of MCC is typically around 1 m^2/g (Ardizzone et al., 1999). As detailed in various reviews (Li et al., 2015; Raghav et al., 2021; Lunardi et al., 2021), NC has unique and desirable biological, chemical, physical and mechanical properties.

In addition to having a high specific surface area and aspect ratio, NC also has numerous surface hydroxyl (-OH) groups, useful for surface modification and functionalisation (Moon et al., 2011). NC itself does not possess any inherent antimicrobial activity, but can be combined with a number of biologically active materials in order to induce this property (Kupnik et al., 2020). Moreover, NC exhibits a particularly low density combined with high mechanical strength and stiffness, resulting in a specific Young's modulus of approximately 65 – 85 J/g in comparison to that of 25 J/g in the case of steel (Poletto et al., 2014). NC can be isolated from many different sources of cellulose, and has successfully been isolated from wood, mulberry pulp, rice husk, kenaf, sugarcane bagasse and cotton (Yahya et al., 2019). There are three main classifications of NC, each with different properties based on their source and preparation method (Deepa et al., 2015): cellulose nanocrystals (CNC), also known as cellulose nanowhiskers or nanocrystalline

cellulose, cellulose nanofibrils (CNF), also known as nanofibrillated cellulose, and bacterial nanocellulose (BNC). The typical dimensions, according to the International Standards Organisation (ISO, 2017), and most common chemical, mechanical, and biological preparation methods for the respective forms of NC are summarised in Table 2.1 (Pachuau, 2017; Khine & Stenzel, 2020; Hasan et al., 2020). Accompanying images depicting the different morphologies NC are provided in Figure 2.3 (Moon et al., 2011).

Table 2.1: Typical dimensions and preparation methods of cellulose nanocrystals (CNC), cellulose nanofibrils (CNF) and bacterial nanocellulose (BNC)

Type of nanocellulose	Preparation method	Diameter (nm)	Length (nm)
CNC	Acid hydrolysis (sulphuric, hydrochloric, hydrobromic, phosphoric) at high temperatures under continuous stirring, followed by dilution in water, centrifugation, and washing with (or dialysis against) water	3 – 50	100 – 4 000
CNF	Enzymatic or chemical pre-treatment (e.g. TEMPO-mediated oxidation) followed by mechanical treatment (high-pressure homogenisation, grinding or sonication)	3 – 100	100 – 100 000
BNC	Static and stirred culturing of bacterial organisms (e.g. *Gluconacetobacter xylinus*) undergoing oxidative fermentation, with saccharides as a carbon source	20 – 100	≥ 1 000

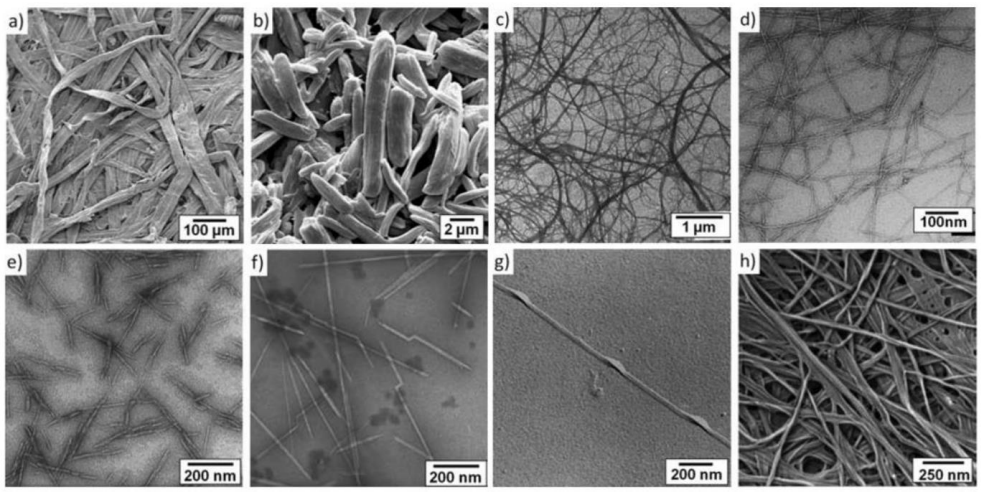

Figure 2.3: (a) Wood fibre, (b) microcrystalline cellulose, (c) microfibrillated cellulose, (d) cellulose nanofibrils, (e) and (f) cellulose nanocrystals, (g) nanocellulose from algae, (h) bacterial nanocellulose. Images reproduced from Moon et al. (2011), with permission from the Royal Society of Chemistry.

Since the amorphous regions of cellulose degrade more readily during acid hydrolysis than the crystalline regions, CNC extracted from plant cellulose are highly crystalline and rod-like, whereas CNF tend to form longer smooth chains of both crystalline and amorphous regions (Lie, Ålander & Lindström, 2017), exhibiting a higher aspect ratio (*L/D*) than both CNC and BNC. BNC exists as a porous, crystalline network, with a high purity in the absence of hemicellulose, lignin or pectin. However, due to the low production rate and high cost of its synthesis, it is considered less commercially feasible compared to mechanical and chemical processes (Moon et al., 2011; Kupnik et al., 2020).

CNC treated with HCl have low colloidal stability due to the abundance of hydroxyl groups on their surface, whereas CNC treated with H_2SO_4 are typically more stable in aqueous suspensions, due to the introduction of sulphate half-ester groups on their surface (Arai, Horikawa & Shikata, 2018), that with a pKa < 7 ionise in neutral suspensions to induce electrostatic repulsion between particles and prevent aggregation (Moon et al., 2011). CNF pre-treated via 2,2,6,6-tetramethylpiperidine-1-oxyl radical (TEMPO)-mediated oxidation are imparted with carboxylic acid groups that can similarly deprotonate to give a negatively charged surface (Khine & Stenzel, 2020). The presence of these functional groups on the NC surface allows for various surface modification techniques (Kupnik et al., 2020), as discussed in Section 2.3.1.

2.2 Polymeric drug delivery systems

Polymeric NPs have been successfully processed into many different forms, such as hydrogels, aerogels, film and foams, as well as complexes, dispersions and emulsions, nanospheres and nanocapsules, self-assembled polymeric micelles and nanofibres (Khine & Stenzel, 2020; Adepu & Ramakrishna, 2021; Lunardi et al., 2021). Kupnik et al. (2020) reviewed key studies published since 2015 that investigated various NC drug delivery formulations, prepared using different approaches and therapeutic agents.

2.2.1 Nanoparticle preparation

Methods of NP preparation are classified as either bottom-up approaches or top-down approaches. The chemical and mechanical methods of producing CNC and CNF (discussed in Section 2.1.3) are top-down approaches, whereas bottom-up approaches include emulsion diffusion, nanoprecipitation and polymerisation induced self-assembly (Wang et al., 2016; Gericke et al., 2020; Zielinska et al., 2020).

The complex rheology of NC has allowed for various applications in hydrogels. With the ability to absorb water, hydrogels are created by cross-linking polymer chains through interactions that can be ionic, physical, or covalent. (Elisseeff, 2008) . Due to their unique display of sol-gel transitions upon environmental changes in temperature, pH and ionic strength, smart polymeric hydrogels (e.g. injectable gels) are frequently used in controlled drug delivery, tissue engineering and regenerative medicine (Jagur-Grodzinski, 2010; Kamaly et al., 2016). Chemically crosslinked hydrogels are irreversible at temperatures sustained by the human body, whereas physically cross-linked hydrogels are held together by reversible non-covalent linkages (Jagur-Grodzinski, 2010).

NC has also been frequently used in solid nanocomposite films, whereby cellulose is incorporated into a matrix of standard material, typically to improve the mechanical and thermal properties of the material (Moon et al., 2011). Common nanocomposite film preparation includes solvent casting, which involves the mixing of a 0.1-1 wt% polymer suspension and an appropriate surfactant followed by water evaporation or freeze-drying, as well as electrospinning and layer-by-layer (LbL) assembly techniques (Dufresne, 2013).

Depending on the charge, size and surface chemistry of the model drug, loading onto the polymeric carrier can be achieved via two common routes, namely covalent binding to or physical entrapment within the polymeric matrix (Akhter et al., 2013; Gericke et al., 2020). Loading can take place either during initial fabrication of the polymeric system, for example mixing of the drug and polymeric mixture prior to electrospinning (Owida et al., 2022), or modification post-fabrication, such as surface adsorption, chemical conjugation or ionic, hydrophobic or host-guest interactions (Khine & Stenzel, 2020). In this study, modification of the CNC and CNF material took place post-fabrication, via adsorption with the surfactant followed by hydrophobic interaction with the model drug.

2.2.2 Surface modification and functionalisation

It is often desirable to engineer NPs with given functionalities, for example to enable biocompatibility and reduce toxicity, minimise identification and uptake by immune system cells, to alter the hydrophobicity, hydrophilicity or surface charge of the dispersion in given solvents, or to control the optical and electrical features of the particle (Soppimath et al., 2001). The abundant hydroxyl groups of native cellulose are convenient for imparting functionality through modification of the surface chemistry (Raghav et al., 2021).

This modification may take place during the initial synthesis, for example, as in the case of the CNC and CNF obtained for this study, whereby sulphate half-ester groups are introduced onto CNC during acid hydrolysis, and carboxylic acid groups are introduced onto CNF during TEMPO-mediated oxidation, producing sulphate and carboxylate anions upon dissociation (Li et al. 2015). Popular chemical reactions that result in substitution of the surface hydroxyl groups include: sulphonation, oxidation, carboxylation, acetylation, silylation, esterification, etherification cationisation, amidation, carbidation and phosphorylation (Dufresne, 2013; Raghav et al., 2021). Cellulose acetate and carboxymethyl cellulose are two of the most well-known cellulose derivatives used in numerous biomedical applications, formed through esterification and etherification reactions, respectively (Khine & Stenzel, 2020).

Surface modification can also take place post-synthesis, for example through physical adsorption of a surfactant or polyelectrolyte onto the NC surface. In this study, CTAB was adsorbed onto the NC surface by ionic interaction between the polymer and oppositely charged surfactant. Post-synthesis modification can also be achieved through chemical conjugation with a molecule of interest (Moon et al., 2011; Dufresne, 2013).

For example, the carboxyl groups imparted on TEMPO-oxidised cellulose allow for amidation reactions to functionalise NPs with amino group-containing molecules, such as dyes, proteins, antibodies. The formation of stable amide bonds is achieved through multistep activation or highly reactive reagents, such as isocyanate (Gericke et al., 2020). Commonly conjugated molecules include tumoral markers, DNA/RNA, carbohydrates, and fluorophores (Kamaly et al., 2016). Nanomaterials functionalised with fluorophores are used for fluorescent labelling in bioimaging and pH-sensing (Moon et al., 2016).

Hybrid inorganic-polymeric nanomaterials have beneficial use in biosensing, photovoltaics and anti-microbial applications (Moon et al., 2016). Common approaches used for the synthesis of these materials include non-covalent association by physical adsorption of the polymer onto the inorganic NP, or by covalent interaction between the polymer and inorganic NP (Macchione et al. 2018). This is achieved by popular conjugation attachment methods known as “grafting-to”, “grafting-from” and “grafting-through” approaches (Dufresne, 2013), represented graphically for in Figure 2.4. These synthetic techniques are more laborious than simple physical techniques, but allow for better control of the chemical modification (Macchione et al. 2018).

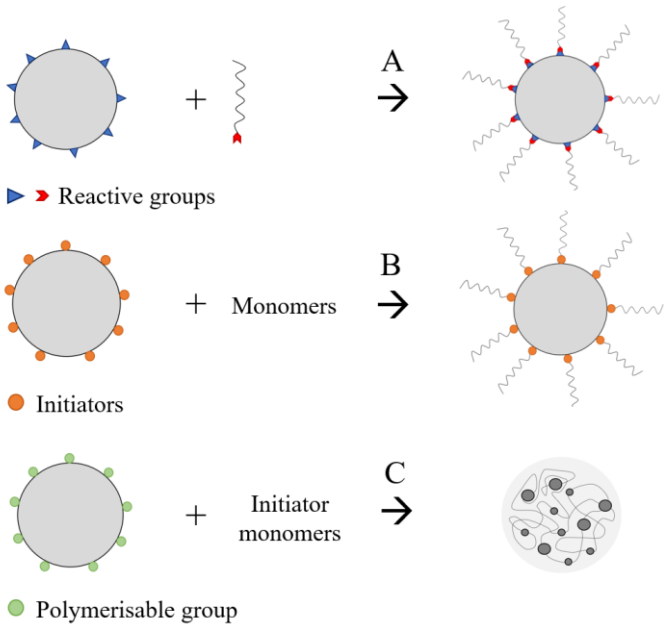

Figure 2.4: Grafting copolymerisation techniques, redrawn from Macchione et al. (2018): (a) grafting-to, (b) grafting-from and (c) grafting-through

"Grafting-to" techniques involve the connection of preformed polymeric chains, by reacting the polymer end groups with functional groups on the NP surface using different coupling agents (Wohlhauser et al., 2018). Grafting-from techniques use various ring opening and radical polymerisation reactions to grow polymer chains *in situ* from initiators on the surface (Roy et al., 2009). Furthermore, grafting-through techniques utilise a low molecular weight co-monomer as an initiator to co-polymerise a macromonomer.

Click chemistry is another popular bioconjugation and surface modification technique, referring to a group of reactions that are simple, fast, versatile and high-yield (Hein, Liu & Wang, 2008). These reactions are typically performed in water, under mild conditions, and allow for easy purification and solvent removal (Hein et al., 2008). Common click chemistry reactions include the Diels-Alder and Thiol-ene reactions, as well as Copper(I)-catalysed azide-alkyne cycloaddition reactions, and Thiol-Michael nucleophilic reactions (Khine & Stenzel, 2020).

Zheng, Li & Huang (2004) identified four requirements for NP modification:

1. Solubility in aqueous solutions
2. Stability without aggregation or agglomeration
3. Minimal interaction with unspecified biomolecules
4. Provide function with the target biomolecules

A common approach to the first requirement is to raise the particle hydrophilicity through grafting with polyethylene glycol (PEG) or polysorbate polymers (Zalipsky & Milton Harris, 1997). PEG-conjugates may exhibit unique physiochemical and biological properties, such as excellent aqueous solubility, reduced clearance, and improved cell membrane permeability (Caracciolo, Farokhzad & Mahmoudi, 2017). However, careful reagent selection and execution of the PEGylation reaction is necessary to avoid undesirable side reactions and PEG derivatives (Zalipsky & Milton Harris, 1997).

The second requirement can be achieved using a number of different surfactants and stabilisers (Zheng et al., 2004), such as CTAB and polyvinyl alcohol (PVA). The adsorption of surfactants allows for the control of a variety of interfacial properties, such as flotation, flocculation and dispersion (Alila et al., 2005). However, many synthetic surfactants have been reported to induce cell membrane lysis (Lunardi et al., 2021), while natural surfactants exhibit lower adsorption capabilities (Bundjaja et al., 2020).

The third and fourth requirements refer to the functionalisation of the drug carrier system for targeted and controlled delivery (Zheng et al., 2004). Passive targeted delivery makes use of the physiochemical properties of the carrier system and its natural distribution pattern to result in accumulation of the drug at the intended site (for example, through direct administration to the region), whereas active targeted delivery relies on surface modification with receptor-recognizing ligands (or antigen-recognizing antibodies) in order to interact with a specific site in the body (Moon et al., 2011; Akhter et al., 2013).

For example, tumors exhibit decreased lymphatic drainage which results in increased retention of extravasated molecules, known as the enhanced permeation and retention (EPR) effect (Gao, Zhang & Sun, 2012). In this way, passive targeted delivery to cancerous tumors can be achieved through natural accumulation. Active targeted delivery can be achieved by modifying the nanocarrier with folic acid ligands which bind to folate receptors present on cancer cells or blood vessels (Akhter et al., 2013). Moreover, physical targeted delivery can be achieved using stimuli-responsive carriers, such as pH-sensitive carriers that degrade upon contact with acidic tumors (Moon et al., 2011; Gao et al., 2012).

2.2.3 Characterisation techniques

Polymeric NPs differ in their physical properties, such as composition and concentration, as well as their morphological properties, such as size, structure, surface chemistry, crystallinity and dispersion state, and can be characterised by various analytical

methods, including electron microscopy, dynamic light scattering (DLS), near-infrared spectroscopy, electrophoresis and chromatography (Carbone et al., 2018; Silva et al., 2019). According to Gericke et al. the three key parameters that should be reported from characterisation of a NP suspension are as follows (Gericke et al., 2020):

- Mean particle size measured as particle diameter (Z)
- Particle size distribution measured as polydispersity index (PdI)
- Suspension stability measured as zeta potential (ζ)

The intensity-weighted mean hydrodynamic particle diameter and PdI of NPs in an aqueous suspension is typically measured by dynamic light scattering (DLS) techniques, whereas important information on the size and shape of dried NPs is typically obtained through scanning and/or transmission electron microscopy (SEM and TEM) (Gericke et al., 2020; Zielinska et al., 2020). Monodisperse systems with narrower size distributions are classified by a PdI $\leq$ 0.1, while systems that are considered moderately and highly polydisperse with wider size distributions have PdIs of 0.1 – 0.4 and > 0.4, respectively (ISO, 2017). Generally, for potential DDSs a PdI < 0.7 is considered acceptable (Danaei et al., 2018), while particles between 20–500 nm are recommended for various *in vivo* applications (Moghimi et al., 1993).

Atomic force microscopy (AFM) has some advantages over conventional electron microscopy, in that it provides information about the 3D topography of the particle – allowing for measurement of additional parameters such as volume, height, aspect ratio, stiffness and Young's modulus (Aschenbrenner et al., 2013), crucial parameters when considering the structural and mechanical properties of the nanomaterial.

The zeta potential ζ (also termed the electrostatic surface potential) is an important property of a nanoparticulate system, in magnitude representing the stability of the system against aggregation, and influenced by pH, ionic strength, particle size and concentration (Gericke et al., 2020). Where the value is positive or negative reflects the particle surface charge, influenced by dissociation of attached functional groups or adsorption of ionic species present in the dispersion medium (Zielinska et al., 2020).

Zeta potential is determined by measuring the velocity of the particles in an external electric field, based on the Doppler effect and electrophoretic light scattering (ELS) techniques (Bhattacharjee, 2016). Generally, the further a system tends away from the isoelectric point (ζ = 0 mV), the stronger the inter-particle repulsive forces and the more

stable it is considered against aggregation and sedimentation, where $|\zeta| > 30$ mV is recommended for potential DDSs (Bhattacharjee, 2016). In this study, where the CNC and CNF DDSs displayed overall negative charges, the objective was therefore to minimise the value of zeta potential (maximising the absolute value).

The modification of NC can further be described by the degree of substitution (DS), which indicates the average number of hydroxyl groups of the anhydroglucose repeat units that have been substituted (Roy et al., 2009). For example, a DS = 3 represents substitution of all three hydroxyl groups. Grafting density can be confirmed with Fourier-transform infrared (FT-IR) spectroscopy, or solid-state 13C nuclear magnetic resonance (NMR) spectroscopy for more quantitative information. The crystallinity index (CrI) of the material may provide insight into the effect of surface modification on the crystalline and amorphous regions of the cellulose chains, and is typically measured via X-ray powder diffraction (XRD), with peaks at 2Θ values of approximately 15°, 17.2° and 22.2° (Khine & Stenzel, 2020). However, these characterisation methods are outside the scope of this study.

The small size of NPs presents a unique challenge in determining and separating the free fraction of unbound drug from the amount of drug associated with the NP (de Jong & Borm, 2008). A widely used technique is ultracentrifugation (Wallace et al., 2013; Bohnert & Gan, 2013), in which the free unbound drug is removed in the supernatant after centrifugation, and quantified using spectroscopic methods, such as UV-visible spectroscopy. The amount of associated drug and binding efficiency – important parameters involved in the optimisation of the DDS for drug delivery – can be calculated from knowledge of the total and free unbound drug concentrations (Zielinska et al., 2020).

2.3 Drug delivery in humans

Pharmacological treatments can be administered via a number of different routes, including but not limited to ingestion, inhalation, transdermal absorption or intravenous injection (Kupnik et al., 2020), with more than 70% of medicines administered orally (Williams, Raimi-Abraham & Luo, 2018). The administered DDS is then absorbed into the bloodstream, distributed to the intended site of action via systemic circulation, metabolised by the liver or kidneys, and finally excreted from the body through urine, faeces, sweat or exhalation (Adepu & Ramakrishna, 2021).

2.3.1 Pharmacokinetics of drug delivery systems

Uptake of the DDS is classified as either first-order (uptake by discrete organs or tissues), second-order (uptake by a specific cell type within organs or tissues), or third-order (uptake by a specific intracellular organelle within cells) (Siepmann & Siepmann, 2009). Low molecular weight drugs can typically enter cells through simple diffusion, whereas higher molecular weight DDSs are taken up by endocytosis, which can be classified according to the following two processes (Siepmann & Siepmann, 2009):

- Phagocytosis: The capture of particulate matter by phagocytic cells (e.g. macrophages) of the reticuloendothelial system (RES)
- Pinocytosis: the engulfment of fluids by all cells.

Phagocytosis is aided by opsonisation, referring to the binding of opsonins (serum proteins recognised by receptors on macrophages, e.g. immunoglobulin G (IgG)) to the target molecule, whereas phagocytosis is hindered by dysopsonins (serum proteins that induce hydrophilicity, e.g. immunoglobulin A (IgA)) (Absolom, 1986).

As discussed, one major goal of targeted drug delivery is to reduce detection by phagocytic cells, in order to prolong circulation and increase the probability of uptake by cells other than those of the RES (Macchione et al., 2018; Gericke et al., 2020; Owida et al., 2022). Particle size has considerable influence over opsonisation and phagocytosis; it has been reported that non-spherical particles < 200 nm experience reduced clearance and prolonged circulation compared to larger, spherical particles (Moghimi et al., 1993; Simone et al., 2008; Pachuau, 2017; Khine & Stenzel, 2020).

Drug elimination is performed mainly by the liver and kidneys; however, metabolism and excretion take place in a variety of other organs throughout the body. Hydrophilic drugs can undergo direct excretion via the kidneys, whereas lipophilic drugs are first metabolised to active or inactive water-soluble products by the liver (Almazroo, Miah & Venkataramanan, 2017). Hepatic metabolism, performed by the cells of the liver (hepatocytes and phagocytic Kupffer cells), is classified as either Phase I or Phase II. Phase I involves oxidation, hydrolysis or reduction reactions catalysed by cytochrome P450 enzymes, while Phase II involves a conjugation reaction (Almazroo et al., 2017).

Both phases serve to increase the polarity of the target molecule, and in turn increase its hydrophilicity and aid excretion via the kidneys. The bioavailability of drugs administered through non-intravenous routes is limited as a result of the first-pass effect,

being the fraction of the drug that is lost after entering the liver via portal circulation and undergoing biotransformation before entering systemic circulation (Almazroo et al., 2017).

The therapeutic success of any given pharmacological treatment depends on the bioavailability of the drug at the intended site of action, i.e. the drug is present at a concentration higher than the minimum effective concentration (MEC) to avoid underdosing, but lower than the minimum toxic concentration (MTC) to avoid potentially harmful side effects (Williams et al., 2018). The advantage of controlled over conventional DDSs is shown in Figure 2.5, which depicts the sustained release concentration-time profile maintained within the therapeutic window, as compared to the immediate release profile.

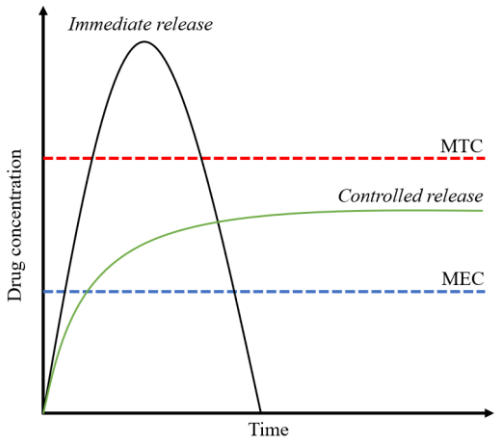

Figure 2.5: Drug concentration vs time profiles of immediate and controlled drug release, indicating the therapeutic window between minimum effective concentration (MEC) and minimum toxic concentration (MTC), redrawn from Williams et al. (2018)

In conventional drug delivery, bioavailability is typically low due to poor water solubility (leading to poor absorption into the bloodstream), poor permeability across biological membranes (e.g. gastro-intestinal tract, mucosa or blood-brain barrier) and/or too rapid metabolism and subsequent clearance from the body (Siepmann & Siepmann, 2009). The intrinsic pharmacokinetic properties of the free drug remain unchanged in the case of a carrier system, but altered distribution and release as a result of the carrier influences the concentration-time profile (Boddy & Aarons, 1989).

2.3.2 Formation of the protein corona

Potential drugs, drug carrier systems or any substance made to interact with the human body needs to be studied and confirmed safe for use through a sequence of tests; pre-clinical trials performed *in vitro* and *in vivo*, followed by human clinical trials. Despite developments in nanomaterials, their clinical application remains somewhat limited, due to

insufficient understanding of their interaction with the physiological environment (i.e. blood and interstitial fluids) (Caracciolo et al., 2017). Once placed in a living system NPs are exposed to high protein concentrations, resulting in the formation of a protein corona (PC) coating that creates a 'biological identity' and mediates the interactions between the particle and its environment (Soppimath et al., 2001; Lundqvist et al., 2008).

The formation of a PC affects circulation, distribution and uptake, and therefore therapeutic effectiveness. The PC formation and composition depends on the physiochemical properties (size, shape, functionality) of the NP (Lundqvist et al., 2017) and the protein source (blood, serum, plasma) (Sieber et al., 2019). In the case of nanomedicines administered intravenously, the PC consists of blood serum components, which vary amongst humans and different animal models, posing a challenge for the translation of both pre-clinical *in vitro* and *in vivo* results to prediction in human clinical trials (Mahon et al., 2012). Müller et al. (2018) studied this theory by comparing the plasma of typical *in vivo* models (rabbit, sheep and mouse) to human plasma, as well as varying NP functionalization, concluding that these factors had significant effects on the aggregation of the NPs, and subsequently biodistribution and uptake.

Accurate prediction of the PC is difficult, and typically comprehensive imaging carried out by mass spectrometry, followed by complex sample processing and analysis, is required for full characterisation of the corona formation (Duan et al., 2020). In the case of NC, it has been reported that the adsorption of proteins may decrease the negative zeta potential of the suspension, as well as contribute to agglomeration and sedimentation in the culture medium (Pinto et al., 2022). Moreover, NPs rich in hydrocarbon surface groups lead to an increase in the production of pro-inflammatory cytokines and the presence of albumin in the formed PC, while NPs rich in carboxylic acid surface groups also increase the production of cytokines, but in response to a higher level of complement proteins and lower amounts of lipoproteins found in their PCs (González-García et al., 2022).

PC formation leads to recognition by phagocytic cells, followed by macrophage activation and clearance by the RES (Sieber et al., 2019). A popular technique to avoid recognition and clearance by phagocytic cells includes surface modification with PEG (Adepu & Ramakrishna, 2021). PEG provides steric stabilisation and polymer flexibility, reducing interaction with serum and plasma proteins (Caracciolo et al., 2017).

2.3.3 Nanotoxicology

A major concern associated with the application of nanomaterials in drug delivery is their toxic effect, especially with chronic administration (Zielinska et al., 2020). Although most modern-day NPs are produced using nontoxic ingredients, accumulation in the liver (the primary organ responsible for reticuloendothelial capture of NPs), spleen and bone marrow increases toxicities to these organs (Akhter et al., 2013). Biodegradable polymeric DDSs are preferred, as their degradations helps remove the carrier system from the body and prevent the accumulation of toxic remnants (Adepu & Ramakrishna, 2021).

Inorganic, metallic nanocarriers are among the most extensively researched systems for their toxicity (Canesi et al., 2008). Despite the frequent use of PEGylation in the preparation of these NPs, its mechanism for biological interaction is not entirely understood, and it has been shown to sterically prevent access of tissue proteins (Romberg, Hennink & Storm, 2008). Moreover, there is significant concern over NPs that are capable of crossing the blood-brain barrier (BBB); a clinical trial of testing a polymeric paclitaxel DDS was terminated due to neurotoxicity (Meerum Terwogt et al., 2001).

The successful formulation of a nanomedicine depends on the biocompatibility of the chosen material, and its ability to encapsulate and release the desired drug (Pachuau, 2017). Particle size, charge, surface chemistry and hydrophobicity influence its interaction with the cell membrane (Kumari, Yadhav & Yadhav, 2010), therefore it is important to test cytotoxicity of formulations against a range of human cell types. CNC has been reported to show insignificant cytotoxic effects when tested against nine different cell lines (at a concentration range and exposure time of 0–50µg/mL and 48h, respectively) (Dong et al., 2010; Roman et al., 2010). Interestingly, when comparing the cytotoxicity of fibrillar and crystalline NC materials on pulmonary epithelial cells, it was found that CNF resulted in increased oxidative stress in particular, whereas CNC caused an elevated inflammatory response (Menas et al., 2017). Moreover, synthetic surfactants have been reported to induce cell membrane lysis (Lunardi et al., 2021).

Lie et al. (2017) reviewed numerous toxicity studies on both CNC and CNF and concluded that the NC materials exhibit high biocompatibility, in addition to low cytotoxicity, genotoxicity, immunotoxicity, and ecotoxicity; displaying minimal interference with cellular functions. Any possible toxic effects are dependent on the concentration, surface chemistry (as a result of the preparation process), and physical form

(e.g. suspension, hydrogel, film) of the NC material (Löbmann & Svagan, 2017). Therefore, *in vitro* studies are necessary in order to study the influence of the above-mentioned factors over any potential inflammatory response, oxidative stress or toxicity (Endes et al., 2016). However, further *in vivo* studies should be performed for accurate prediction of toxic effects and undesirable biological activity exhibited by the DDS.

2.4 Drug release from the delivery system

The process of a drug leaving its carrier system to undergo absorption, distribution, metabolism and excretion (ADME) in the body, thereby becoming available for pharmacological action, is termed drug release (Shaikh, Kshirsagar & Patil, 2015). The release mechanism of a DDS is determined by the rate-limiting step (Adepu & Ramakrishna, 2021), and is controlled either by dissolution, diffusion, water penetration (swelling and osmotic pressure), or chemically controlled (Gupta et al., 2010).

2.4.1 Mechanisms of drug release

Diffusion is the typical mechanism by which a drug leaves a polymeric carrier system, and can be aided by swelling of the matrix, or in the case of biodegradable polymers – enzymatic degradation and surface or bulk erosion through hydrolysis (Shaikh et al., 2015). In summary, the release profile of a drug from polymeric NPs depends on one or more of the following factors (Soppimath et al., 2001; Kamaly et al., 2016; Bohrey, Chourasiya & Pandey, 2016):

- Desorption of the drug from the particle surface and/or polymeric matrix erosion
- Diffusion of the drug through the nanosphere matrix or nanocapsule polymer wall
- Combined diffusion and erosion processes

Drug release from polymeric NPs has been successfully described using various experimental methodologies, such as diffusion from dialysis bags (as used in this study), as well as drug-carrier separation by ultracentrifugation, low-pressure filtration, and ultrafiltration-centrifugation (Soppimath et al., 2001; Shen & Burgess, 2013).

An important assumption in simplifying the derivation of these mathematical release models is that a pseudo steady-state is maintained during drug release, by the presence of excess solute (an initial drug concentration higher than the saturation solubility of the drug) (Bruschi, 2015). Moreover, constant diffusion and sink conditions are assumed, with no interaction occurring between the drug and matrix (Bruschi, 2015).

2.4.2 Release kinetics models

Mathematical modelling of drug release rates can achieved through both linear and non-linear regression of experimental cumulative release (%) versus time profiles. Common fitted models, and those chosen to be investigated in this study, include zero- and first-order models, as well as the Korsmeyer-Peppas and Higuchi model (Dash et al., 2010). Drug release kinetics from nanocapsules are generally zero-order (constant release), due to the dissolved drug releasing from the oily nucleus upon diffusion through the polymeric wall, whereas release kinetics from nanospheres are generally first-order (exponential release), due to drug release by diffusion from the matrix to the outside environment as well as release by erosion of the polymeric matrix (Zielinska et al., 2020).

Zero-order release rates are independent of concentration (Dash et al., 2010), as seen by the rate constant term K in Equation 2.1, where Q_t is the amount of drug released at time t and Q_0 is the initial amount released (equal to zero). First-order release rates however are dependent on the loaded drug concentration of the NP (Dash et al., 2010), as described mathematically in Equation 2.2. Therefore, plotted zero-order release data displays a straight line, whereas first-order data would display a curved line.

$$Q_t = Q_0 + Kt \quad [2.1]$$

$$Q_t = Q_0 e^{-Kt} \quad [2.2]$$

The Higuchi model (Equation 2.3) describes drug release from a matrix system based on Fick's simple law of diffusion (Higuchi, 1963), which is dependent on the square root of time and where Q_t / Q_0 represents the fraction of drug released at time t. The Korsmeyer-Peppas semi-empirical power law (Equation 2.4) derives a simple relationship to describe the release of a drug from a polymeric system (Korsmeyer et al., 1983).

$$Q_t/Q_0 = Kt^{0.5} \quad [2.3]$$

$$Q_t/Q_0 = Kt^n \quad [2.4]$$

The values for the release exponent n describe the mechanism of release according to Table 2.2 (Dash et al., 2010). This model is the basis for the theory that a drug with both an erosion- and diffusion-controlled release rate is governed by anomalous (non-Fickian) diffusion, displaying a first-order release (Camelo et al., 2016), as expected by the formulated DDSs in this study. Swelling-controlled systems exhibit super case II (relaxational) transport, describing polymer hydration and swelling (and disentanglement and dissolution), related to matrix erosion for non-swellable systems (Camelo et al., 2016).

Table 2.2: Mechanism of drug release as determined by the value of the release exponent (n) regressed for the Korsmeyer-Peppas model

Release exponent (n)	Drug transport mechanism	Rate as *f* (time)
$0.45 \leq n$	Case I Fickian diffusion	$t^{-0.5}$
$0.45 < n < 0.89$	Anomalous (non-Fickian) diffusion	First-order
$n = 0.89$	Case II transport	Zero-order
$n > 0.89$	Super case II transport	t^{n-1}

2.5 Zebrafish as *in vivo* models

In vitro models often fail to "mimic the complex biological situation nanomedicines will encounter *in vivo*" (McGrath & Li, 2008; Haque & Ward, 2018). With specific regard to studying drug toxicity effects, *in vitro* assays are often not predictive of certain ADME results, otherwise obtainable from *in vivo* assays (Peterson & MacRae, 2012). Many *in vivo* models have been developed for invertebrate organisms, such as yeast (*Saccharomyces cerevisiae*), roundworms (*Caenorhabditis elegans*) and fruit flies (*Drosophila*), due to their easy genetic modification and high-throughput capacity (van Wijk et al., 2016). However, vertebrate species are often preferred in pharmacological studies because of their increased genetic homology to mammals (Lee et al., 2017).

2.5.1 Overview and features of zebrafish

Mammalian models, such as mice, are most commonly used in modelling human disease, owing to the homology between their genomes and cell biology, and that of a human (van Wijk et al., 2016). However, mice together with their popular mammalian counterparts (rats, rabbits, canines and primates) have significant drawbacks, in that they are often expensive, time-consuming and raise ethical concerns (Lieschke & Currie, 2007). Zebrafish (*Danio rerio*), in their embryonic, larval and adult form, have been posed as a promising alternative for the *in vivo* testing of potential therapeutic delivery systems.

Their main advantages over other vertebrate models include their high fertility, rapid development, optical transparency and relatively straightforward genetic modification (Grunwald & Eisen, 2002; Haque & Ward, 2018). Interest in zebrafish as new model vertebrates began in the early 1970s, with the simplicity of their experimental methods attracting the attention of researchers (Howe et al., 2013). Zebrafish are 70%

genetically homologous with humans (McGrath & Li, 2008), and have anatomically, physiologically, and molecularly similar organ structures (Kar & Subbiah, 2013).

The low husbandry costs associated with zebrafish are owed largely to their small and robust structure, the size of approximately 3 cm in the case of adult zebrafish and only 2–3 mm in the case of embryonic and larval zebrafish, which can survive for days in individual wells of standard 96-well plates, in as little as 200 µL of fluid, living off the nutrients stored in their yolk sac (Lee et al., 2017). Additionally, the high fecundity of zebrafish provides statistical reliability through multiple experimental groups and large sample sizes (Nasevicius & Ekker, 2000). The characteristics of zebrafish models are compared to other popular animal models in Table 2.3, reproduced from Lee et al. (2017).

Table 2.3: Comparison of the main characteristics of popular animal models (zebrafish, primate, mouse and chick) used for *in vivo* testing, from Lee et al. (2017)

Characteristic	Zebrafish	Primate	Mouse	Chick
Handling	Easy	Difficult	Difficult	Moderate
Genetic homology	70%	96-98%	75%	62%
Development	Fast	Slow	Slow	Fast
Transparency	Yes	No	No	No
Embryos	100-600	1-2	~10	1-2
Transgenic models	Many	Few	Many	Few
Maintenance cost	Cheap	Very expensive	Expensive	Cheap

Zebrafish have similar cardiovascular, nervous and digestive systems to mammals, with embryonic zebrafish beginning their major organ development around 24 hours post fertilization (hpf) and becoming fully morphologically developed by 96 hpf (McGrath & Li, 2008). The optical transparency of zebrafish is an advantageous characteristic that allows for the observation of important internal events, such as tumor and organ development, vessel growth and NP distribution (Lee at al., 2017). By 120 hpf, the zebrafish has discrete organs, including a brain, heart, liver, intestine, eyes, ears and swim bladder (White et al., 2008), and matures into an adult by three months.

Embryonic transparency is only retained until approximately 60 hpf, but treatment with 1-phenyl 2-thiourea (PTU) can inhibit the pigmentation process, or transgenic models of adult transparency, such as Casper (Sieber et al., 2019), can be employed (Peterson & MacRae, 2012). Transgenic organisms have had their genome altered through genetic engineering techniques. A specific gene (the transgene) is introduced, removed or modified and results in the organism expressing a new attribute or characteristic of this gene. A wide range of transgenic zebrafish models have been developed for *in vivo* modelling purposes (Santoriello & Zon, 2012). A simple diagram of the internal anatomy of both a larval and adult zebrafish is illustrated in Figure 2.6 below, redrawn from Santoriello & Zon (2012).

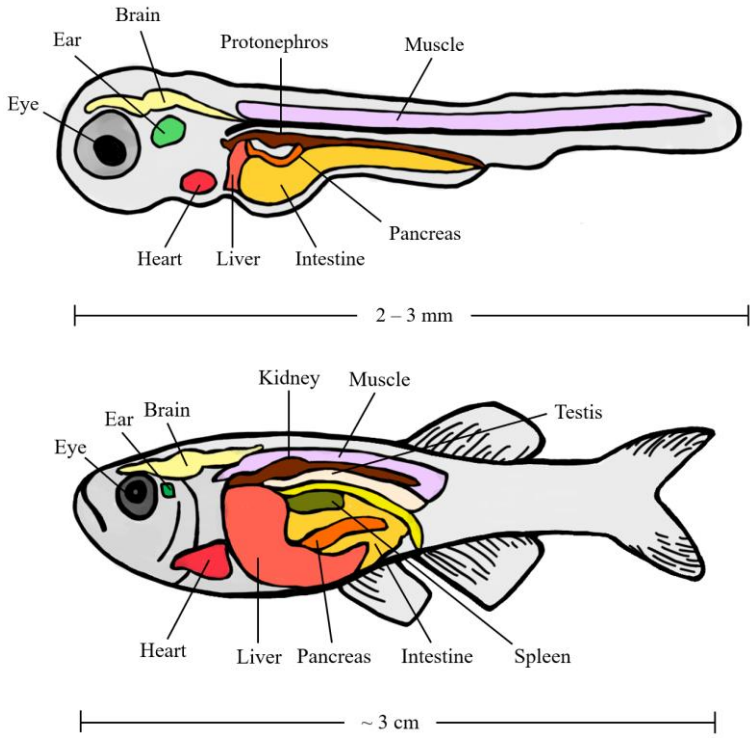

Figure 2.6: The internal anatomy of a zebrafish in its larval (top) and adult (bottom) form, redrawn from Santoriello & Zon (2012)

2.5.2 Toxicity of nanoparticles in zebrafish

The zebrafish is particularly suitable for assessing toxicity because it is a vertebrate species, its genome has been sequenced (Caballero & Candiracci, 2018) and it has a high cost-effect benefit (Harper et al., 2016). Caballero & Candiracci reviewed multiple studies performed on the cardiotoxicity of anti-cancer and anti-psychotic drugs (e.g. doxorubicin, aripiprazole, respectively), in zebrafish models, as well as various studies on genotoxicity and hepatotoxicity (Caballero & Candiracci, 2018). Studies performed on the neuro- and

developmental toxicity of zebrafish in response to administered DDSs have been reviewed by McGrath & Li, who reported toxicity profiles of the mammalian and zebrafish model organism to be remarkably similar (McGrath & Li, 2008).

The biocompatibility of NC was investigated by Harper et al., they described that method of preparation and chemical modification influences the toxicity of the cellulose material to embryonic zebrafish (Harper et al., 2016). Specifically, the surface chemistry of the NP (neutral, anionic or cationic) had minimal effect on toxicity, whereas higher aspect ratio CNF produced via mechanical methods were found to be more toxic than CNF or CNC produced via chemical methods. However, both the CNC and CNF showed overall low toxicity to developing zebrafish (Harper et al., 2016; Lee et al., 2017.)

2.5.3 Testing nanoparticles in zebrafish

The performance of a DDS using *in vivo* testing can be assessed by a number of different outcomes, obtained through both qualitative phenotypic observations and quantitative methods of characterisation. According to Sieber et al., DDSs should demonstrate "low cytotoxicity, stability in biological environments, controlled blood circulation half-life, cell/tissue specificity and efficacy/functionality under *in vivo* conditions" which can be achieved through optimisation of physiochemical characteristics of the particle, such as size, shape and surface chemistry (Sieber et al., 2019).

Biotoxicity can be assessed through a number of different phenotypic observations, such as organ development, hatching and survival rates, and heart functionality, whereas efficacy and biodistribution trends are typically observed through fluorescently labelled nanomaterials or TEM analysis, with quantification of accumulation via inductively coupled plasma mass spectrometry (ICP-MS) (Lee at al., 2017). These tests should be coupled with the evaluation of a functional response to the treatment, and many automated procedures have been developed to evaluate behavioral toxicity parameters, such as locomotory patterns (e.g. swimming speed and depth) (Kane, Salierno & Brewer, 2005). These results can be affected by multiple parameters, including (McGrath & Li, 2008):

- The development stage (embryonic, larval, or adult) and specific transgenic line
- The presence of a chorion during growth
- Agglomeration or sedimentation of the NPs
- Maintenance (temperature, conductivity, pH, feeding, housing density)
- Administration of the nanomedicine (e.g. incubation or intravenous injection)

Zebrafish are housed at about 28°C under standard conditions (Sieber et al., 2019), and in order to obtain reliable efficacy, biodistribution and biotoxicity results, the above-mentioned maintenance parameters should be controlled and kept as constant as possible. The experimental administration of the drugs or compounds to be tested in the zebrafish can be approached in multiple ways, for example (Rosen, Sweeney & Mably, 2009):

- Dilution of the drugs in the surrounding solution for larvae to absorb through their skin and gills (particularly for small, hydrophilic molecules).
- Oral delivery of the drugs from 72 hpf onwards once the zebrafish can swallow.
- Injection of the drugs into the yolk sac, sinus venosus or circulation (particularly for large, hydrophobic molecules and proteins).

Precise quantities (up to 3 nL) of sample can be injected using a microinjector system, whereby adjusting the air pressure and volume allows for calibration of sample volumes, via injection into mineral oil followed by scaled drop size measurements (Sieber et al., 2019). Injection into the yolk sac of the zebrafish should be avoided, as this material does not enter circulation and an unknown volume is lost (McGrath & Li, 2008).

Direct injection is controllable, whereas the uptake of the test substance by the zebrafish cannot be guaranteed when administering via direct incubation. Due to the lack of an established protocol for *in vivo* modelling with zebrafish, studies use inconsistent conditions and comparison between research becomes difficult. Lee et al. (2017) proposed recommended guidelines for both direct incubation and injection.

Although a larger array of compounds needs to be assessed and studied in order to confidently validate the zebrafish model for accurate *in vivo* testing, their convenience and low cost have allowed them to serve as a reliable and high-throughput intermediate step between *in vitro* evaluation and conventional rodent testing, in the early stages of pre-clinical trials (Caballero & Candiracci, 2018).

2.6 Design of experiments for process improvement

Process optimisation aims to determine the factor conditions that will result in the best possible response. Studying the influence of multiple factors on a response using the one-factor-at-a-time (OFAT) approach is both time-consuming and does not allow for investigation into interaction effects (Montgomery, 2012). DOE techniques are multivariate statistical methodologies that allow for parametric optimisation, especially useful when many independent variables are varied simultaneously (Montgomery, 2012).

In industry, DOE techniques are widely applied to simulate complex processes, due to their efficiency and low time, material and cost demands (Yahya et al., 2019).

The dominant variables that have the greatest influence over the process are typically identified by carrying out the OFAT approach, whereafter a factorial design may be employed to study the main and interaction effects of these factors (NIST & SEMATECH, 2012). Each factor is set at a high (+1) and low (–1) level, and experiments are run at every combination of these factors across their levels. For *a* levels of Factor A and *b* levels of Factor B, there are *ab* treatment combinations for each replicate in the design. When more than four factors are to be investigated, a fractional factorial design is recommended, whereby only a subset of the full factorial experimental runs are performed, and certain higher-order interactions are assumed negligible (Montgomery, 2012).

The design geometry of a 2-factor-2-level full factorial design (FFD) is depicted in Figure 2.7a, with the four corners of the square representing the four experimental runs necessary to complete the design. The addition of centre points can indicate any potential curvature in the response, however, the further addition of axial points is necessary to allow for this curvature to be modelled (Myers, Montgomery & Anderson-Cook, 2009).

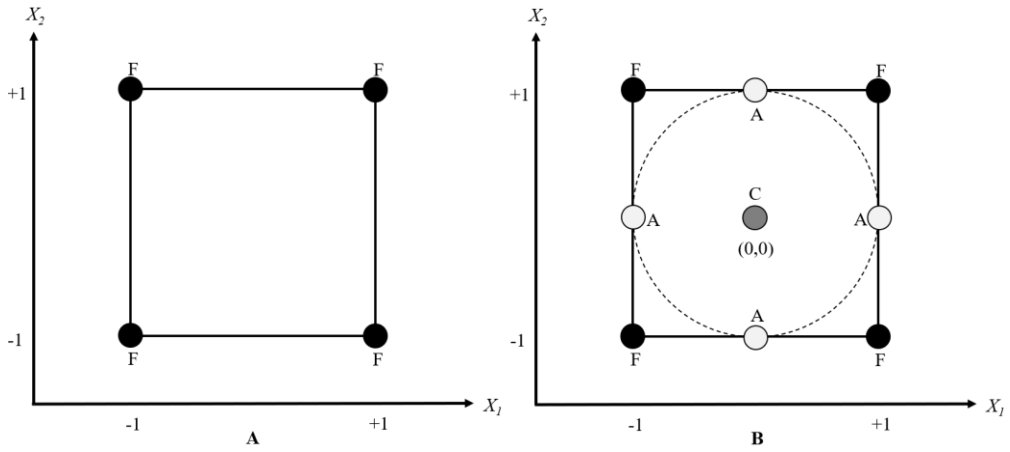

Figure 2.7: Design geometry of a 2-factor (X_1, X_2) (a) full factorial design (FFD) and (b) face-centred central composite design (CCD), with factors at a high (+1), low (–1), or centre (0) level and points either in the factorial (F), axial (A) or central (0) space

RSM is a parametric optimisation method developed by Box and Wilson (1951), that models the relationship between factors and responses by visualisation of the response surface (Box & Draper, 1987). A central composite design (CCD) is one type of response surface design, that allows for this visualisation by fitting second-order response models using least-squares regression (Myers et al., 2009). For a face-centred design, the distance

from the axial points to the centre is set to one, foregoing rotatability (constant prediction variance at all points equidistant from the centre); this design geometry is depicted in Figure 2.7b. However, it is generally accepted that any possible reduction in effects estimation and prediction error for rotatable designs compared to orthogonal face-centred designs is insignificant when considering only two factors (NIST & SEMATECH, 2012).

The blocking design geometry of separate factorial and axial blocks, each with centre point replicates and randomization of experimental runs within each block, allows for determination of the experimental (pure) error and reproducibility of the results. The design matrix of each block is orthogonally coded, allowing for model terms and block effects to be estimated independently, thereby minimizing variation in the regressed coefficients describing the response (Box & Draper, 1987).

The Box-Behnken (1960) design is another commonly used design that allows for regression of response models, but unlike a CCD (otherwise called a Box-Wilson design), the Box-Behnken design geometry does not include an embedded FFD and cannot be used for two factors (NIST & SEMATECH, 2012). Moreover, optimisation by the Taguchi (1987) method serves as an alternative to RSM. Taguchi robust parameter design techniques focus on maximising the signal-to-noise (S/N) ratio of the response, in contrast to RSM that focuses on minimising error between predicted and experimental response data (Myers et al., 2019). Often Taguchi methods are employed for initial screening of influential factors through highly fractionated factorial designs, whereafter RSM is used to optimise the dominant variables (Montgomery, 2012).

Chapter 3: Experimental work

3.1 Experimental approach

NC is a naturally hydrophilic compound, therefore surface modification with the cationic surfactant CTAB has been studied for the effective loading of water-insoluble and non-ionizable drugs, such as hydrophobic anti-cancer drugs (docetaxel, paclitaxel, etoposide) (Jackson et al., 2011), NSAIDs (ibuprofen, etodolac, diclofenac) (Gupta & Raghav, 2020), or plant flavonoids (curcumin) (Raghav et al., 2020; Zainuddin et al., 2017). Additionally, NC has been reported to associate with the plant flavanol quercetin via hydrogen bonding, in the absence of surfactant (Li et al., 2019; Liu et al., 2021). In this study, both CNC and CNF were investigated as potential drug carriers for quercetin (structure in Figure 3.1), utilising CTAB (Figure 3.2) as a surfactant, with methodologies based on the literature cited (Jackson et al., 2011; Zainuddin et al., 2017; Li et al., 2019; Gupta & Raghav, 2020; Raghav et al., 2020; Liu et al., 2021).

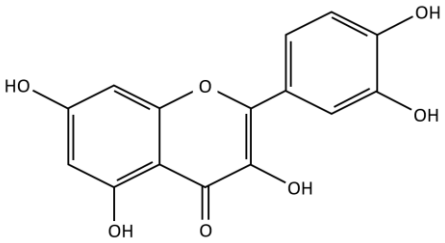

Figure 3.1: Chemical structure of quercetin (3,3′,4′,5,7-pentahydroxyflavone) drawn with PowerPoint (Microsoft Office®, 2022)

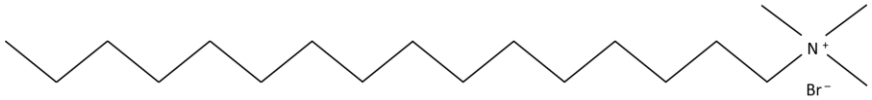

Figure 3.2: Chemical structure of cetyltrimethylammonium bromide, drawn with PowerPoint (Microsoft Office®, 2022)

The hydrophilic-lipophilic balance (HLB) of a surfactant can be represented in the range 0 – 20, where a value < 10 indicates lipophilicity, and > 10 indicates hydrophilicity. The HLB value of CTAB is approximately 10 (Doolaanea et al., 2015). The interaction between negatively charged NC and the positively charged head of CTAB is governed by electrostatic polymer-surfactant interactions (Alila et al., 2005; Abitbol et al., 2014, Tardy et al., 2017), while hydrophobic interaction is responsible for the binding of quercetin to the long alkyl CTAB tails, in order to minimise contact with water (Khine & Stenzel, 2020). The intended mechanism of interaction between the sulphated CNC or carboxylated CNF surface, and the surfactant and drug, is illustrated in Figure 3.3.

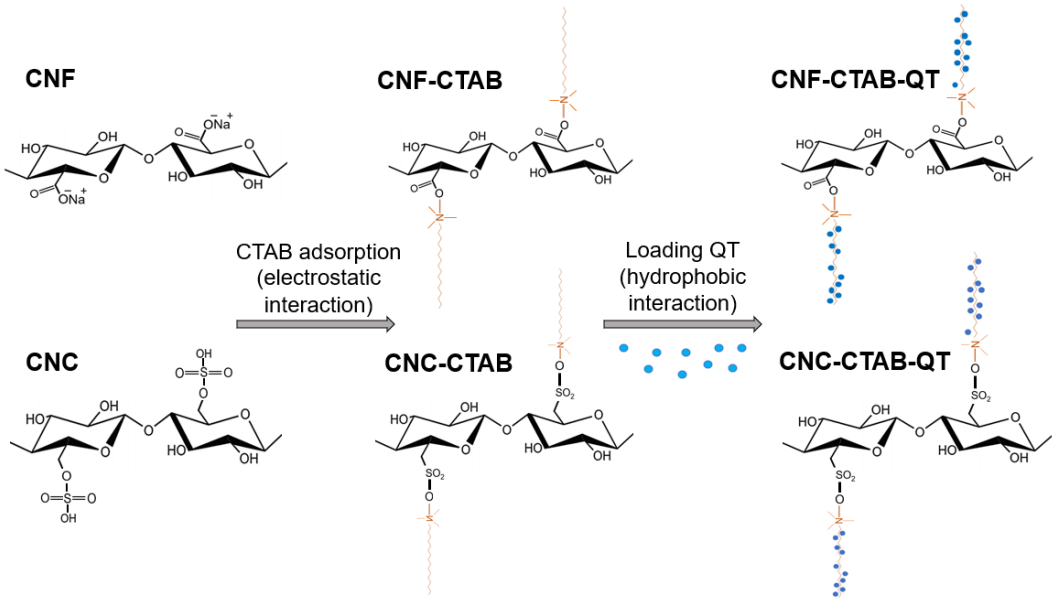

Figure 3.3: Depiction of the intended interaction chemistry between anionic cellulose nanocrystals (CNC) and nanofibrils (CNF), the cationic surfactant (CTAB), and hydrophobic quercetin (QT), drawn with PowerPoint (Microsoft Office®, 2022)

Quercetin has anti-inflammatory, anti-oxidant, and anti-viral properties (Zhang et al., 2008), but poor solubility in water (0.01 mg/mL, 25 ºC) (Gao et al., 2011). However, quercetin shows increased solubility in ethanol, so that for this study the chosen solvent was 75 wt% ethanol, in which quercetin has a solubility of about 5.6 mg/mL (25 ºC) (Razmara, Daneshfar & Sahraei, 2010). The chosen wt% of ethanol was based on previous work by Li et al. (2019), where this concentration was found to result in optimum binding conditions between quercetin and CNF. Figure A.1 in Appendix A compares two quercetin mixtures, one prepared with 75 wt% ethanol and the other with distilled water.

The NPs were characterised in terms of size, charge, and drug binding, as these characteristics are considered crucial in determining the uptake, distribution, rate of release and therapeutic efficacy of the DDS (Gericke et al., 2020; Khine & Stenzel, 2020). RSM was applied through a 2-factor CCD with an embedded FFD and used to regress second-order models describing the effect of CTAB and quercetin concentration on measured responses, further allowing for the visualisation of these relationships through response surface and contour plots, as well as parametric optimisation by desirability analysis. This experimental design is expanded on in Section 3.4. The *in vitro* release kinetics and *in vivo* toxicity were investigated by the dialysis method and zebrafish model, respectively. The flowchart in Figure 3.4 provides the overall study approach.

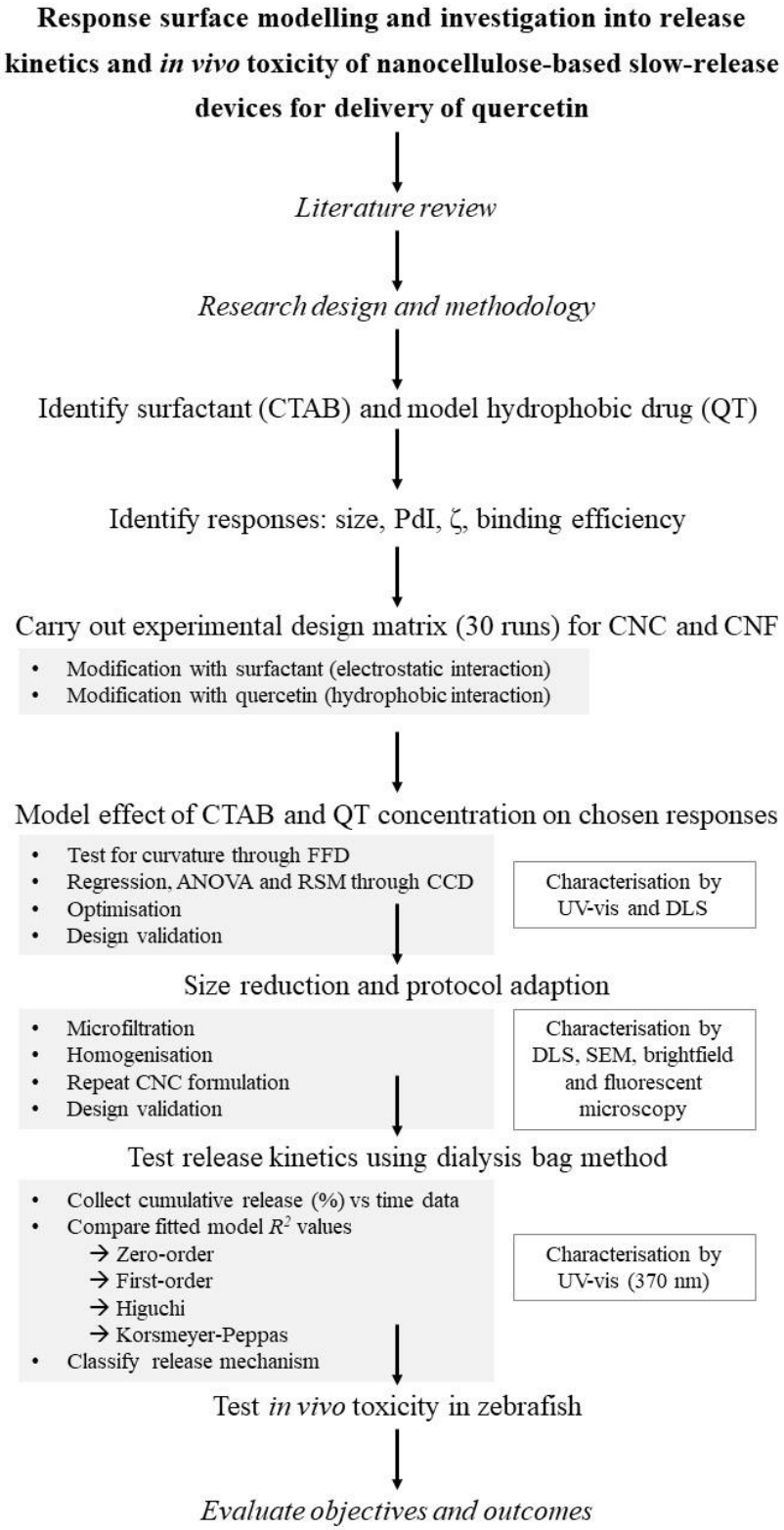

Figure 3.4: Flowchart of the overall study approach for the response surface modelling and investigation into release kinetics and in vivo toxicity of nanocellulose-based slow-release devices for delivery of quercetin

3.2 Materials and equipment

3.2.1 Materials

A commercial 1.9 wt% CNC liquid suspension from Sappi Biotech (South Africa), as well as freeze-dried CNC and CNF from the University of Maine Process Development Center (United States) were obtained. The CNC and CNF provided by the University of Maine had characterisation data according to Table 3.1, whereas the CNC provided by Sappi Biotech first underwent Zetasizer characterisation, displaying a mean hydrodynamic diameter of 5731 nm, a PdI of 0.86 and a zeta potential of –23.5 mV.

Table 3.1: Particle size and characterisation data for the cellulose nanocrystals (CNC) and cellulose nanofibrils (CNF) provided by the University of Maine (United States)

Sample	Diameter (nm)	Length (nm)	PdI	Zeta potential (mV)
CNC	27 ± 6	173 ± 5	0.47 ± 0.01	–45.0 ± 8
CNF	27 ± 8	> 1 µm	1 ± 0.03	–14.5 ± 1

Solid quercetin powder (purity ≥ 95%, HPLC), as well as the reagents cetyltrimethylammonium bromide (≥ 97%) and ethanol (95%), were obtained from Sigma-Aldrich (Merck Life Science, South Africa). Distilled water (reverse-osmosis) was used for all dilutions in sample preparation, as well as redispersion of solids.

3.2.2 Equipment

An A&E S60 UV-Visible Spectrophotometer (China) and a Malvern Zetasizer Nano ZS (United Kingdom) were used for analytical studies and particle characterisation. Moreover, a Lasec TG16.5 (50 mL) (South Africa) and an Ohaus Frontier 5000 Series Multi FC5706 (15 mL) (Germany) centrifuge were used for routine centrifugation purposes. Other equipment used included a Labotech ScienTech 701 ultrasonic cleaner (South Africa), a ProScientific Bio-Gen Pro-250 rotor-stator homogeniser (United States), and a Vacutec V-FD12 freeze dryer (South Africa). Seamless cellulose acetate dialysis tubing (99.99% retention, MWCO 14 kDa, 25 mm flat diameter), as well as 10 µm, 1 µm, and 0.45 µm (25 mm diameter) nylon syringe filters were obtained from Merck Life Science and Axiology Labs (South Africa), respectively.

3.3 Methods

3.3.1 Modification of cellulose nanoparticles with surfactant

CNC and CNF 0.4 wt% stock solutions, as well as CTAB stock solutions (concentrations varied from 2.0, 4.0, and 6.0 mM) were prepared in distilled water. The polymer suspensions (25 mL) were slowly added to the CTAB solutions (25 mL), in 250 mL volumetric flasks, with 200 rpm stirring for 15 minutes. The reaction mixture was then heated at 60°C for three hours to ensure adequate ionic bonding, and left to stir overnight at room temperature. After this, unbound CTAB was subsequently removed by 10 minutes of centrifugation at 10 000 rpm.

3.3.2 Loading modified nanoparticles with quercetin

The respective CTAB-modified NC suspensions (5 mL) were added to 5 mL of quercetin solution (concentrations varied from 1.0, 5.5, and 10.0 mg/mL) and mixed with a swirling test tube mixer at room temperature for 30 minutes. The suspension was centrifuged for 15 minutes at 6 000 rpm, and the supernatant was collected to determine the concentration of unbound quercetin using UV-visible spectroscopy.

3.3.3 Size reduction

Particle size and size distribution reduction were investigated by way of sequential syringe microfiltration, ultrasonication and homogenisation. To break up larger particles and agglomerates, suspensions were sonicated at 25 ºC under high power, high frequency for 30 minutes. Temperature increase was monitored so as not to exceed 37 ºC, the temperature at which quercetin starts to degrade (Wang & Zhao, 2016; Chaaban et al., 2017), and degradation products may begin to form.

Moreover, homogenisation of the stock solutions of polymer (CNC, CNF) and quercetin was carried out using an 18 mm probe, operating at 24 000 rpm for six minutes (Xhanari et al., 2011; Karadag, Ozcelik & Huang, 2014; Furtado et al., 2021). The solutions were kept in an ice water bath, and the probe was operated in two-minute intervals to avoid excessive temperature increase and degradation.

3.3.4 *In vitro* release kinetics tests

Schematically shown in Figure 3.5, the release kinetics of quercetin from the DDSs was determined using the dialysis bag method (Wallace et al., 2012; Yu et al., 2019). 5 mL of the QT-CTAB-modified NC suspension was sealed inside cellulose acetate dialysis tubing (MWCO 14 kDa), pre-soaked in distilled water for 12 h to remove any contaminants

that may be present . The tubing was placed in a beaker containing 250 mL of an ethanol-water (3:7) mixture, with conditions maintained at 37°C and stirred at 120 rpm. A fixed volume (2 mL) of the sink medium was withdrawn every 20 minutes for up to two hours, for further analysis with UV-visible spectroscopy to determine the concentration of released quercetin. With every sample withdrawn the sink was replenished with fresh medium of equal volume in order to maintain sink conditions.

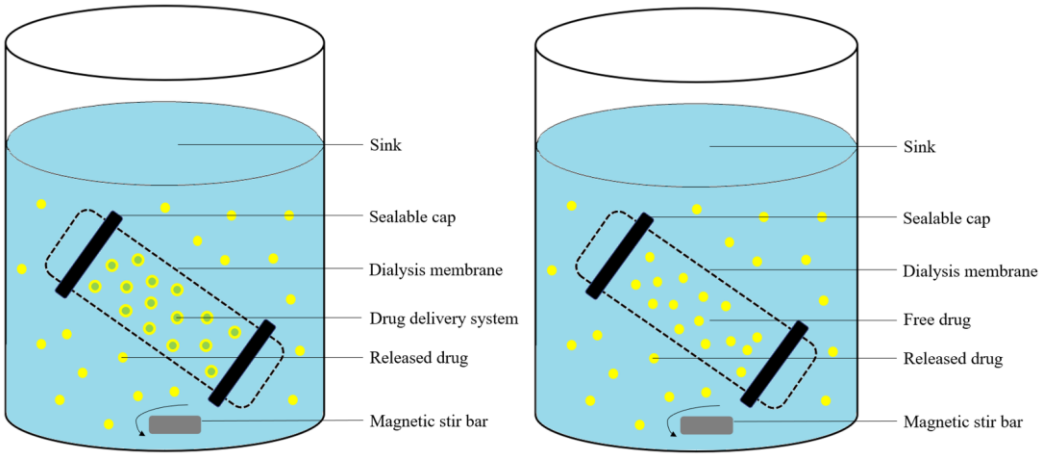

Figure 3.5: Graphical illustration of the dialysis release test set-up for the drug delivery system (DDS) (left) and free drug (right) control run

The change in quercetin concentration of the sink over time was monitored to allow for calculation of cumulative percent quercetin release. Cumulative release profiles were developed for quercetin loaded in a DDS formulation, as well as a control run consisting of free quercetin present in an amount equivalent to that of the DDS. These cumulative release profiles were then fitted to appropriate kinetic models, namely the zero-order, first-order, Higuchi and Korsmeyer-Peppas model (given in Equations 2.1 – 2.4). The kinetic parameters (release rate constants) were calculated, and the respective coefficients of determination (R^2) were compared.

3.3.5 *In vivo* zebrafish tests

General toxicity of the DDS was assessed by the zebrafish research unit in the Division of Clinical Pharmacology, Department of Medicine, Faculty of Health and Medical Sciences, Stellenbosch University. Toxicity test protocols used were designed according to the Organisation for Economic Co-operation and Development (OECD) guidelines, and all protocols were ethically cleared by the Stellenbosch University Animal Research Ethics committee (REF#: ACU-2019-11820).

3.4 Experimental design

The optimum process conditions for the modification of CNC and CNF with the surfactant and drug were determined using RSM tools provided by Minitab® Statistical Software, version 21.1. A 2-factor FFD, expanded to become a face-centred CCD, was applied to study the process. The identified independent variables (factors) are X_1: CTAB concentration (2 – 6 mM), and X_2: quercetin concentration (5 – 10 mg/mL). The identified dependent variables (responses) are mean hydrodynamic particle diameter (Z), polydispersity index (PdI), zeta potential (ζ), and quercetin binding efficiency (BE). Table 3.2 lists the actual and coded high (+1), low (–1) and centre (0) levels of each factor, with the ranges based on various literature findings.

Table 3.2: Factors and their corresponding natural values evaluated at each coded level (low, centre and high) of the experimental design

Factor	Low level (-1)	Centre (0)	High level (+1)
X_1: CTAB concentration (mM)	2	4	6
X_2: QT concentration (mg/mL)	1	5.5	10

Three replications per experimental run resulted in a total of 15 runs per polymer in the FFD (12 factorial and three centre points) and 30 runs per polymer in the CCD (12 factorial, 12 axial and six centre points). The results from the FFD were used for the factorial block runs of the CCD, and in order to minimize systematic error, the run order of the experiments in each block was randomised.

Non-linear regression was performed on the collected data in order to derive an equation describing the response, in which all variable parameters and their interactions were included. Minitab® was used to solve for the regression coefficients of the second-order model (given in Equation 3.1) for each response, where y_i is the i^{th} response, x_i is the i^{th} factor, n is the number of factors and β_0, β_i, β_{ii}, and β_{ij}, are the constant, linear, quadratic and cross product coefficients, respectively. Quadratic cross-products are generally considered negligible (Montgomery, 2012) and were not taken into account.

$$y_i = \beta_0 + \sum_{i=1}^{n} \beta_i x_i + \sum_{i=1}^{n} \beta_{ii} x_i^2 + \sum_{i<j} \beta_{ij} x_i x_j \qquad [3.1]$$

Effects models, as well as statistical and regression models were developed, and goodness-of-fit was studied by comparing the model coefficients of determination, root-

mean-square and cross validation errors, and analysis of variance (ANOVA) results determined using the Fisher's test (F-test). A confidence level of 95% (alpha = 0.05) was chosen so that $p < 0.05$ indicates statistical significance. A significant p-value means there is sufficient evidence to reject the null hypothesis H_0 that the coefficient is zero (no association between the term and response), in favour of the alternate hypothesis H_a, and conclude that the coefficient is statistically different from zero (Devore, 2016).

Moreover, 3D-surface plots of the responses were modelled using MATLAB® software, version R2018b. In addition, analysis of the residuals (the difference between the observed and predicted response) was performed to validate the assumptions of normality made during ANOVA (Montgomery, 2012). All supplementary calculations, such as means, percentage error and standard deviations for replicate measurements were determined using Excel (Microsoft Office®, 2022).

3.5 Analytical methods

3.5.1 Particle size and charge analysis

The morphology response variables, mean particle size (Z), polydispersity index (PdI) and zeta potential (ζ) of each DDS were determined by the Malvern Zetasizer Nano ZS. DLS techniques rely on the principle of random Brownian motion of particles, whereby the intensity of light scattered by particles fluctuates with their motion, and analysis of this short-term fluctuation yields the speed of motion (Hoo et al., 2008). Using the Stokes-Einstein relationship, this speed can be converted to size. Light scattering techniques assume homogenous suspensions of spherical particles, not accounting for particle agglomeration and or non-spherical morphologies (Danaei et al., 2018).

Analysis conditions were at 120 seconds equilibrating time, at a temperature of 25°C, with a He-Ne laser beam operating at a wavelength of 633 nm and a scattering angle of 90°. Sample preparation included ultrasonication for 30 minutes (high power, high frequency) and dilution (<0.01 wt%) with distilled water; all measurements were performed in triplicate. The intensity-weighted mean hydrodynamic diameter was determined from autocorrelation data peaks with a cumulant method programmed by the instrument software. PdI is a dimensionless number describing the breadth of the size distribution, ranging from 0 – 1 where ≤ 0.1 classifies a system as monodisperse, and > 0.4 as polydisperse (ISO, 2017). Zeta potential represents the charge and tendency of the system to aggregate, with $|\zeta| > 30$ mV indicating colloidal stability (Bhattacharjee, 2016).

3.5.2 Ultraviolet-visible spectroscopy

Binding efficiency (BE) of quercetin to the CTAB-modified NC was calculated according to Equation 3.2, with the amount of unbound quercetin quantified using UV-visible spectroscopy (Wallace et al., 2012). Quercetin displays maximum absorbance at a wavelength (λ_{max}) of 370 nm (He et al., 2012). The calibration curve produced with a dilution factor of 100 is provided in Figure A.2. The trendline was regressed linearly according to the Beer-Lambert Law, given in Equation 3.3, which is used to calculate sample concentration *C*. *A* represents the absorbance measured at a given wavelength, $b = 1$ is the path length of the sample, and ε is the molar absorptivity (the calculated gradient of the trendline). A coefficient of determination R^2 value of 99.3% indicated a good fit.

$$BE(\%) = \frac{[QT]_{added} - [QT]_{unbound}}{[QT]_{added}} \times 100 \quad [3.2]$$

$$A = \varepsilon bC \quad [3.3]$$

3.5.3 Microscopic imaging

The structure and morphologies of the NC, CTAB and quercetin, as well as their respective formulations, were imaged and examined by brightfield light microscopy (Zeiss Axiovision) and SEM (Zeiss EVO). Additionally, the autofluorescence of quercetin allowed for Total Internal Reflection Fluorescence (TIRF) microscopy (Zeiss LSM780). Analysis was performed by the Central Analytical Facilities (CAF) in the Chamber of Mines Building, Stellenbosch University. All SEM samples were sputter-coated with gold to provide adequate conductivity.

Chapter 4: Results and discussion

4.1 Effect of surfactant and drug concentration on delivery device properties

The interaction between CTAB and quercetin during formulation of each DDS was evident in the results obtained from the response surface design. The complete design matrices are given in Table B.1 and B.2 in Appendix B, with the means of each replicate summarised in Table 4.1. The change in each response between the levels of CTAB depended on the level of quercetin, and vice versa. For example, changing the CTAB concentration in the CNC design from its low (2 mM) level to its high (6 mM) level increased the mean zeta potential by 104% at the low (1 mg/mL) level of quercetin, compared to only 9% at the high (10 mg/mL) level of quercetin. This dependency and its practical implications for the DDSs are further discussed in the succeeding sections.

Table 4.1: Coded and uncoded design matrix, with the response values recorded at each factor combination, for the cellulose nanocrystals (CNC) and nanofibrils (CNF) system

	Factor					Response			
	Space	X_1	X_2	[CTAB] mM	[QT] mg/mL	Z (nm)	PdI	Zeta (mV)	BE (%)
CNC	F	-1	-1	2	1	6738	0.46	-33.9	35.4
	F	1	-1	6	1	4157	0.72	-16.6	44.8
	F	-1	1	2	10	3428	1.00	-18.8	93.1
	F	1	1	6	10	3708	0.66	-17.2	97.8
	A	-1	0	2	5.5	6969	0.92	-19.1	90.9
	A	1	0	6	5.5	7095	0.96	-14.5	90.5
	A	0	-1	4	1	8054	0.31	-18.5	49.9
	A	0	1	4	10	5416	0.85	-8.4	95.6
	C	0	0	4	5.5	4884	0.53	-14.0	85.6
CNF	Space	X_1	X_2	[CTAB] mM	[QT] mg/mL	Z (nm)	PdI	Zeta (mV)	BE (%)
	F	-1	-1	2	1	5127	0.63	-25.9	29.5
	F	1	-1	6	1	3980	0.82	-10.2	28.8
	F	-1	1	2	10	3546	0.96	-13.4	92.3
	F	1	1	6	10	4382	0.84	-11.9	98.1
	A	-1	0	2	5.5	4634	0.56	-6.5	93.1
	A	1	0	6	5.5	4610	0.33	1.6	93.3
	A	0	-1	4	1	4722	0.62	-8.2	71.3
	A	0	1	4	10	5074	0.81	0.7	95.0
	C	0	0	4	5.5	3467	0.69	-12.4	85.5

The second-order models fitted to each response and their significant effects are discussed in Section 4.1.1 and 4.1.2, with goodness-of-fit summarised in Section 4.1.3. Results from the CCD together with RSM optimisation tools in Minitab® allowed for determination of the CTAB and quercetin concentration that results in CNC and CNF DDSs with the most desirable size, charge, and binding efficiency, discussed in Section 4.1.4.

The mean centre-point (4 mM CTAB, 5.5 mg/mL) responses (Z, PdI, ζ, BE) were reported as 4884 nm, 0.53, –14.0 mV, 85.6% and 3467 nm, 0.69, –12.4.0 mV, 85.5%, for the CNC and CNF design, respectively. The design geometry of factorial and axial blocking, each with centre-point replicates, allowed for factor and block effects to be estimated independently. As seen in Table 4.2, CNC showed higher deviation between the centre-points than CNF, indicating that blocking of the CNC runs had a larger effect on the measured responses, and that the CNC DDSs recorded less consistent responses at constant experimental conditions. Moreover, ANOVA reported a significant ($p < 0.05$) block effect in the regressed models of Z and ζ in the CNC design, and ζ and BE in the CNF design.

Table 4.2: Mean factorial and axial centre-point responses recorded in the experimental design for cellulose nanocrystals (CNC) and cellulose nanofibrils (CNF)

Design	Space	Z	PdI	Zeta	BE
CNC	Factorial	3009	0.74	-18.9	87.2
	Axial	6759	0.33	-9.1	84.1
	Average	*4884*	*0.53*	*-14.0*	*85.6*
	Std. dev.	*2652*	*0.29*	*6.9*	*2.2*
CNF	Factorial	3892	0.69	-14.0	87.1
	Axial	3041	0.69	-10.76	84.0
	Average	*3467*	*0.69*	*-12.4*	*85.5*
	Std. dev.	*602*	*0.00*	*2.3*	*2.1*

4.1.1 Effect on size distribution and stability

4.1.1.1 Size and dispersity

Referring to the descriptive statistics of the CNC and CNF design summarised in Table 4.3 and 4.4, mean particle sizes reported to the micron range, with the two designs displaying similar Z values of 5533 nm and 4301 nm, respectively. Although this suggests that CNC formed on average larger aggregates than CNF, the standard deviation of the mean diameters recorded for CNC was 67% higher than those recorded for CNF.

Table 4.3: Descriptive statistics summary for each response recorded in the experimental design of the cellulose nanocrystals (CNC) system

Response	Valid N	Mean	Minimum	Maximum	Std. Dev.
Z	30	5533	2467	9881	2174
PdI	30	0.69	0.02	1.00	0.32
Zeta	30	-17.5	-38.0	-5.8	7.4
BE	30	76.9	29.5	99.3	23.4

Table 4.4: Descriptive statistics summary for each response recorded in the experimental design of the cellulose nanofibrils (CNF) system

Response	Valid N	Mean	Minimum	Maximum	Std. Dev.
Z	30	4301	2243	7588	1301
PdI	30	0.69	0.18	1.00	0.26
Zeta	30	-9.9	-27.2	5.2	8.2
BE	30	77.3	20.3	98.4	25.8

DLS techniques are based on the Stokes-Einstein relation, assuming that the particles undergoing analysis are spherical in shape and reporting an equivalent intensity-weighted mean hydrodynamic diameter, which overestimates the size of non-spherical particles with high aspect ratios (Karmakar, 2019), such as NC. Although DLS does not accurately represent the physical size of the aggregates, the numbers still allow for comparison of the colloidal stability of different samples, and offer some indication on whether discrete nanostructures are present or if there is a tendency to aggregate (Zheng, Bott & Huo, 2016). However, results from DLS and the regressed models represent the behaviour of poorly-defined aggregates in an aqueous environment. DLS techniques are convenient for routine characterisation of large sample batches and sample recovery, but should always be used in combination with other analytical methods (Zheng et al., 2016). Section 4.2 discusses the results of electron and fluorescent microscopy used to further investigate the size and shape of the dried particles.

A PdI < 0.70 is generally considered acceptable for potential DDSs (Danaei et al., 2018). However, only 43% and 50% of the respective CNC and CNF systems reported PdIs within this range. The Zetasizer is unable to measure the dispersity of a suspension with a PdI greater than 0.70, and reports a value of one. As seen in Table 4.3 and 4.4, the CNC and CNF designs both reported an averaged PdI of 0.69, within the measurable range, but indicative of broad size distributions. The minimum CNC PdI of 0.02 was much lower than the minimum CNF PdI of 0.18; the rod-like structure of CNC allows for the formation of more uniform suspensions than the long chains of CNF (Li et al., 2015; Hasan et al., 2020).

The coded effect of a factor on a response describes the magnitude and direction of change in the response due to a step change in the factor (Montgomery, 2012). The smaller the p-value the more significant the effect and the bigger the change in response due to a step change in the factor, and in the case of interaction, the more the relationship between a factor and response depends on changes in other factors (Montgomery, 2012).

Second-order response models were regressed according to Equation 3.1. The linear, quadratic and cross-product coded coefficients of each response model and their corresponding significance are provided in Table 4.5, with the full ANOVA results in Table B.3 and B.4 in Appendix B, and goodness-of-fit of each model compared in Section 4.1.3. In Table 4.5, it is shown that the mean particle size of the CNF design was not significantly affected by changes in concentration of either the surfactant or drug, whereas ANOVA of the measured CNC response data reported Z to be significantly ($p = 0.006$) affected by changes in quercetin concentration.

Table 4.5: Coded linear, quadratic and interaction coefficients and the statistical significance (alpha = 0.05) of their effect on each recorded response in the experimental design, for the cellulose nanocrystals (CNC) and cellulose nanofibrils (CNF) system

Term	Z (nm)		PdI		Zeta (mV)		BE (%)	
	Coded coeff.	p-value	Coded coeff.	p-value	Coded coeff.	p-value	Coded coeff.	p-value
CNC								
X_1	-362	0.310	-0.006	0.931	3.9	**0.000**	2.29	0.125
X_1^2	773	0.214	0.254	**0.036**	-4.0	**0.019**	0.75	0.766
X_2	-1066	**0.006**	0.171	**0.016**	4.1	**0.000**	26.07	**0.000**
X_2^2	476	0.439	-0.105	0.367	-0.6	0.695	-17.21	**0.000**
X_1X_2	715	0.108	-0.150	0.075	-3.9	**0.002**	-1.17	0.513
CNF								
X_1	-56	0.863	-0.025	0.642	4.23	**0.000**	0.90	0.729
X_1^2	352	0.531	-0.108	0.255	1.64	0.364	-4.13	0.362
X_2	-138	0.670	0.092	0.099	3.27	**0.004**	25.98	**0.000**
X_2^2	629	0.267	0.166	0.087	0.34	0.848	-14.11	**0.004**
X_1X_2	495	0.218	-0.077	0.251	-3.57	**0.009**	1.64	0.607

Factor 1 = CTAB concentration; Factor 2 = QT concentration; X = linear; X^2 = quadratic; X_1X_2 = cross-product

The same result is visible in the Pareto charts provided in Figure 4.1. Pareto charts aid in comparing the relative magnitudes of each effect, by plotting the standardised effects ranked according to their contribution to variation in the response, with a line drawn to

indicate at which point there is enough evidence to reject the null hypothesis and conclude that there is statistically significant ($p < 0.05$) association between the term and the response (Montgomery, 2012). Another method of visualisation is through normal plots of the standardised effects, where distance of a term from the straight line is proportional to its degree of significance (NIST & SEMATECH, 2012).

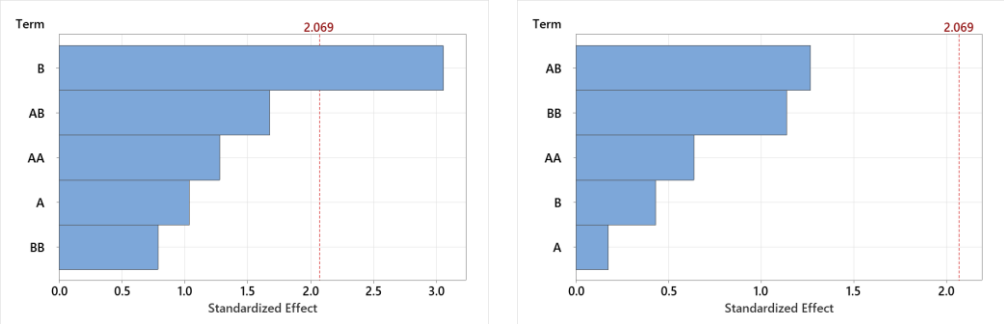

Figure 4.1: Pareto charts of the standardised linear surfactant (A) and drug (B) effect, quadratic surfactant (AA) and drug (BB) effect, and the effect of their interaction (AB), on the mean hydrodynamic diameter (Z) of cellulose nanocrystals (CNC) (left) and cellulose nanofibrils (CNF) (right), with a line indicating significance (alpha = 0.05)

The regression models (Equation 4.1) reported cross validation errors of 23.5% and 22.4% for CNC and CNF, respectively, indicating they were not suitable in describing the system. Moreover, the respective CNC and CNF models reported root-mean-square-errors (RMSEs) of 1482 nm and 1355 nm, which represent deviation between the observed data points and those predicted by the regression models (Devore, 2016). The limitations of DLS for aggregated systems with non-spherical structures undoubtedly contributed towards the failure of these models in predicting variation in the response.

$$Z_{CNC} = 12363 - 2164x_1 - 813x_2 + 193x_1^2 + 24x_2^2 + 80x_1x_2 \quad [4.1.1]$$

$$Z_{CNF} = 7552 - 1035x_1 - 592x_2 + 88x_1^2 + 31x_2^2 + 55x_1x_2 \quad [4.1.2]$$

Despite the differences between their determined significant effects, the visualised response surface of Z (Figure 4.2) was similar for the CNC and CNF designs. Worth noting is the synergistic effect between CTAB and quercetin at high levels in the upper right quadrant. This was hypothesised as a result of agglomeration at high surfactant levels (Jackson, 2011), together with recrystallisation of unbound quercetin in solution (Sun et al., 2012; Williams, Raimi-Abraham & Luo, 2018). At low (2 mM) CTAB concentrations mean particle size was shown to decrease with increasing quercetin added, most likely due to the presence of free unbound drug in suspension (Sun et al., 2012).

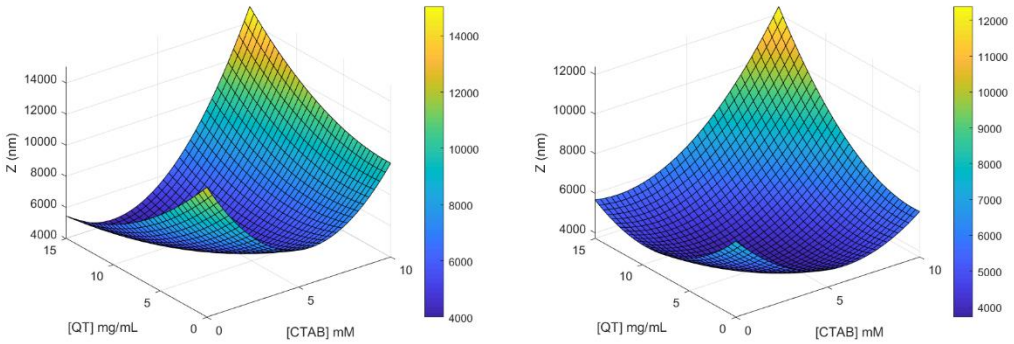

Figure 4.2: Response surface plots of the cellulose nanocrystals (CNC) (left) and cellulose nanofibrils (CNF) (right) predicting the mean hydrodynamic diameter (Z) with surfactant (CTAB) and quercetin (QT) concentration as independent variables

In a study by Zainuddin et al. (2019), TEM and XRD analysis revealed that modification of CNC with CTAB had no effect on the overall crystallinity (CrI decreased from 71.9% to 70.9%), but did slightly increase the mean particle size and decrease the aspect ratio (*L/D*) from 13.4 to 11.1. The obtained results were related to the attachment of bulky alkyl chains of CTAB that may have slightly increased the amorphous surfaces of the modified CTAB-CNC, having little consequence on their suitability as drug carriers.

In the case of the dispersity of the DDSs, ANOVA of the CNF design reported changing CTAB and drug concentration to have an insignificant ($p > 0.05$) effect on PdI. However, as reported in Table 4.5 and the Pareto charts in Figure 4.3 below, the PdIs of the CNC DDSs were significantly ($p = 0.016$) affected by quercetin concentration, and exhibited a significant ($p = 0.036$) curvilinear relationship with CTAB, concluding with 95% confidence that the coefficients for X_2 and X_1^2 are in fact non-zero.

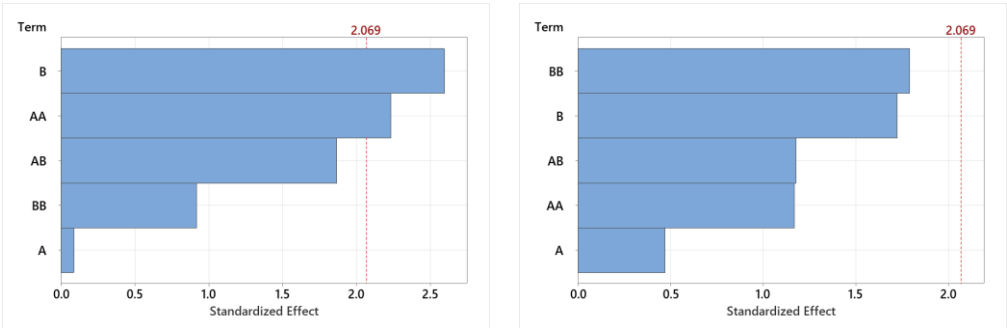

Figure 4.3: Pareto charts of the standardised linear surfactant (A) and drug (B) effect, quadratic surfactant (AA) and drug (BB) effect, and the effect of their interaction (AB), on the polydispersity index (PdI) of cellulose nanocrystals (CNC) (left) and cellulose nanofibrils (CNF) (right), with a line indicating significance (alpha = 0.05)

However, similar to the Z models discussed above, the regressed PdI models (Equation 4.2) of CNC and CNF reported cross validation errors of 17.7% and 17.2%, and RMSEs of 0.28 and 0.23, respectively. In addition to the limitations imposed by DLS, accurately determining the size distribution of biomaterials is challenging; complex morphologies in liquid media means that observed trends and patterns are often system-specific, associated with a high amount of random error (Bester, 2018).

$$PdI_{CNC} = 0.90 - 0.42x_1 + 0.16x_2 + 0.064x_1^2 - 0.005x_2^2 - 0.017x_1x_2 \quad [4.2.1]$$

$$PdI_{CNF} = 0.22 + 0.25x_1 - 0.035x_2 - 0.027x_1^2 + 0.008x_2^2 - 0.009x_1x_2 \quad [4.2.2]$$

The response surface plots are provided in Figure 4.4. A positive relationship between the dispersity of the suspension and increasing quercetin concentration was attributed to the widening of the size distributions with an increasing solids concentration (Sun et al., 2012). CNC and CNF both showed a curvilinear response to changing CTAB concentration, however in opposite directions – this discrepancy was hypothesised as a result of the poor fit of these regressed models, further discussed in Section 4.1.3.

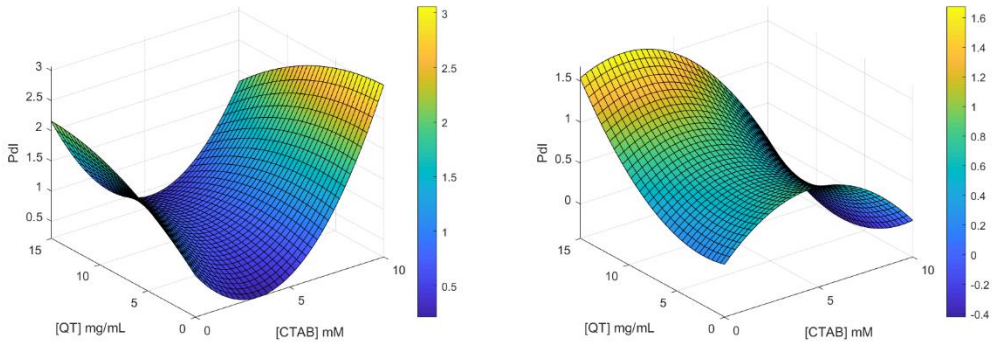

Figure 4.4: Response surface plots of the cellulose nanocrystals (CNC) (left) and cellulose nanofibrils (CNF) (right) predicting the polydispersity index (PdI) with surfactant (CTAB) and quercetin (QT) concentration as independent variables

4.1.1.2 Charge and stability

The magnitude of the absolute value of the zeta potential of a suspension is defined by the degree of electrostatic repulsion between particles; suspensions with large $|\zeta|$ values are electrically stable against aggregation, while dispersions with small $|\zeta|$ values tend have a high affinity for coagulation or flocculation (Gericke, Schulze & Heinze, 2020). Whether the value is positive or negative depends on the overall charge of the suspension.

According to Table 4.5, and as is depicted in the Pareto charts in Figure 4.5, the zeta potential of both the CNC and CNF design was significantly ($p < 0.05$) affected by changing CTAB and quercetin concentration, as well as their interaction. Furthermore, CNC exhibited a significant ($p = 0.019$) curvilinear relationship with CTAB.

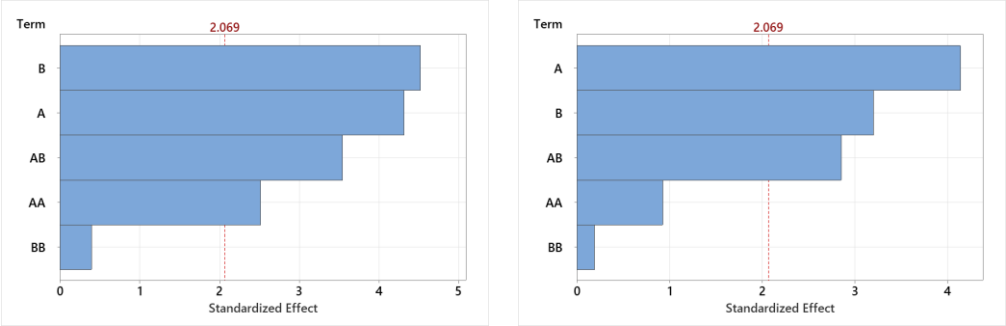

Figure 4.5: Figure 4.3: Pareto charts of the standardised linear surfactant (A) and drug (B) effect, quadratic surfactant (AA) and drug (BB) effect, and the effect of their interaction (AB), on the zeta potential (ζ) of cellulose nanocrystals (CNC) (left) and cellulose nanofibrils (CNF) (right), with a line indicating significance (alpha = 0.05)

The effect of CTAB and quercetin concentration on zeta potential is further evident in Figure 4.6a, which provides the main effects plots of each design. These plots display the means for each value of a factor, with a reference line drawn indicating the overall mean. Steep slopes exhibited by the lines connecting the means suggest significant main effects (Montgomery, 2012). Furthermore, the degree of non-parallelism displayed by the lines in the interaction plots in Figure 4.6b suggests strong interaction between the factors.

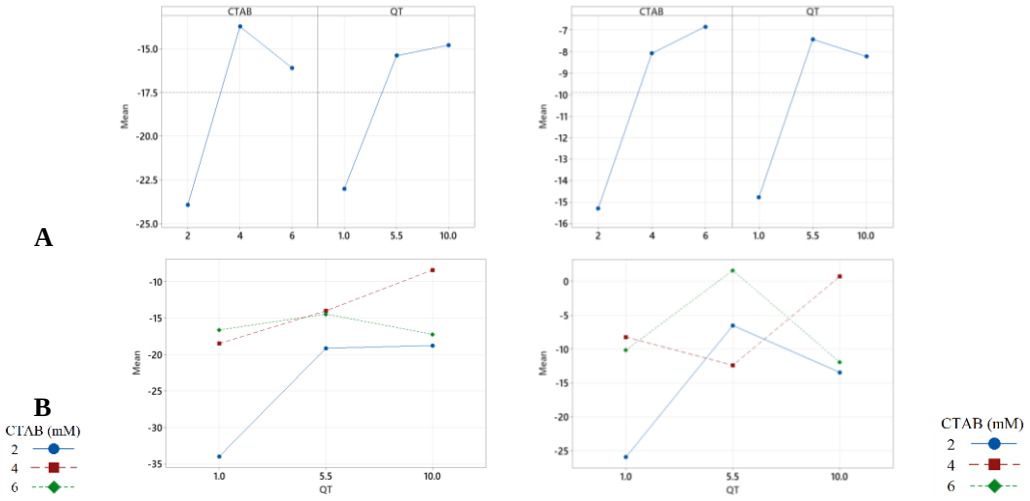

Figure 4.6: (a) Main effect and (b) interaction plots displaying the mean zeta potential (ζ) for every value of surfactant (CTAB) and quercetin (QT) concentration, for the cellulose nanocrystals (CNC) (left) and nanofibrils (CNF) (right) design

Alternatively, factorial main effects and interaction plots can be generated that display fitted means instead of data means. The regressed ζ response models are given in Equation 4.3. CNC and CNF reported cross validation experimental errors of 7.6% and 3.1%, and RMSEs of 3.9 mV and 4.3 mV, respectively, indicating their suitability in describing the system. The significant ($p < 0.05$) interaction between surfactant and drug is visible in the twisted planes of the surface plots in Figure 4.7.

$$\zeta_{CNC} = -54.0 + 12.3x_1 + 3.0x_2 - 1.0\,x_1^2 - 0.03x_2^2 - 0.44x_1x_2 \quad [4.3.1]$$

$$\zeta_{CNF} = -25.2 + 1.0x_1 + 2.1x_2 + 0.41\,x_1^2 + 0.02x_2^2 - 0.40x_1x_2 \quad [4.3.2]$$

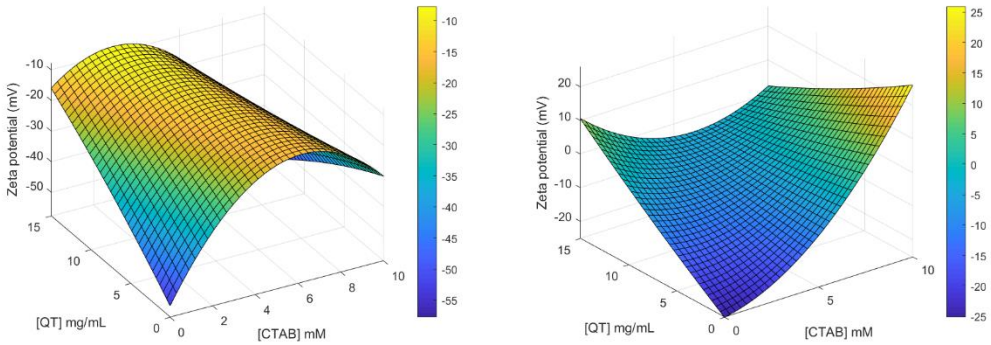

Figure 4.7: Response surface plots of the cellulose nanocrystals (CNC) (left) and cellulose nanofibrils (CNF) (right) predicting the zeta potential (ζ) with surfactant (CTAB) and quercetin (QT) concentration as independent variables

This interaction and the curvilinear response of zeta potential to changing CTAB concentration (visible in the CNC response surface) is likened to the interactions vastly covered in literature for complex formations between oppositely charged surfactants and polymers. The positive heads of CTAB electrostatically adsorb to either the available sulphate or carboxylate bonding sites on the NC surface (Alila et al., 2005, Abitbol et al., 2014), neutralizing the negative charges as zeta potential tends more positive (Jackson, 2011; Qing et al., 2016). However, above the critical micelle concentration (CMC, 0.93 mM for CTAB), the surfactant reassociates through alkyl tail interaction according to Figure 4.8. Monolayered (hemimicelle) and bilayered (admicelle) regions are formed, as well as free micelles in the bulk solution, due to the increase in entropy of the system when alkyl chains are removed from the aqueous phase (Hubbe, Rojas & Lucia, 2015; Tardy et al., 2017). These relative rates of formation are governed by the competing electrostatic repulsive forces between the positively charged surfactant heads and the attractive van der Waals forces between the long, C16 tails (Syverud et al., 2011; Xhanari et al., 2011).

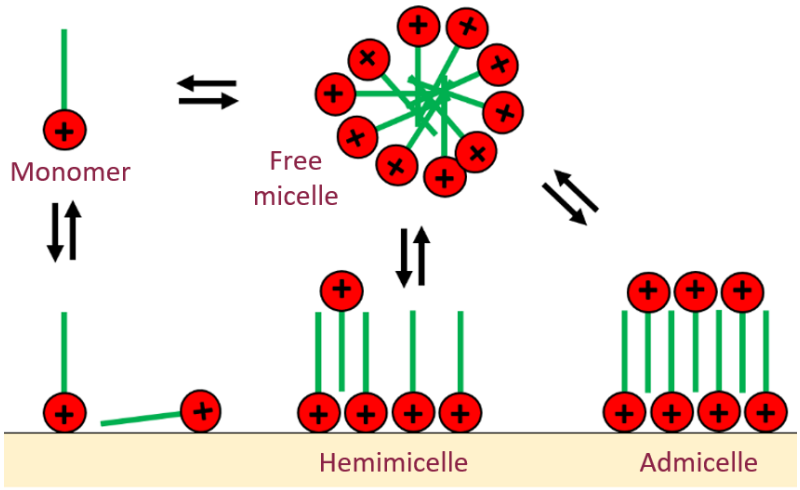

Figure 4.8: Schematic illustration of the possible stages of micelle formation and orientation of a cationic surfactant in solution, adsorbed onto an anionic cellulosic surface, redrawn from Hubbe et al. (2015)

As can be seen in Table B.2 in Appendix B, the CNF experimental runs labelled 19, 20, 25, and 27 recorded full charge reversals ($\zeta > 0$ mV). However, on average, the zeta potentials for both designs were negative, and not in magnitudes large enough to imply colloidal stability. Typically, systems with $|\zeta| > 30$ mV are considered stable, while $|\zeta| > 10$ mV is considered incipiently stable (Bhattacharjee, 2016). This was hypothesised as a result of micelle desorption during centrifugation and washing steps, exposing the anionic NC surface (Moon et al., 2011; Lunardi et al., 2021). Moreover, quercetin is a weakly acidic molecule with electro-active hydroxyl groups that can deprotonate in weakly alkaline water/ethanol solutions to display anionic surface charges (Pal & Saha, 2017).

Referring back to Table 4.3 and 4.4, the CNF systems on average exhibited more positive zeta potentials, with a mean ζ value of –9.9 mV compared to –17.5 mV reported for the CNC systems. It could be that the initial sulphated surface of CNC carried a stronger negative charge than the carboxylated surface of CNF, in agreement with recorded zeta potentials of –23.5 mV and –14.5 mV for CNC and CNF, respectively. The strength of a CNF functional group is highly dependent on the mechanical treatment and oxidation conditions (Rattaz et al., 2011), and as a result nanofibrillated cellulose may experience decreased electrostatic stabilisation due to weaker imparted surface charges (Moon et al., 2011). The ionic bonds between the surfactant heads and the NC surface are more permanent than van der Waals bonding between alkyl tails, and may be affected by various reaction conditions, such as pH and temperature (Alila et al., 2005; Tardy et al., 2017).

4.1.2 Effect on binding efficiency

Referring to the descriptive statistics in Table 4.3 and 4.4, both CNC and CNF reported a mean binding efficiency of 77% for the overall response surface design. This suggests that the two NC materials performed similarly as model drug carriers for quercetin through hydrophobic modification with a cationic surfactant. Recorded binding efficiencies ranged from 20.3% to 99.3%, with both CNC and CNF displaying a maximum at a CTAB and quercetin concentration of 6 mM and 10 mg/mL, and a minimum at a CTAB and quercetin concentrations of 2 mM and 1 mg/mL, respectively.

At centre-point conditions of 0.4 wt% polymer and 4 mM CTAB (polymer:surfactant ratio of 1:1), a mean quercetin binding efficiency of 86% was reported for both the CNC and CNF design. Raghav et al. (2020) studied different CTAB-modified polysaccharide supports as potential sustained release systems for curcumin, including carboxymethyl cellulose, pectin, alginate, and CNC. Recorded binding efficiencies ranged from 48 – 87%, with an experimental run of 1 wt% CNC and 10 mM CTAB (polymer:surfactant ratio of 1:1) reporting the maximum BE of 87% (Raghav et al., 2020).

A control run of 5.5 mg/mL quercetin in the absence of surfactant (0 mM CTAB) reported decreased quercetin binding efficiencies, confirming that the presence of a surfactant aids in facilitating the loading of NC with hydrophobic drugs. The CNF-QT and CNC-QT formulations reported binding efficiencies of 69% and 76%, respectively, indicating that in the absence of surfactant CNF experienced less efficient binding than CNC. This could be partially due to carboxylate groups deposited onto the CNF surface during TEMPO-oxidation that imparted hydrophilicity, leading to weaker hydrophobic interactions with quercetin than the sulphate groups of CNC (Hasan et al., 2020). However, Zainuddin et al. (2017) reported a curcumin binding efficiency of 27% for a 0 mM CTAB control run of a CNC-CTAB formulation, and Li et al. (2019) reported a quercetin binding efficiency of 89% for a CNF-QT formulation studied in the absence of any surfactant.

ANOVA of the FFD reported significant ($p < 0.05$) curvature in the BE response. In agreement, ANOVA of the CCD (Table 4.5) reported the regressed BE model (Equation 4.4) to show a significant ($p < 0.05$) curvilinear response to changing quercetin concentration. CNC and CNF reported cross validation errors of 4.4% and 5.5%, and RSMEs of 6.1% and 10.9%, respectively, indicating similar suitability in describing the system. The Pareto charts in Figure 4.9 rank the magnitudes of each effect in the models.

$$BE_{CNC} = 24.8 + 0.36x_1 + 15.7x_2 + 0.19x_1^2 - 0.85x_2^2 - 0.13x_1x_2 \quad [4.4.1]$$

$$BE_{CNF} = 21.1 + 7.7x_1 + 12.7x_2 - 1.0x_1^2 - 0.70x_2^2 + 0.18x_1x_2 \quad [4.4.2]$$

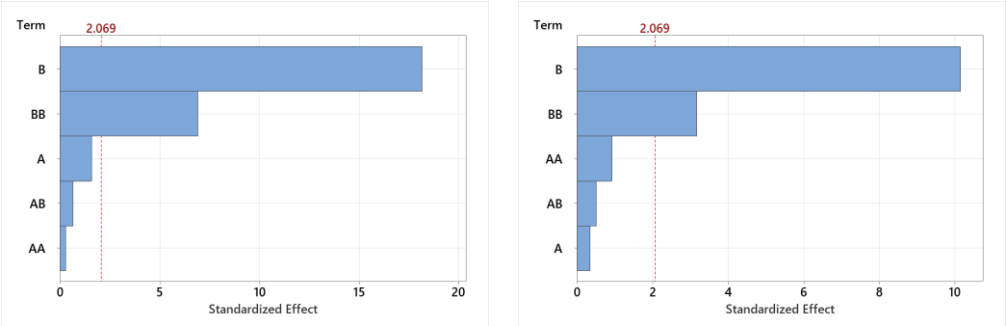

Figure 4.9: Pareto charts of the standardised linear surfactant (A) and drug (B) effect, quadratic surfactant (AA) and drug (BB) effect, and the effect of their interaction (AB), on the drug binding efficiency (BE) of cellulose nanocrystals (CNC) (left) and cellulose nanofibrils (CNF) (right), with a line indicating significance (alpha = 0.05)

The curvilinear relationship between the binding of a model drug and the drug concentration itself has been previously reported (Zainuddin et al., 2017; Gupta & Raghav, 2020), where the amount of drug bound increased in a concentration-dependent manner until reaching a steady state, plateauing once all available bonding sites are filled. Increasing concentration beyond this point can increase the presence of free unbound quercetin that remains in the supernatant post-centrifugation (6000 rpm, 15 min), thereby lowering the calculated binding efficiency. This phenomenon is visible in the response surface plots in Figure 4.10, and was observed regardless of surfactant concentration, hence the insignificant ($p < 0.05$) interaction terms.

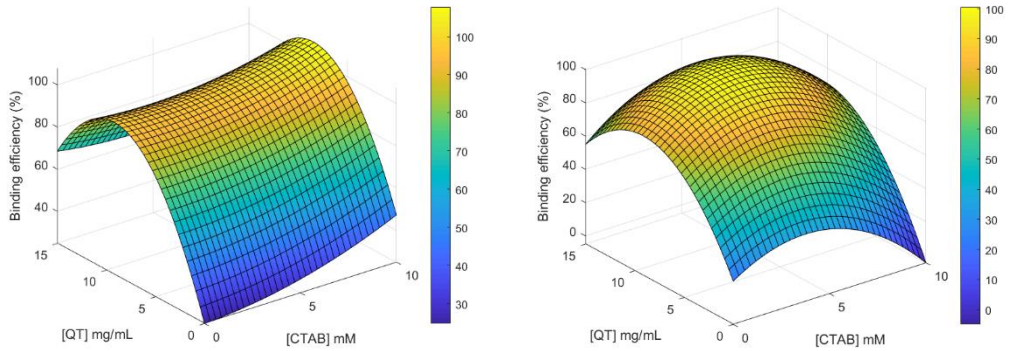

Figure 4.10: Response surface plots of the cellulose nanocrystals (CNC) (left) and cellulose nanofibrils (CNF) (right) predicting the binding efficiency (BE) with surfactant (CTAB) and quercetin (QT) concentration as independent variables

Gupta & Raghav (2020) prepared CNC-CTAB formulations, loaded with various hydrophobic NSAIDs, and found that in each case drug binding efficiency increased with drug concentration, before starting to plateau. The maximum binding efficiencies ranged from 40 – 60%, and corresponded to the octanol-water partition coefficient (log P value) of the drug (Gupta & Raghav, 2020). This value expresses the lipophilicity of a compound as the ratio of its concentration in a water-saturated octanolic phase to its concentration in an octanol-saturated aqueous phase, at a neutral pH.

More hydrophobic drugs (e.g. ibuprofen, etodolac, diclofenac) with higher log P values facilitated more efficient binding compared to less hydrophobic drugs (e.g. paracetamol) with lower log P values (Gupta & Raghav, 2020). Quercetin is one of the least lipophilic flavonoids, possessing a log P = 1.82 ± 0.32 (Rothwell, Day & Morgan, 2005), relatively low compared to that of curcumin and typical NSAIDs, which possess a log P ≈ 3 (Priyadarsini, 2014; Czyrski, 2019). This is one of the reasons for the strong dependency of binding efficiency on the quantity of quercetin added during loading.

The curvilinear response of BE to increasing surfactant is well explained by the changing availability of bonding sites with micelle formation, as depicted in Figure 4.8. As hydrophobicity increased with increasing surfactant concentration, BE likely increased as a result quercetin attaching to the available alkyl tails. The extent of hydrophobicity, aggregation and quercetin co-adsorption is determined by the relative rates of formation of hydrophobic (hemimicelle) and hydrophilic (admicelle regions), as well as free micelles forming in solution (Alila et al., 2005; Xhanari et al., 2011; Tardy et al., 2017).

The decrease in BE at higher surfactant concentrations was hypothesised as a result of micelle desorption during centrifugation and washing steps, reducing the available surface area for hydrophobic interaction with quercetin (Song et al., 2011; Hubbe et al., 2015; Lunardi et al., 2017). Moreover, quercetin that had gravitated towards the hydrophobic cores of these detached micelles was subsequently removed.

The long C16 alkyl tails of CTAB are particularly conducive to self-assembly, as hydrophobic interactions are stronger between aliphatic molecules compared to aromatic, and are directly proportional to the number of carbon atoms in the alkyl chain (Tardy et al., 2017). This curvilinear relationship was not as apparent in CNC than it was in CNF, possibly due to the surfactant having more permanent ionic bonds with the sulphated CNC surface, thus experiencing reduced micelle desorption and quercetin removal.

Zainuddin et al. (2017) prepared hydrophobic CNC through modification with CTAB, and investigated the effect of changing surfactant concentration on the DS of the surfactant and curcumin binding. Figure 4.11 graphs the reported curcumin binding efficiencies against CTAB concentration, as well as the calculated DS values based on the percentage of nitrogen from the CTAB trimethylammonium groups. It is clear that binding efficiency is directly proportional to the DS of CTAB, with a lower DS presumably resulting in fewer binding sites for quercetin attachment. Both factors displayed a curvilinear response to increasing surfactant concentration and reached an optimum at 4 mM CTAB. Increasing the concentration of CTAB beyond this resulted in surfactant desorption, a decrease in DS, and a resulting decrease in BE (Zainuddin et al., 2017).

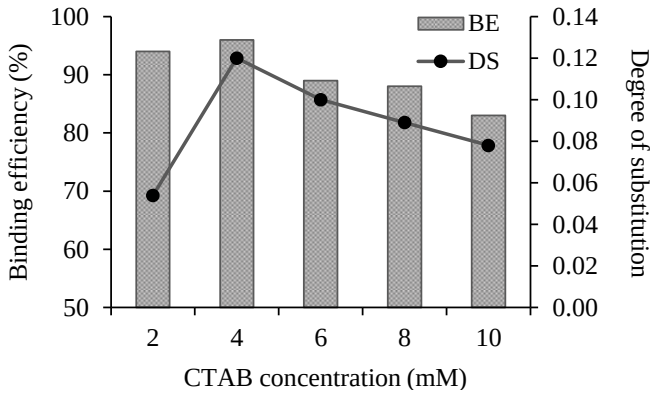

Figure 4.11: The relationship between surfactant (CTAB) concentration, degree of substition (DS) of the surfactant, and curcumin binding efficiency (BE), graphed using results produced by Zainuddin et al. (2017)

4.1.3 Goodness-of-fit analysis

The goodness-of-fit statistics for each model are summarised in Table 4.6 below, with $R^2 > 75\%$ considered to be indicative of a good fit (Haaland, 1989). Predicted R^2 represents the ability of the model to predict the response for new observations, and is used to verify that the model captures significant changes in the response variable, but not the random experimental noise (Devore 2016). Model reduction can be performed by sequentially removing the insignificant terms, thereafter adjusted R^2 is used to compare models containing different numbers of terms. The regressed Z and PdI models exhibited poor (< 75%) coefficients of determination, specifically the CNF systems, reporting R^2 values of 14.0% and 38.2%, respectively, explaining less than 50% of the variation in the response (Devore, 2016). Moreover, large cross validation and root-mean-square errors indicates that these models were not suitable in describing size distributions of the systems.

Table 4.6: Coefficient of determination and lack-of-fit p-values for the regressed response models of the cellulose nanocrystals (CNC) and cellulose nanofibrils (CNF) design

CNC					CNF				
Model	R^2	R^2 (adj)	R^2 (pred)	Lack-of-fit p-value	Model	R^2	R^2 (adj)	R^2 (pred)	Lack-of-fit p-value
Z	63.17	53.56	37.25	0.744	Z	13.97	0.00	0.00	0.420
PdI	41.34	26.04	0.56	0.095	PdI	38.15	22.01	0.00	0.499
Zeta	78.46	72.85	62.86	0.188	Zeta	77.65	71.81	63.45	0.039
BE	94.60	93.19	90.34	0.069	BE	85.89	82.20	76.31	0.000

The lack-of-fit test expresses the residual error in comparison to the pure error, where a significant ($p < 0.05$) lack-of-fit indicates that there might be a contribution in the regressor-response relationship that is not accounted for by the current model (Chen, Lee & Abd Hamid, 2017), indicating the need for additional or higher-order terms to better describe variation in the response. The Z and PdI models for each design yielded insignificant ($p > 0.05$) lack-of-fit test statistics, suggesting that the lack-of-fit in each response occurred due to the noise in the results, and that the fitted model terms were the best available at modelling the variation in the response. This is to say that the models would not necessarily benefit from additional or high-order terms.

Reasonably large deviation between the factorial and axial centre-point runs (see Table 4.2) confirms that the DOE results included notable experimental error. Low (~0%) predicted R^2 values indicates that these models are not representative of the larger population (Devore, 2016), and are therefore over-fit. In order to verify whether the developed models met the necessary assumptions of ANOVA, analysis of the residuals (the difference between the experimental and predicted data points) was performed.

Histograms and normal probability plots of the residuals, as well as plots of the residuals versus the observation order and fitted values were generated, and are given in Figure B.1 to B.4 in Appendix B, respectively. The normality of the residuals was assessed through normal probability plots, as histograms are considered ineffective at reliably representing skewness or outliers in results for small sample sizes (Devore, 2016).

Normal probability plots display the residuals versus their expected values under a normal distribution, and in the case of the Z and PdI responses in each design, the residuals all followed a relatively straight line (save for a few outliers), indicative of a normal distribution. The residuals versus fits plots displayed points that fall randomly on both sides of zero with no discernible patterns, satisfying the assumption of constant variance.

Similarly, the residuals versus observation order plots showed no recognizable trends or cycles, satisfying the assumption that the residuals are not correlated, and thus, are independent of each other (Montgomery, 2012). It should be noted that the Kolmogorov-Smirnov test for the recorded PdIs of the CNC systems concluded that the data was non-normally distributed, as is clear in the plot provided in Figure 4.12, where data with a normal distribution would typically fall along the straight line. Box-Cox transformations can be employed in an attempt to transform the data into a normally distributed dataset pre-processing, otherwise another potential solution could be to utilise non-parametric statistical tests in place of traditional ANOVA.

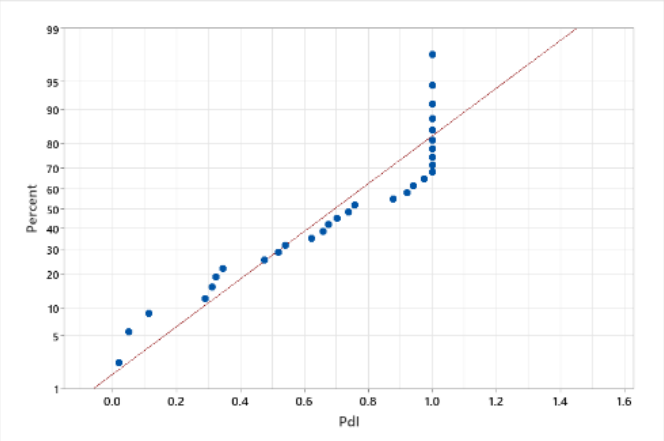

Figure 4.12: Normal probability plot produced from the Kolmogorov-Smirnov normality test performed on the polydispersity index (PdI) response data collected for the cellulose nanocrystals (CNC) (KS = 0.190, $p < 0.01$)

The ζ models of the CNC and CNF design reported R^2 values of 78.5% and 77.7%, respectively, indicative of moderately good fits (Haaland, 1989). However, the CNF model reported a significant ($p = 0.039$) lack-of-fit with an F-statistic of 3.37, suggesting that the model could possibly be improved by additional/higher-order terms. The four-by-four residual analysis (see Figure B.3) showed no patterns or trends that warrant concern, providing enough evidence to conclude that ANOVA assumptions of normality, constant variance and independence were met. Kolmogorov-Smirnov test statistics of 0.117 and 0.083 obtained for the CNC and CNF systems, respectively, concluded that the collected ζ response data followed a relatively normal distribution. Cross validation errors below 10% and RMSEs less than 5 mV indicate that these models accurately described the system.

The reported R^2 values for binding efficiency in the CNC and CNF systems were 94.6% and 85.9%, respectively, both indicative of good model fits (Haaland, 1989), and in

agreement with low cross validation and root-mean-square errors. A lack-of-fit test statistic approaching significance ($p = 0.069$) with a corresponding F-value of 2.76 for CNC suggests that these model terms were the best available at fitting the data, whereas a highly significant ($p = 0.000$) lack-of-fit test statistic with a relatively large F-value of 40.13 for CNF indicates that variation in the BE response might be better explained by a higher-order model, hence the lower coefficient of determination.

Although BE reported the largest coefficients of determination amongst the measured responses, the data sets of both polymers reported notably significant ($p < 0.01$) Kolmogorov-Smirnov test statistics of 0.284 (CNC) and 0.292 (CNF), indicative of non-normal distributions. Analysis of the residuals (see Figure B.4) was in agreement, with the normal probability plots exhibiting changing slopes, specifically inverted S-shaped curves indicative of distributions with short tails and possibly an unidentified variable. Plots of the residuals versus fits displayed a large shift and slight fanning (narrowing residual scatter along the x-axis), indicative of non-constant variance (Devore, 2016).

Plots of the residuals versus observation order displayed slight cycling trends with respect to the centre line (especially within the CNF design), indicative of correlation amongst the residuals. The Kolmogorov-Smirnov test together with the four-by-four residual analysis for each design provided sufficient evidence to reject the null hypothesis that the response data of binding efficiency followed a normal distribution, and conclude that the assumptions of ANOVA were not satisfactorily met.

4.1.4 Optimisation

Once characterisation of the system responses was complete and the models were regressed, RSM optimisation tools in MINITAB® were employed to determine the CTAB and quercetin concentration that minimises Z, PdI, and ζ, while maximizing BE. A multiple response optimisation technique developed by Derringer and Suich (1980) makes use of desirability functions, by transforming each response model y_i (Equation 3.1) into an individual desirability function d_i between zero (outside of acceptable limits) and one (ideal case), with the factors calculated to maximise the composite desirability function D (Equation 4.5), a weighted geometric mean for m responses (Montgomery, 2012).

$$D = (d_1 \cdot d_2 \cdot \cdots d_m)^{1/m} \qquad [4.5]$$

Contour plots illustrating the relative maximum and minimum regions in each regressed response surface are given in Figures B.5 to B.8 in Appendix B. Elliptical contour plots indicate considerable interaction between factors, whereas circular plots indicate less prominent interaction (Montgomery, 2012). Results of the single-response optimisations are given in Table 4.7, where factor settings were determined by how effective they were at optimising the desirability function of an individual response.

Table 4.7: Fitted response values and the corresponding surfactant (CTAB) and quercetin (QT) concentration predicted from single-response optimisation of the cellulose nanocrystals (CNC) and cellulose nanofibrils (CNF) design

Response	CNC			Response	CNF		
	Fit	CTAB	QT		Fit	CTAB	QT
Z	4154 nm	3.54	10.00	Z	3705 nm	4.00	6.00
PdI	0.31	3.41	1.00	PdI	0.53	6.00	5.27
Zeta	-31.3 mV	2.00	1.00	Zeta	-20.2 mV	2.00	1.00
BE	98.9%	6.00	8.73	BE	100.0%	4.59	9.73

However, for the purpose of this study, multi-response optimisation was more appropriate, where factor settings were determined by how effective they were at optimising all four responses simultaneously. Results of this optimisation are given in Table 4.8, with accompanying desirability plots in Figure 4.13.

Table 4.8: Fitted response values and composite desirabilities, and the corresponding surfactant (CTAB) and quercetin (QT) concentration predicted from multi-response optimisation of the cellulose nanocrystals (CNC) and cellulose nanofibrils (CNF) design

Response	CNC		CNF	
	Individual desirability	Fit	Individual desirability	Fit
Z	0.60	5436 nm	0.63	4183 nm
PdI	0.44	0.56	0.53	0.56
Zeta	0.39	–18.3 mV	0.60	-14.3 mV
BE	0.68	76.9%	0.77	80.8%
	Composite desirability = 0.51 CTAB = 3.3 mM QT = 4.2 mg/mL		Composite desirability = 0.63 CTAB = 2.0 mM QT = 5.1 mg/mL	

The design optimisation was validated by performing triplicate experimental runs at the predicted optimal factor settings, measuring the responses and calculating experimental error. These results are presented in Table 4.9. The CNC validation resulted in an experimental error of 18.2%, in comparison to 9.9% obtained for CNF. These values are reasonably low (within the acceptable range of 10–20%), and in agreement with the lower CNC composite desirability of 0.51 in comparison to the CNF desirability of 0.63.

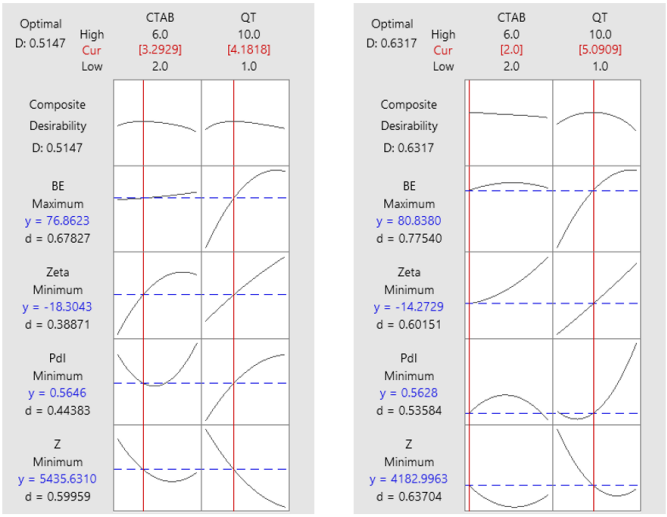

Figure 4.13: Multi-response optimisation desirability plots generated for the CNC (left) and CNF (right) systems, with mean hydrodynamic diameter (Z), polydispersity index (PdI) and zeta potential (ζ) minimised, and binding efficiency (BE) maximised, with surfactant (CTAB) and quercetin (QT) concentration as independent variables

Table 4.9: Comparison of predicted and experimental response values, with the corresponding percentage error, as design validation for the multi-response optimisation of the cellulose nanocrystals (CNC) and cellulose nanofibrils (CNF) systems

Polymer	Response							
	Z (nm)		PdI		ζ (mV)		BE (%)	
	Pred.	Exp.	Pred.	Exp.	Pred.	Exp.	Pred.	Exp.
CNC	5436	4414	0.56	0.41	-18.3	-20.5	76.9	65.1
% error	18.8		26.8		12.0		15.3	
CNF	4183	3307	0.56	0.53	-14.3	-13.2	80.8	85.2
% error	20.9		5.4		7.7		5.4	

4.2 Development of a method for modifying nanocellulose for hydrophobic drug delivery

NC suspensions have been reported to display elastic, gel-like behaviour at high concentrations, and viscous, liquid-like behaviour at low concentrations (Li et al., 2015). CNF-based suspensions in particular exhibit complex rheological properties and have extensively been reviewed in literature (Löbmann & Svagan, 2017). Their properties depend both on the network characteristics and flocculation of the nanofibres, as well as the uniformity of the size distribution (Hubbe, 2007), which is determined by the cellulose source and processing conditions of the extracted CNF. Although CNC is typically produced via acid hydrolysis of pulp, filter paper or other cellulosic material, it can also be

extracted from CNF, by removing the amorphous regions that connect the shorter, more crystalline segments (Habibi, Lucia & Rojas, 2010). Due to this reduction in dimension and disentanglement of the fibrous network, CNC often display a significant loss of rheological properties in comparison to CNF (Löbmann & Svagan, 2017).

A homogenous dispersion is obtained by using an appropriate solvent and mixing techniques, and it has been reported that unmodified CNF shows a high affinity for aggregation in solvents other than water (Eichhorn et al., 2010; Löbmann & Svagan, 2017). Figure A.3 in Appendix A shows the prepared liquid suspensions of 0.4 wt% CNC and CNF, as well as their respective CTAB-QT formulations. Additionally, freeze-drying of the unmodified NC was investigated (see Figure A.4), but as previously observed (Lavoine et al., 2012), the texture of the solid material was irreversibly plasticised, due to hydrogen bonds between the nanofibres becoming disrupted by water molecules (Peng, Gardner & Han, 2012). The tendency of the fibres to self-associate and form nanofibre agglomerates has been attributed to the strongly interacting surface hydroxyl groups (Dufresne, 2013).

4.2.1 Modification with CTAB

After completion of 30 experimental runs per polymer for the experimental design, particle size analysis reported mean hydrodynamic diameters of 5533 nm and 4301 nm for the respective CNC and CNF formulations. However, as discussed, the accuracy of DLS is limited for non-spherical systems with high aspect ratios. NC networks may consist of fibres with varying nanos-sized diameters, up to several micrometers in length (Karmakar, 2019). Moreover, modification with CTAB rendered the NC surface hydrophobic and led to aggregates with a poorly defined structure in aqueous solution. A mean PdI of 0.69 reported for both polymer designs implied polydisperse systems (Danaei et al., 2018), and measured sample size distributions (Figure 4.14) showed broad spectrums, suggesting the presence of smaller NPs among larger microparticles and agglomerates.

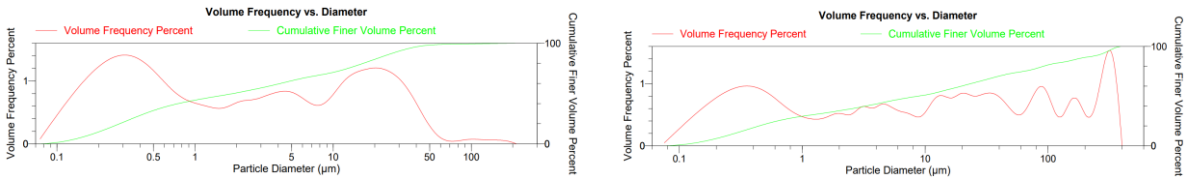

Figure 4.14: Size distribution by volume frequency percent of mean hydrodynamic diameter (Z), for the cellulose nanocrystals (CNC) (left) and cellulose nanofibrils (CNF) (right), formulated at a surfactant (CTAB) and quercetin (QT) concentration of 2 mM and 10 mg/mL, respectively

Sequential microfiltration of 10 µm, 1 µm, and 0.45 µm was investigated for potential improvement and narrowing of the centre-point size distributions, with the upper pore size cut-off chosen as 10 µm considering the maximum recorded Z value of 9811 nm. Microfiltration was successful in filtering off the size range above 10 µm. However, light and fluorescent microscopy (Figure C.1 in Appendix C) revealed significant filter blockage at 1 µm and 0.45 µm, attributed to the high aspect ratios and aggregation of the fibres.

Brightfield and fluorescent microscopy of the respective CNC and CNF formulations (Figure 4.15) showed that quercetin was both amorphously dispersed throughout the NC networks, as well as recrystallised as large, rod-shaped microparticles. Interestingly, quercetin fluoresced in its amorphous state or when particularly large aggregates clustered together (see Figure C.2), but the fluorescence intensity of the smaller, individualised and unbound particles was too low to detect.

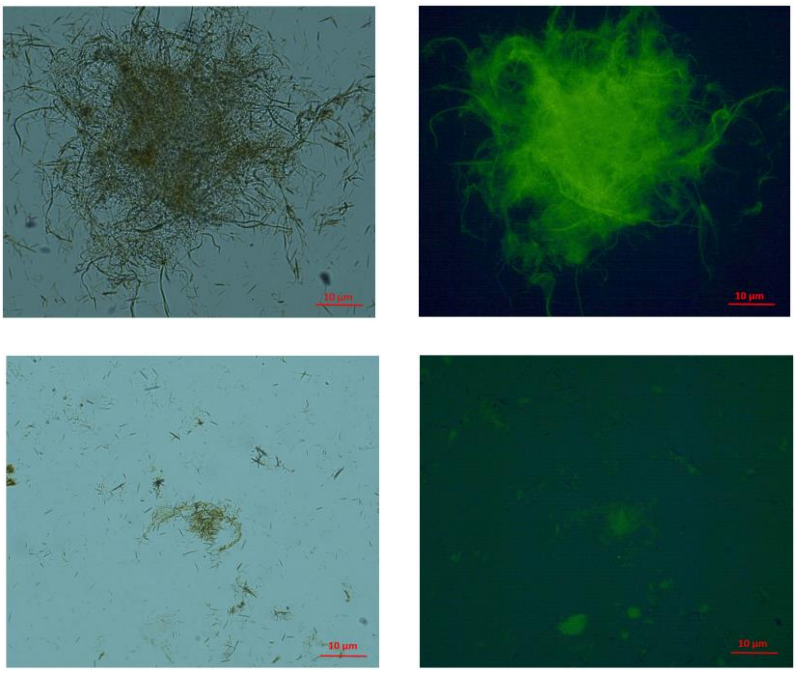

Figure 4.15: Brightfield (left) and fluorescent (right) micrographs of unfiltered cellulose nanocrystals (CNF) (top) and cellulose nanofibrils (CNC) (bottom), modified with a surfactant (CTAB) and quercetin (QT) concentration of 4 mM and 5.5 mg/mL, respectively (scale bar 10 µm)

The progressive series of CNC, CNC-CTAB and CNC-CTAB-QT micrographs in Figure 4.16 shows the aggregation of CNC particles after the addition of CTAB, and the subsequent clustering of quercetin onto these aggregates. Physical entanglement governs

aggregation in CNF, due to high aspect ratios and flexibility even at low concentrations, whereas aggregation of CNC is mainly due to hydrogen bonding between the surface groups, together with strong ionic interactions with the surfactant and as a result hydrophobic agglomeration in aqueous solution (Li et al., 2015).

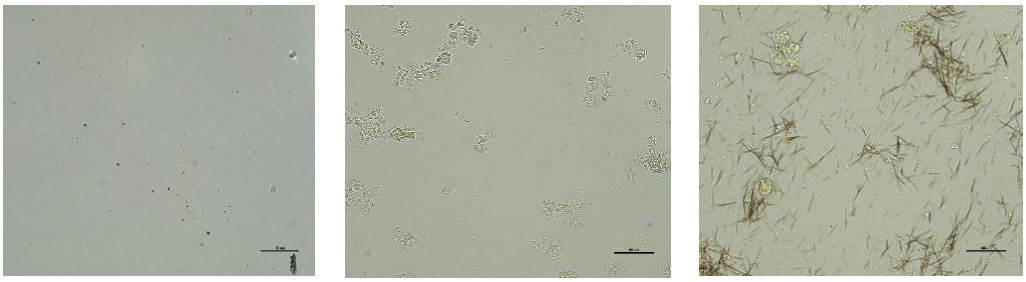

Figure 4.16: Progressive light microscopy of unmodified cellulose nanocrystals (CNC) (left), CNC modified with surfactant (CTAB) (middle), and CNC-CTAB loaded with quercetin (QT) (right) (scale bar 100 µm)

4.2.2 Protocol adaption

In an attempt at particle size and PdI improvement, the protocol was adapted to include an initial homogenisation step of the prepared quercetin, CNC and CNF stock solutions. The suspensions were homogenised at 24 000 rpm for six minutes (Xhanari et al., 2011; Karadag et al., 2014; Furtado et al., 2021), in two-minute intervals and suspended in a cool water bath to avoid excessive temperature increase above the degradation temperature of quercetin, 37 ºC (Wang & Zhao, 2016; Chaaban et al., 2017).

A repeat experiment of CNC- and CNF-CTAB-QT formulations prepared with these solutions at centre-point conditions (4 mM CTAB and 5.5 mg/mL QT) was performed, and further investigation into the morphology was carried out by SEM analysis. From DLS, unmodified CNC and CNF reported mean hydrodynamic particle sizes of 4521 nm and 3578 nm, respectively; after homogenisation and 30 minutes of ultrasonication pre-analysis, a reduction of about 50% was seen in each material, reporting new mean sizes of 2133 nm and 1736 nm, respectively.

In agreement with TEM micrographs of CNF prepared by Li et al. (2015), the SEM results in Figure 4.17 showed the structure of CNF as individual fibres with varying nano-sized widths and lengths up to several micrometers, entangling to form a network. The aggregation and bundling of the fibres may have been partially accelerated as a result of drying steps during sample preparation (Eichhorn et al., 2010; Peng et al., 2012).

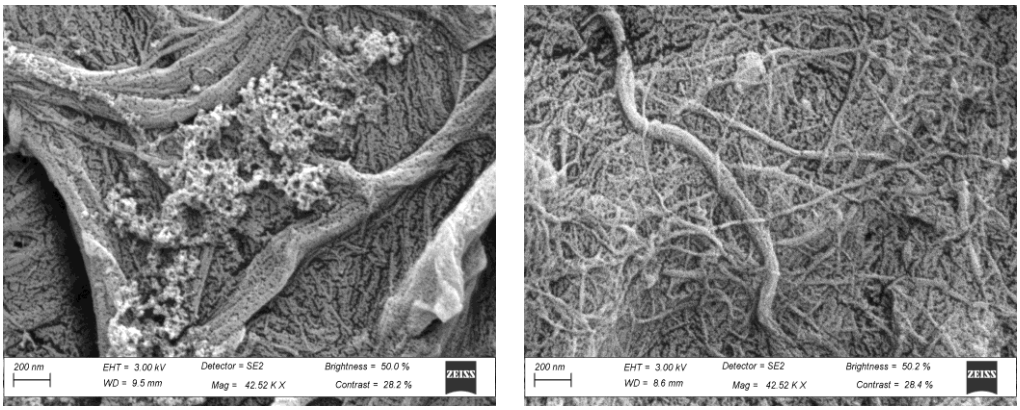

Figure 4.17: SEM micrographs of an unmodified (left) and homogenised (right) 0.4 wt% cellulose nanofibrils (CNF) suspension (scale bar 200 nm)

Homogenisation seemed to have little influence on the network-like structure of CNF, however led to considerable delamination of the larger bundles and a decrease in fibre diameter. A similar lack of substantial trends in the size distributions of NC has been reported by other researchers (Bester, 2018), whereby high-shear homogenisation had little effect on particles below 1000 nm. Similar to previous observations (Habibi et al., 2010; Deepa et al., 2015), fibre diameter varied considerably, and exact fibril length was not able to be measured, due to overlapping and inter-fibrillar attraction between the bundles, creating a “bird nest” (Bhutiya et al., 2020) structure.

Rather than displaying the expected needle-like rod shape characteristic of crystalline NC, obtained SEM images of both the unmodified and homogenised CNC (Figure C.3 in Appendix C) showed a highly aggregated, fibrous network structure, similar to CNF. It is possible that the obtained liquid CNC stock suspension from Sappi that was used in previous experimental runs had initially undergone insufficient acid hydrolysis (Li et al., 2015), leading to incomplete nanofibre defibrillation and size reduction, and as a result a structure similar to CNF. This could also explain the similarities observed in the size and dispersity of the two materials, as discussed in Section 4.1.

The CNC-CTAB-QT formulation was repeated at centre-point conditions, using a previously freeze-dried CNC powder obtained from the University of Maine, that reported Z = 153 nm. Its SEM imaging (Figure 4.18) was in agreement with a previously observed CNC morphology (Lu & Hsieh, 2012; Jiang & Hsieh, 2013) of individual NPs aggregating into thin, lamellar planes. This has been attributed to hydrogen bonding and the formation of an ordered chiral nematic structure upon lyophilisation (Han et al., 2013)

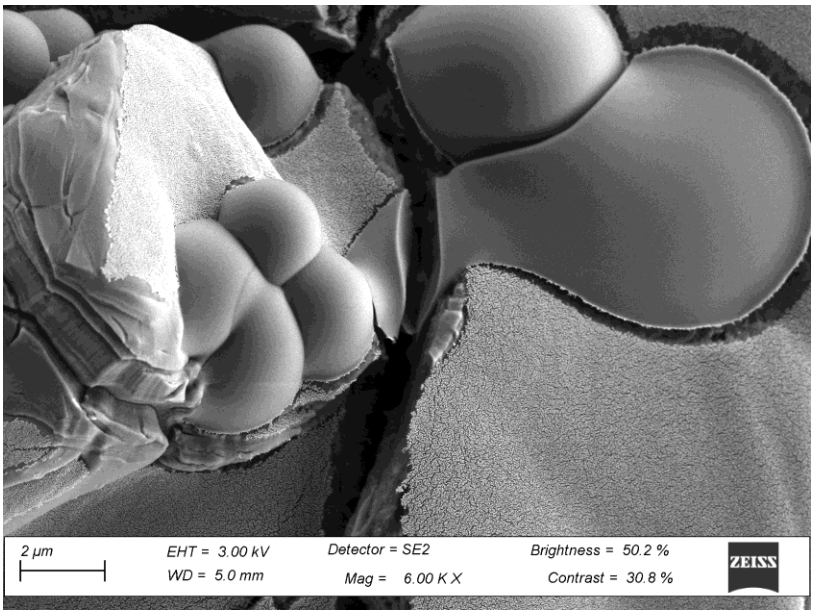

Figure 4.18: SEM micrograph of an unmodified, previously freeze-dried cellulose nanocrystals (CNC) powder, redispersed as a 0.4 wt% suspension (scale bar 2 µm)

When considering the adsorption of a cationic surfactant onto a non-ionic cellulosic material, the interaction is comparable to that observed for other hydrophilic, hydroxylated surfaces, such as silica (Penfold et al., 2007). When considering the adsorption of a cationic surfactant onto an anionic cellulosic material, the interaction is mainly due to electrostatic interaction (Tardy et al., 2017). Because of the non-covalent nature and fast kinetics of this interaction, customising the characteristics of NC DDSs by this approach is viewed as simpler and more cost-effective than conventional chemical routes (Tardy et al., 2017). However, the interaction of cationic surfactants with NC strongly depends on the source cellulose and charge density, as well as the surfactant structure and hydrophobicity. Moreover, it can be influenced by pH and ionic strength (Zainuddin et al., 2017). Increasing the anionic surface charge of NC has been well-studied and correlated with the increased adsorption of cationic surfactants (Alila et al., 2005).

Typically, mechanically-produced CNF show less active surface characteristics, with lower zeta potentials and fewer functional surface groups than acid-hydrolysed CNC, stabilised by abundant sulphate and hydroxyl groups (Löbmann & Svagan, 2017). The CNC in Figure 4.19 was characterised by ζ = –45.8 mV, compared to the CNF in Figure 4.18, characterised by ζ = –14.5 mV. Together with an increasing zeta potential, adsorption of CTAB onto the CNC surface was visually confirmed by SEM imaging

(Figure 4.19), whereby a previously reported (Fairman, 2014) morphological change was observed. The addition of CTAB to a tightly packed, non-porous CNC had some effect in the modified structure exhibiting a visually "fluffier" assembly (Fairman, 2014).

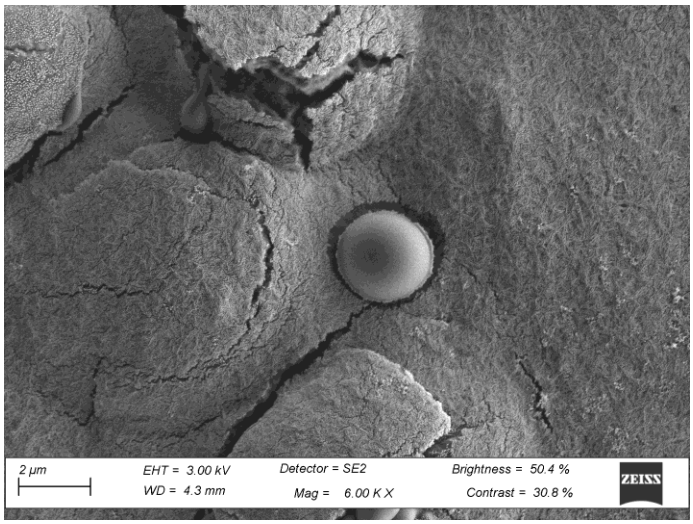

Figure 4.19: SEM micrograph of redispersed, previously freeze-dried cellulose nanocrystals (CNC) modified with surfactant (CTAB) (scale bar 2 µm)

The addition of CTAB resulted in a rougher surface (Xhanari et al., 2011), compared to the fine, uniform packing of CNC in thin layers as seen in Figure 4.19; adding that CTAB may reduce fibre-fibre bonding during the drying stages of sample preparation (Fairman, 2014). However, the addition of CTAB to CNC induces aggregation and sedimentation within a suspension (Tardy et al., 2017), due to interaction between the alkyl chain tails. This was visualised in the brightfield images in Figure 4.16, where CNC-CTAB aggregated and entrapped large, undissolved quercetin rods.

In order for a drug to be effective *in vivo*, it needs to be present as individual molecules dispersed throughout a liquid solvent. *Dissolution* requires the drug in its solid form to overcome intermolecular forces, separate and mix with the solvent (Williams et al., 2018). At the same time, if a molecule collides with the surface of an undissolved particle, it may adhere and undergo *crystallisation.* Both processes occur according to the dynamic equilibrium in Equation 4.6, as long as excess solute is present (Sun et al., 2012).

$$solute + solvent \underset{crystallization}{\overset{dissolution}{\rightleftharpoons}} solution \qquad [4.6]$$

A solution containing the maximum amount of solute that can dissolve at a given temperature and pressure is considered saturated (at its solubility limit), and if excess solute is present, the rate of dissolution equals the rate of crystallisation. Supersaturated solutions are unstable, as they contain more dissolved solute than allowed under particular conditions, and addition of a seed crystal causes the excess to precipitate. Quercetin is a naturally crystalline material, having a polymorphous structure made up by a regular and repeating arrangement of molecules expanding in three directions (Rossi, Rickles & Halpin, 1986), as illustrated in Figure 4.20 (Williams et al., 2018).

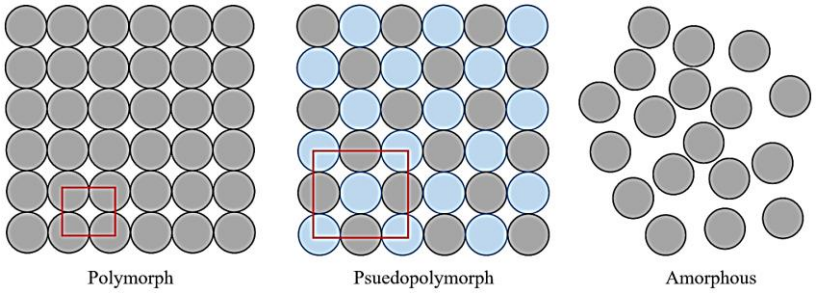

Figure 4.20: Graphical illustration depicting the polymorphic, pseudopolymorphic and amorphous forms of a crystalline drug, with the unit cell indicated by a red square, redrawn from Williams et al. (2018)

Quercetin hydrate is a psuedopolymorph, with a water molecule present in each unit cell. The strong intermolecular forces between the molecules in a polymorph serve as an energy barrier to dissolution; however, the more desirable amorphous form is thermodynamically unstable, and over time relaxes into a crystalline arrangement (Williams et al., 2018). Mixing drugs with polymers is a popular approach to stabilising the amorphous state (Figure 4.21), partly by sterically hindering the translational movement and reorientation of the drug into the crystalline phase (Löbmann & Svagan, 2017).

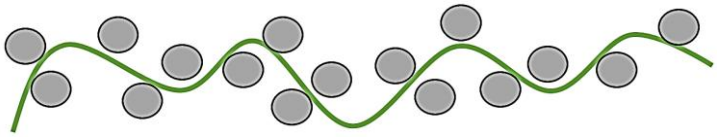

Figure 4.21: Graphical illustration depicting the mechanism by which polymeric nanofibres block the movement of drug molecules and stabilise the amorphous state, redrawn from Williams et al. (2018)

As shown in Figure 4.22, pre-homogenisation of quercetin resulted in reasonable delamination of the larger particles, as well as the introduction of smaller, more spherically shaped particles. This size reduction subsequently leads to an increased surface-to-volume ratio, and should result in an increased saturation solubility (Sun et al., 2012).

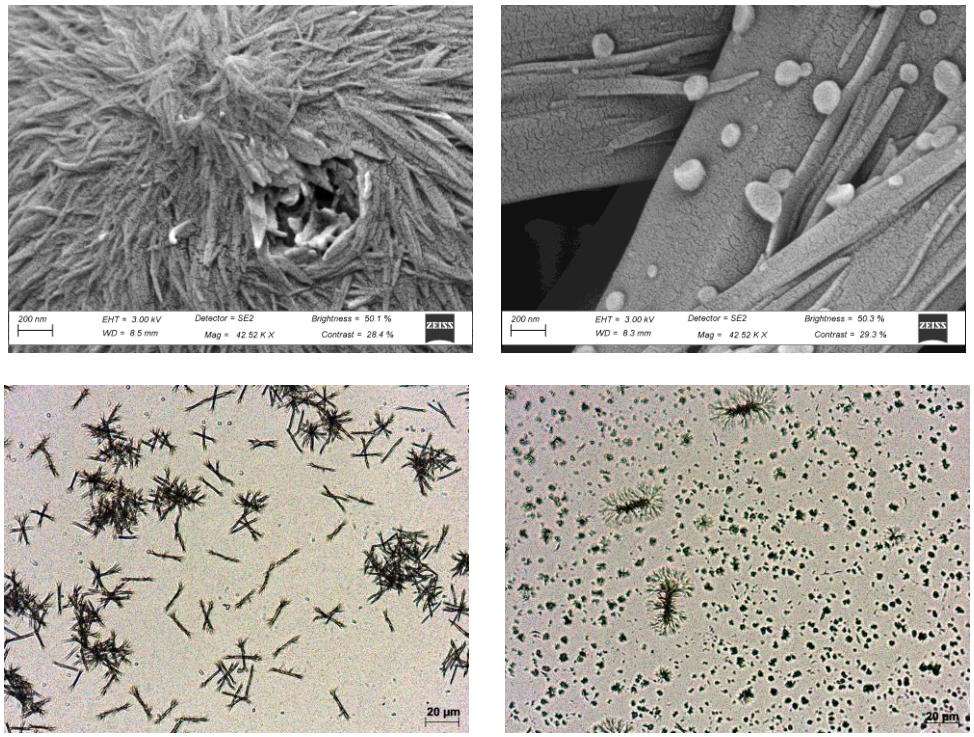

Figure 4.22: SEM (top, scale bar 200 nm) and brightfield (bottom, scale bar 20 µm) micrographs of unmodified (left) and homogenised (right) quercetin, solubilised at a concentration of 5.5 mg/mL in 75 wt% ethanol

However, despite homogenisation and 0.45 µm filtering of the initial quercetin solution, micron-sized (up to 20 µm) crystalline agglomerates of quercetin were still present in the CNC- and CNF-CTAB-QT formulations (visible in the SEM images in Figure 4.23). Thus, CNC and CNF were unsuccessful at maintaining quercetin in this high energy, metastable state. The large, elongated rods clustered together, forming a backbone for the respective CNC and CNF networks to weave between. It is hypothesised that a reversal of the dynamic dissolution-crystallisation equilibrium occurred and precipitation of excess solute was accelerated by collision during centrifugation, washing and drying.

Moreover, after particle size reduction and increased solubility, Ostwald ripening is more likely to occur, i.e. the process whereby large crystals grow at the expense of smaller crystals, due to their differences in solubility (Sun et al., 2012). In order to reduce the enlarged surface area as a result of decreased dimensions, there is a tendency towards precipitation, and subsequent agglomeration – the smaller the size, the faster the ripening.

The morphology of these precipitates corresponded well to typically observed needle-like quercetin obtained upon crystallisation from an organic solvents, such as

methanol, chloroform or acetone (Pal & Saha, 2017). It was similarly observed that CNF films mixed with an ethanol solution of the lipophilic drug indomethacin, resulted in a portion of the drug amorphously adsorbing to the fibres, and the remaining precipitating as nanocrystals (100 nm wide and 100–5 000 nm long) (Löbmann & Svagan, 2017).

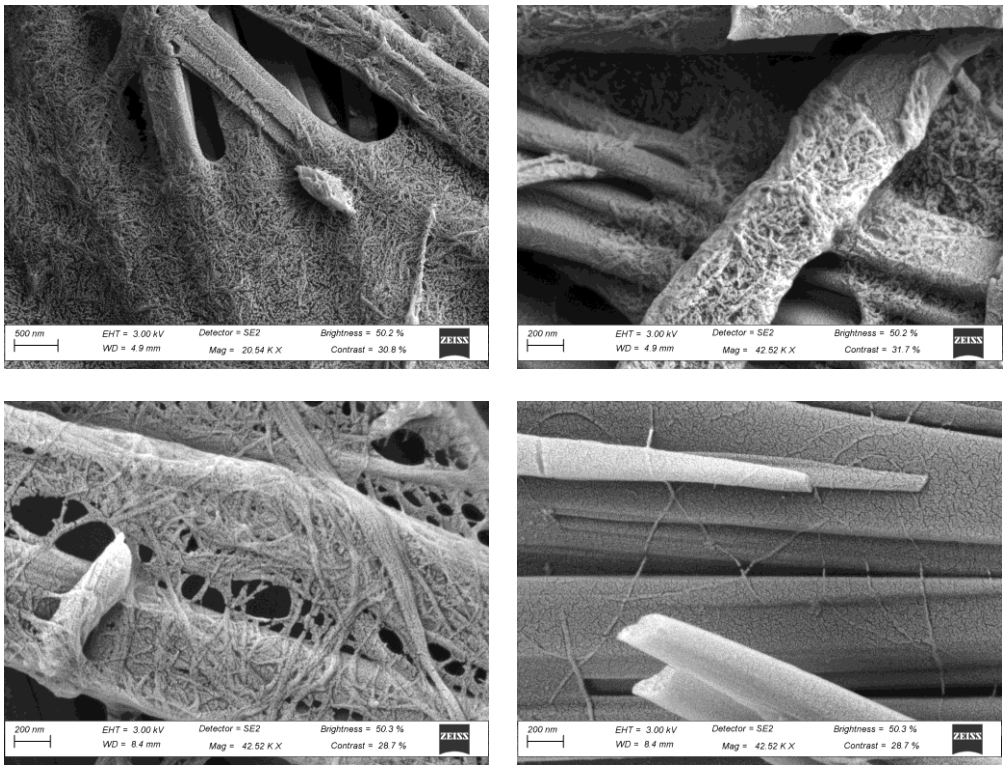

Figure 4.23: SEM micrographs of cellulose nanocrystals (CNC) (top) and cellulose nanofibrils (CNF) (bottom), modified with a surfactant (CTAB) and quercetin (QT) concentration of 4 mM and 5.5 mg/mL, respectively

The CNC network possessed smaller, individual crystalline particles densely packed together, covering more surface area than the CNF network, which comprised of long, smooth, entangled fibrous chains; both morphologies have been previously observed (Eichhorn et al., 2010; Fairman, 2014, Tardy et al., 2017). The CNC particles were uniform, with low aspect ratios and dimensions estimated in the range of 50–500 nm. The fibre bundles in the CNF network varied considerably, with estimated diameters in the range between 10–200 nm, and lengths up to several micron. Moreover, the more porous, “open” appearance of the CNF formulation is attributed to weaker aggregation experienced as a result of physical entanglement and flexibility, compared to stronger aggregation in the CNC formulations, governed by chemical interactions and hydrogen bonding between the more active surface groups (Li et al., 2015; Löbmann & Svagan, 2017).

4.3 Quercetin release kinetics from modified nanocellulose

Characterisation of the *in vitro* drug release profile of a NP formulation requires separation of the NP from the unbound drug (Wallace et al., 2019). This has been achieved by a number of methods, including ultracentrifugation, low-pressure filtration (Soppimath et al., 2001; Shen & Burgess, 2013), and dialysis methods (Yu et al., 2019). The final formulation of CNC-CTAB-QT (Figure 4.24), prepared using freeze dried CNC and homogenised, filtered (< 0.45 µm) quercetin at centre-point conditions (4 mM CTAB, 5.5 mg/mL QT), was used for a trial release test, employing the dialysis bag method (Li et al., 2009; Kumar et al., 2015; Selvaraj et al., 2021).

Sink conditions of 70 wt% ethanol were maintained at 37 ºC and 120 rpm, and a dialysis membrane with a MWCO of 14 kDa (Li et al., 2019) was used. A control run was performed for an equivalent amount of free quercetin, in order to compare the determined release rate and mechanism of the DDS to the release of the free drug. Experiments were performed in triplicate, and the mean cumulative release profiles were regressed according to the zero-order, first-order, Higuchi and Korsmeyer-Peppas models (Equations 2.1 – 2.4), where linearisation into the form $y = mx + b$ was first applied where necessary.

4.3.1 Modelling release kinetics

Polymeric NPs are modelled as either a matrix or reservoir system (illustrated simply in Figure 4.24), where the release rate depends on the nature of the developed DDS, and is assumed to be controlled by diffusion through the polymeric membrane or matrix, possibly aided by its dissolution or erosion (Soppimath et al., 2001; Shaikh et al., 2015).

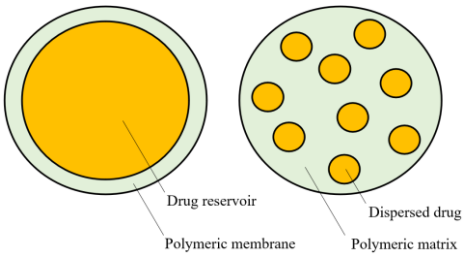

Figure 4.24: Simple schematic of reservoir (left) and matrix (right) nanoparticle (NP) systems, redrawn from Williams et al. (2018)

Matrix systems (e.g. nanospheres), assume a uniform drug distribution and release via diffusion and erosion (modelled as first-order), whereas reservoir systems (e.g. nanocapsules), assume complete drug encapsulation by the polymer, and release via diffusion across the barrier layer (modelled as zero-order) (Williams et al., 2018).

The calculated release data is given in Table D.1 in Appendix D. Cumulative release exceeded 100%, hypothesised as a result of the unstable dissolution/crystallisation equilibrium leading to discrepancies in solubility and error in the DLS results, propagating through to quantification of cumulative quercetin released. The calibration curve was repeated (Figure D.1), and the erroneous data removed as outliers,. Generally, the Korsmeyer-Peppas model should only be used to fit the first 60% of the release data (Korsmeyer et al., 1983), however due to the lack of available data points, this assumption was neglected. The linearised release data and fitted trendlines for each mechanistic model are provided in Figure 4.25, with coefficients of determination summarised in Table 4.10.

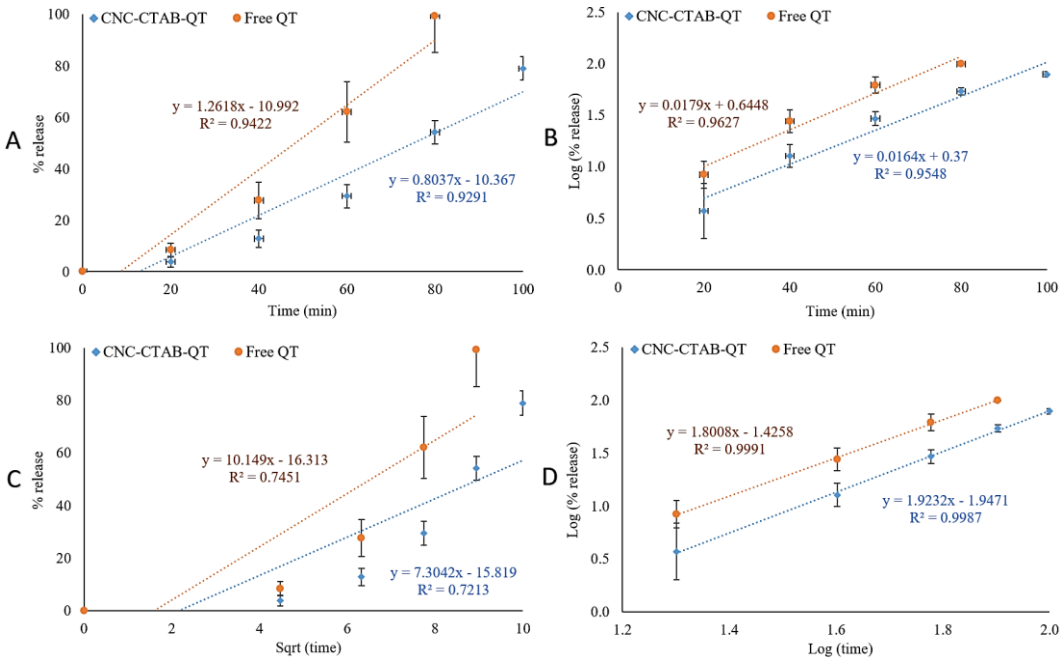

Figure 4.25: Cumulative percent release vs time data from dialysis bag tests of cellulose nanocrystals (CNC) modified with 4 mM surfactant (CTAB) and 5.5 mg/mL quercetin (QT), as well as an equivalent amount of free QT as a control run, fitted to (a) zero-order, (b) first-order, (c) Higuchi, and (d) Korsmeyer-Peppas models

Table 4.10: Coefficients of determination of mechanistic models fitted to the release profiles of cellulose nanocrystals (CNC), modified with 4 mM surfactant (CTAB) and 5.5 mg/mL quercetin (QT), as well as a control run of equivalent free QT

Model	R^2 (%)	
	CNC-CTAB-QT	Free QT
Zero-order	92.9	94.2
First-order	95.5	96.3
Korsmeyer-Peppas	99.9	99.9
Higuchi	72.1	74.5

It is clear by the high coefficient of determination (R^2 = 99.9%), that the Korsmeyer-Peppas model was the best at fitting the release profiles of both the CNC-CTAB-QT formulation and the free drug. The release exponent *n*, given by the trendline gradient, characterises the mechanism of release according to Table 2.2. In both cases, $n > 1$ suggested that the release was best modelled as non-Fickian diffusion, specifically super case II transport, which describes the influence of polymeric hydration and swelling on drug release for swellable systems, related to matrix erosion and disentanglement for non-swellable systems (Camelo et al., 2016). Therefore the DDS is best described as an interwoven nanofibre matrix, with drug release as both diffusion- and erosion-controlled.

The steeper gradients and release rate constant of $K = 9\ min^{-1}$ calculated for the free drug, confirms that formulating quercetin to be transported as a CNC-CTAB-QT formulation did have some effect on slowing the release of the drug into the sink, as is evident by the flatter gradients and calculated release rate constant of $K = 8\ min^{-1}$ for the DDS. Within the first hour, the free drug has displayed a 62.0% cumulative release, while at the same time point the formulated DDS had released less than half of this amount (29.4%). However, a rapid rather than controlled or sustained release was achieved.

Raghav et al. (2021) have compiled a comprehensive review on recent nanoscale DDSs, reporting varying release times between a few minutes to several days in literature. For example, Selvaraj et al. (2021) prepared quercetin-loaded alginate NPs via cold precipitation, that upon dialysis showed sustained release for up to six days, attributed to degradation of the polymer matrix. Moreover, *in vitro* studies reported these quercetin-alginate NPs to retain their anti-oxidant activity, as well as show enhanced anti-cancer efficacy of the U937 cell line (Selvaraj et al., 2021).

On the other hand, CNF films loaded with the water-insoluble drug indomethacin, showed complete release within 10–20 minutes; the immediate and burst release profile was attributed to the presence of the drug in both its amorphous and crystalline state (Löbmann & Svagan, 2017). A typical limitation of polymeric systems is their tendency to demonstrate *in vitro* instability and a rapid initial release compared to inorganic systems (Akhter et al., 2013), representing the fraction of drug weakly associated with the NP. Li et al. (2019) reported a cumulative release of 38% in eight hours for prepared CNF-QT, compared to the equivalent free drug release of 57%; however, undissolved blocks of quercetin appeared in the system at 50 wt% ethanol, imparting uncertainty in the results.

CNC-CTAB formulations prepared and loaded with curcumin (Raghav et al., 2020) and various NSAIDs (Gupta & Raghav, 2020), displayed release profiles effects for 18 hours and 3 hours, respectively, with release rate proportional to binding efficiency of the drug (Gupta & Raghav, 2020; Raghav et al., 2020). Biphasic models are frequently reported for polymeric DDSs (Li et al., 2009; Dinesh Kumar Verma & Singh, 2015), with initial burst release of the unbound drug, followed by diffusion of the dispersed drug, with potential dissolution/erosion of the polymeric matrix.

4.3.2 Limitations of the dialysis bag method

The dialysis bag method is commonly used for dissolution releases tests, and in practice, permeation of the drug across the membrane is generally considered rapid (in other words, not rate limiting) (Yu et al., 2019). However, in reality, the apparent release profile of the drug in the sink compartment is often delayed due to unaccounted for diffusion of the drug through the membrane.

This effect is more prominent for membranes with low permeability coefficients, whereby the barrier effects not only delay the apparent drug release rate, but also hinder the actual drug release. In some cases, incomplete drug release from nanocarriers may occur due to over-saturation of the release medium, leading to a change in the release mechanism after the initial phase of release (Zhou et al., 2016).

The assumption of effective sink conditions is based on the large volume of release medium in the receiver compartment being around 10–20 times higher than the volume required for saturation (allowing for rapid equilibration across the membrane and maintenance of a low free drug concentration in the donor compartment (Yu et a., 2019). Moreover, reversible binding of the release drug to the nanocarrier is possible, and may reduce the driving force for drug transport across the membrane, resulting in a slower overall apparent release rate (Modi & Anderson, 2013).

Thus, in order to calculate the actual release profile of the drug adjacent to the nanocarriers, calibration experiments of the membrane barrier properties need to be performed, and an appropriate mathematical model should be applied to the sampled experimental data (Weng Tong & Chow, 2020), such as numerical deconvolution (Zhou et al., 2016) or dynamic simulations (Modi & Anderson, 2013).

4.4 *In vivo* safety profile in zebrafish

Unfortunately, the CNC-CTAB-QT formulation was too large to administer to the zebrafish larvae for sufficient toxicity, efficacy, biodistribution and functional response testing. Figure 4.26 below shows a micrograph of a larval zebrafish tail taken during the pilot *in vivo* performance test, showing that even after dilution, the elongated and aggregated quercetin crystals, entangled in the fibrous NC network, gravitated towards the body of the fish, leading to an increase in viscosity of the incubation medium, and subsequent suffocation of the zebrafish.

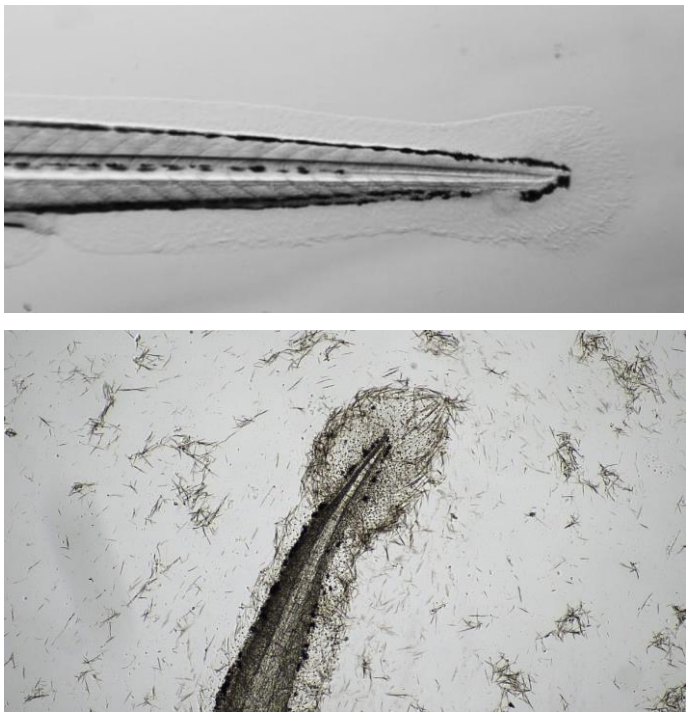

Figure 4.26: Brightfield micrographs (100X) of a larval zebrafish tail, before (top) and after (bottom) incubation with cellulose nanocrystals (CNC) modified with surfactant (CTAB) and quercetin (QT), taken during an *in vivo* toxicity assay

Moreover, in some instances, synthetic surfactants (such as CTAB) have been reported as being toxic to cells, by inducing cell membrane lysis (Lunardi et al., 2021). Naturally available surfactants have been studied as alternatives to modifying NC for hydrophobic interaction. However, NC modified with the natural surfactant *rarasaponin* exhibited lower adsorption capabilities than NC modified with synthetic surfactants, such as CTAB, SDS and Tween20 (Bundjaja et al., 2020).

Chapter 5: Conclusions and recommendations

The purpose of this study was to investigate CNC and CNF as potential carriers for quercetin, through modification with CTAB. The surfactant facilitated effective drug binding by rendering the NC surface hydrophobic. The DDSs were able to bind and release quercetin at a slower rate than the release of the free drug, suiting their functionality as delivery systems. RSM was useful in understanding the interaction between surfactant and drug concentration, and their effect on particle size, charge, dispersity and binding efficiency. The particle morphologies consisted of aggregated fibrillar networks, with large, precipitated quercetin crystals. Further work is necessary to improve the size distribution, quercetin amorphisation and stability of the DDS, to enable sufficient testing on *in vivo* models, such as zebrafish. Optimisation and validation by other methods should be performed to obtain models that more accurately describe the system.

5.1 General conclusions

The main conclusions are discussed according to the objectives in Chapter 1:

(i) Investigate the effect of surfactant and drug concentration on particle morphology and drug binding efficiency

The particle sizes were largely overestimated due to DLS reporting a mean hydrodynamic diameter for poorly-defined aggregates. The average PdI of 0.69 suggested broad size distributions, not considered ideal for drug delivery. Limitations of DLS for non-spherical systems with low aqueous solubility led to failure of the Z and PdI models. However, the ζ and BE models reported high R^2 values with low cross validation errors, indicative of good fits. Both polymers reported a mean binding efficiency of 77%, indicating a high drug loading capacity. CNF reported a less negative mean zeta potential (– 9.9 mV) than CNC (– 17.5 mV), however, both fall below 30 mV, indicating colloidally unstable systems prone to aggregation. The curvilinear response of charge and binding efficiency to increasing surfactant concentration is explained by micelle formation at the NC surface and surfactant-drug interaction. The interaction between NC and CTAB is electrostatic, while the interaction between CTAB and quercetin is hydrophobic. At low surfactant concentrations, the anionic charges are reduced and hydrophobicity increases, facilitating efficient drug binding. However, at high surfactant concentrations, reassociation of the surfactant monomers into micelles that can detach from the surface leads to an increase in the anionic charge, decreasing hydrophobicity and drug binding.

(ii) Modify and characterise nanocellulose for the binding and release of quercetin

The smaller, more uniform size of CNC may lend itself well to liquid suspensions and oral formulations, whereas the fibrous network of CNF may be better suited for hydrogels, films or transdermal patches. The rheological complexities and inter-fibrillar aggregation of NC upon drying pose challenges to its suitability as a drug carrier. In CNF, aggregation was governed by the physical entanglement of flexible fibres, whereas in CNC, aggregation was governed by chemical interaction and hydrogen bonding. Size reduction via homogenisation was ineffective, and had little influence on the "bird nest" structure. However, homogenisation led to considerable delamination of the larger fibre bundles. Homogenisation and filtering of quercetin resulted in reasonable size reduction, but its amorphous form proved to be thermodynamically unstable in CNC and CNF, recrystallizing into large rod-shaped particles within the NC networks.

(iii) Investigate and model quercetin release kinetics from nanocellulose

The release profile of the CNC-CTAB-QT formulation was best fitted by the Korsmeyer-Peppas model (R^2 = 99.9%), with a release exponent $n > 1$ indicating super case II transport. This suggests that drug release occurred via diffusion, as well as erosion of the polymeric matrix. Although the DDS delayed drug release (29% released within 60 minutes, compared to 62% released by the free drug), visually, the release followed a zero-order rather than sustained release, with complete release within 100 minutes. Therefore the formulated DDS was ineffective for the slow, controlled release of quercetin.

(iv) Evaluate the in vivo toxicity using the zebrafish model

Sufficient toxicity and functional response tests of the CNC-CTAB-QT formulations were unable to be performed on the zebrafish. Even after dilution, large quercetin crystals precipitated in the fibrous NC networks, gravitating towards the body of the fish, increasing the viscosity of the incubation medium and suffocating the fish.

5.2 Recommendations and future work

While this study represents notable progress towards the application of NC in drug delivery, the following proposals and recommendations are made for future work:

Aggregation, size reduction and drug solubilisation

Although the relationship between NC and water still eludes the scientific community, NC shows a high affinity for aggregation in solvents other than water.

However, upon modification with CTAB, an organic solvent should rather be used to redisperse the hydrophobic NC, in which CTAB can prevent excessive aggregation between particles by steric stabilisation. In terms of quercetin solubilisation, DMSO could be explored as an alternative organic solvent in which quercetin is highly soluble, however, this may have toxic side effects. Homogenisation could be improved by using a high-pressure rather than high-shear homogeniser, known to improve NP yield and efficacy. Moreover, spray-drying as an alternative to freeze-drying has been found to significantly reduce agglomeration. The effect of solids concentration and incubation temperature could be investigated, as hydrophobic interaction increases with temperature.

Cellulose source and characterisation

Although there is extensive research covering the effects of NC surface charges on its interaction with surfactants, there is a paucity of studies addressing the influence of the aspect ratio, source and isolation process of the material. In order to effectively compare NC in its crystalline and fibril form, the two types of NC should ideally be extracted from the same cellulose source, as CNC can be isolated from CNF by removing the amorphous regions in the polymer chains. Additional characterisation of the materials, such as FT-IR, XRD, TEM, and AFM could be performed to expand the investigated response variables. For further insight into the aggregate structure and extent of charge reversal, zeta potential of the intermediate NC-CTAB systems should be measured prior to loading quercetin.

Experimental design

The experimental design could be further improved by first systematically identifying all dominant variables by a OFAT approach, followed by an initial screening phase of factors through a fractional factorial design, e.g. surfactant, drug, and polymer concentration, ethanol wt%, temperature, pH, homogenisation and centrifugation time/speed. Surface area and textural properties, such as porosity, should be characterised to investigate their effect on quercetin binding. Modelling of the significant factors should ideally be achieved through a rotatable (alpha = 1.14) CCD, with extreme high and low star points and equal prediction variance at all points equidistant from the centre. The method of steepest ascent should be used to locate the area of optimality, and optimisation should be repeated after model improvement and validated by other parametric methods. An increase in sample size could improve the normality of the raw data distributions, otherwise Box-Cox transformations or non-parametric statistical tests should replace ANOVA.

In vitro and *in vivo* testing

In future work, in order to obtain the true release profile of the drug, calibration of the dialysis membrane properties should be used together with an appropriate mathematical model. Alternatively, other methods of separating the unencapsulated drug from its nanocarrier can be employed, such as ultracentrifugation, or low-pressure filtration.

Testing the effect of pH and temperature, as well as sink conditions (e.g. simulated gastric or intestinal fluid), could provide additional insight into the release mechanism of the formulated DDSs. Moreover, NP systems of such morphologies are not suitable for incubation and absorption with zebrafish, but could rather be administered orally from 72 hpf onwards, once the fish are able to swallow. The bioactivity of quercetin could be assessed through anti-oxidant, cathepsins inhibiting and serum protein binding tests.

Commercialisation

Although recent years have shown great advances in NC-based medicine, determination of size distributions remains a challenge, and has resulted in discrepancies among products and suppliers. This has greatly hindered the adoption of this revolutionary material in the marketplace. Interdisciplinary research conducted in collaboration with manufacturers, together with extensive technoeconomic and life cycle analyses, is needed to facilitate scientifically sound and commercially viable solutions. *"The future is bright, but it will require hard and careful work to manifest the many benefits nature has bestowed on us in that most enigmatic of natural polymers, cellulose."* – Moon et al. (2016).

Reference List

Abitbol, T., Marway, H. & Cranston, E.D. 2014. Surface modification of cellulose nanocrystals with cetyltrimethylammonium bromide. Nordic Pulp & Paper Research Journal. 29:46–57.

Absolom, D.R. 1986. Opsonins and Dysopsonins: An Overview. In Methods in Enzymology. V. 132. 281–318.

Adepu, S. & Ramakrishna, S. 2021. Controlled drug delivery systems: Current status and future directions. Molecules. 26:1–48.

Akhter, S., Ahmad, I., Ahmad, M.Z., Ramazani, F., Singh, A., Rahman, Z., Jalees Ahmad, F., Storm, G., et al. 2013. Nanomedicines as Cancer Therapeutics: Current Status. Current Cancer Drug Targets. 13:1–17.

Alila, S., Boufi, S., Belgacem, M.N. & Beneventi, D. 2005. Adsorption of a cationic surfactant onto cellulosic fibers I. Surface charge effects. Langmuir. 21:8106–8113.

Almazroo, O.A., Miah, M.K. & Venkataramanan, R. 2017. Drug Metabolism in the Liver. Clinics in Liver Disease. 21:1–20.

Arai, K., Horikawa, Y. & Shikata, T. 2018. Transport Properties of Commercial Cellulose Nanocrystals in Aqueous Suspension Prepared from Chemical Pulp via Sulfuric Acid Hydrolysis. ACS Omega. 3:13944–13951.

Aschenbrenner, E., Bley, K., Koynov, K., Makowski, M., Kappl, M., Landfester, K. & Weiss, C.K. 2013. Using the polymeric ouzo effect for the preparation of polysaccharide-based nanoparticles. Langmuir. 29:8845–8855.

Bester, L.M. 2018. Development and optimisation of a process for cellulose nanoparticle production from waste paper sludge with enzymatic hydrolysis as an integral part. Master's Thesis. University of Stellenbosch.

Bhattacharjee, S. 2016. DLS and zeta potential - What they are and what they are not? Journal of Controlled Release. 235:337–351.

Bhutiya, P.L., Misra, N., Rasheed, M.A. & Hasan, S.Z. 2020. Silver Nanoparticles Deposited Algal Nanofibrous Cellulose Sheet for Antibacterial Activity. BioNanoScience. 10:23–33.

Boddy, A. & Aarons, L. 1989. Pharmacokinetic and pharmacodynamic aspects of site-specific drug delivery. Advanced Drug Delivery Reviews. 3:155–163.

Bohnert, T. & Gan, L.-S. 2013. Plasma protein binding: From discovery to development. Journal of Pharmaceutical Sciences. 102:2953–2994.

Bohrey, S., Chourasiya, V. & Pandey, A. 2016. Polymeric nanoparticles containing diazepam: preparation, optimization, characterization, in-vitro drug release and release kinetic study. Nano Convergence. 3:3.

Box, G.E.P & Behken, D.W. 1960. Some New Three Level Designs for the Study of Quantitative Variables. Technometrics. 2:455–475.

Box, G.E.P. & Draper, N.R. 1987. Empirical model-building and response surfaces. Hoboken, NJ: John Wiley & Sons, Ltd.

Box, G.E.P & Wilson, K.B. 1951. On the Experimental Attainment of Optimum Conditions. Journal of the Royal Statistical Society Series B. 13:1–45.

Bruschi, M.L. Ed. 2015. Mathematical models of drug release. In Strategies to Modify the Drug Release from Pharmaceutical Systems. Elsevier Ltd. 63–86.

Bundjaja, V., Sari, T.M., Soetaredjo, F.E., Yuliana, M., Angkawijaya, A.E., Ismadji, S., Cheng, K.C. & Santoso, S.P. 2020. Aqueous sorption of tetracycline using rarasaponin-modified nanocrystalline cellulose. Journal of Molecular Liquids. 301:112433.

Caballero, M. v & Candiracci, M. 2018. Zebrafish as screening model for detecting toxicity and drugs efficacy. Journal of Unexplored Medical Data. 3:1–14.

Camelo, S.R.P., Franceschi, S., Perez, E., Fullana, S.G. & Ré, M.I. 2016. Factors influencing the erosion rate and the drug release kinetics from organogels designed as matrices for oral controlled release of a hydrophobic drug. Drug Development and Industrial Pharmacy. 42:985–997.

Canesi, L., Ciacci, C., Betti, M., Fabbri, R., Canonico, B., Fantinati, A., Marcomini, A. & Pojana, G. 2008. Immunotoxicity of carbon black nanoparticles to blue mussel hemocytes. Environment International. 34:1114–1119.

Caracciolo, G., Farokhzad, O.C. & Mahmoudi, M. 2017. Biological Identity of Nanoparticles In Vivo: Clinical Implications of the Protein Corona. Trends in Biotechnology. 35:257–264.

Carbone, C., Martins-Gomes, C., Pepe, V., Silva, A.M., Musumeci, T., Puglisi, G., Furneri, P.M. & Souto, E.B. 2018. Repurposing itraconazole to the benefit of skin cancer treatment: A combined azole-DDAB nanoencapsulation strategy. Colloids and Surfaces B: Biointerfaces. 167:337–344.

Chaaban, H., Ioannou, I., Chebil, L., Slimane, M., Gerardin, C., Paris, C., Charbonnel, C., Chekir, L., et al. 2017. Effect of heat processing on thermal stability and antioxidant activity of six flavonoids. Journal of Food Processing and Preservation. 41:13203.

Chen, Y.W., Lee, H.V., Abd Hamid, S.B. 2017. Investigation of optimal conditions for production of highly crystalline hydrolysis: response surface methodology. Carbohydrate Polymers. 178: 57–68.

Crespo, C.F., Badshah, M., Alvarez, M.T. & Mattiasson, B. 2012. Ethanol production by continuous fermentation of d-(+)-cellobiose, d-(+)-xylose and sugarcane bagasse hydrolysate using the thermoanaerobe Caloramator boliviensis. Bioresource Technology. 103:186–191.

Czyrski, A. 2019. Determination of the Lipophilicity of Ibuprofen, Naproxen, Ketoprofen, and Flurbiprofen with Thin-Layer Chromatography. Journal of Chemistry. 2019:1–6.

Danaei, M., Dehghankhold, M., Ataei, S., Hasanzadeh Davarani, F., Javanmard, R., Dokhani, A., Khorasani, S. & Mozafari, M.R. 2018. Impact of particle size and polydispersity index on the clinical applications of lipidic nanocarrier systems. Pharmaceutics. 10:1–17.

Das, S., Ghosh, B. & Sarkar, K. 2022. Nanocellulose as sustainable biomaterials for drug delivery. Sensors International. 3:100135.

Dash, S., Murthy, P.N., Nath, L. & Chowdhury, P. 2010. Kinetic modelling of drug release from controlled drug delivery systems. Acta Poloniae Pharmaceutica - Drug Research. 67:217–223.

Deepa, B., Abraham, E., Cordeiro, N., Mozetic, M., Mathew, A.P., Oksman, K., Faria, M., Thomas, S., et al. 2015. Utilization of various lignocellulosic biomass for the production of nanocellulose: a comparative study. Cellulose. 22:1075–1090.

Derringer, G. & Suich, R. 1980. Simultaneous Optimization of Several Response Variables. Journal of Quality Technology. 12:214–219.

Devore, J.L. 2016. Probability and Statistics for Engineering and the Sciences. Boston, MA: Cengage Learning ed.

Dinesh Kumar, V., Verma, P.R.P. & Singh, S.K. 2015. Development and evaluation of biodegradable polymeric nanoparticles for the effective delivery of quercetin using a quality by design approach. LWT - Food Science and Technology. 61:330–338.

Dong, S., Hirani, A.A., Kolacino, K.R., Lee, Y.W. & Roman, M. 2012. Cytotoxicity and cellular uptake of cellulose nanocrystals. Nano Life. 2:1241006

Doolaanea, A.A., Ismail, A.F.H., Mansor, N.I., Mohd Nor, N.H. & Mohamed, F. 2015. Effect of surfactants on plasmid DNA stability and release from poly (D,L-lactide-co-glycolide) microspheres. Tropical Journal of Pharmaceutical Research. 14:1769–1778.

Duan, Y., Coreas, R., Liu, Y., Bitounis, D., Zhang, Z., Parviz, D., Strano, M., Demokritou, P., et al. 2020. Prediction of protein corona on nanomaterials by machine learning using novel descriptors. NanoImpact. 17:100207.

Dufresne, A. 2013. Nanocellulose: A new ageless bionanomaterial. Materials Today. 16:220–227.

Dwiarti, L., Boonchird, C., Harashima, S. & Park, E.Y. 2012. Simultaneous saccharification and fermentation of paper sludge without pretreatment using cellulase from Acremonium cellulolyticus and thermotolerant Saccharomyces cerevisiae. Biomass and Bioenergy. 42:114–122.

Eichhorn, S.J., Dufresne, A.A., Aranguren, A.M., Marcovich, A.N.E., Capadona, A.J.R., Rowan, A.S.J., Weder, A.C., Thielemans, A.W., et al. 2010. Review: current international research into cellulose nanofibres and nanocomposites. Journal of Materials Science. 45:1–33.

Elisseef, J. 2008. Structure starts to gel. Nature Materials. 7:271–273.

Endes, C., Camarero-Espinosa, S., Mueller, S., Foster, E.J., Petri-Fink, A., Rothen-Rutishauser, B., Weder, C. & Clift, M.J.D. 2016. A critical review of the current knowledge regarding the biological impact of nanocellulose. Journal of Nanobiotechnology. 14:1–14.

Fairman, E. 2014. Avoiding Aggregation During Drying and Rehydration of Nanocellulose. Honors College. Available: https://digitalcommons.library.umaine.edu/honors/172. [Accessed July 2022]

Furtado, M.R., da Matta, V.M., Carvalho, C.W.P., Magalhães, W.L.E., Rossi, A.L. & Tonon, R. v. 2021. Characterization of spray-dried nanofibrillated cellulose and effect of different homogenization methods on the stability and rheological properties of the reconstituted suspension. Cellulose. 28:207–221.

Gao, L., Liu, G., Wang, X., Liu, F., Xu, Y. & Ma, J. 2011. Preparation of a chemically stable quercetin formulation using nanosuspension technology. International Journal of Pharmaceutics. 404:231–237.

Gao, Z., Zhang, L. & Sun, Y. 2012. Nanotechnology applied to overcome tumor drug resistance. Journal of Controlled Release. 162:45–55.

Garcia, R.B., Nagashima, T., Praxedes, A.K.C., Raffin, F.N., Moura, T.F.A.L., Sócrates, E. & do Egito, T. 2001. Preparation of micro and nanoparticles from corn cobs xylan. Polymer Bulletin. 46:371–379.

Geng, Y., Dalhaimer, P., Cai, S., et al. 2007. Shape effects of filaments versus spherical particles in flow and drug delivery. Nature Nanotechnology. 2:1283–1300.

Gericke, M., Schulze, P. & Heinze, T. 2020. Nanoparticles Based on Hydrophobic Polysaccharide Derivatives—Formation Principles, Characterization Techniques, and Biomedical Applications. Macromolecular Bioscience. 20:1–39.

González-García, L.E., Macgregor, M.N., Visalakshan, R.M., Lazarian, A., Cavallaro, A.A., Morsbach, S., Mierczynska-Vasilev, A., Mailänder, V., et al. 2022. Nanoparticles Surface Chemistry Influence on Protein Corona Composition and Inflammatory Responses. Nanomaterials. 12:682.

Grunwald, D.J. & Eisen, J.S. 2002. Headwater of the zebrafish - emergence of a new model vertebrate. Nature Reviews Genetics. 3:717–724.

Gugler, R., Leschik, M. & Dengler, H.J. 1975. Disposition of quercetin in man after single oral and intravenous doses. European Journal of Clinical Pharmacology. 9:229–234

Gupta, A.K. & Gupta, M. 2005. Synthesis and surface engineering of iron oxide nanoparticles for biomedical applications. Biomaterials. 26:3995–4021.

Gupta, B.P., Thakur, N., Jain, N.P., Banweer, J. & Jain, S. 2010. Osmotically controlled drug delivery system with associated drugs. Journal of Pharmaceutical Sciences. 13:571–588.

Gupta, R.D. & Raghav, N. 2020. Nano-crystalline cellulose: Preparation, modification and usage as sustained release drug delivery excipient for some non-steroidal anti-inflammatory drugs. International Journal of Biological Macromolecules. 147:921– 930.

Haaland, P.D. (1989) Statistical Problem Solving. In: Haaland, P.D., Ed., Experimental Design in Biotechnology, Marcel Dekker, New York, 1-18.

Habibi, Y., Lucia, L.A. & Rojas, O.J. 2010. Cellulose nanocrystals: Chemistry, self-assembly, and applications. Chemical Reviews. 110:3479–3500.

Han, J., Zhou, C., Wu, Y., Liu, F. & Wu, Q. 2013. Self-Assembling Behavior of Cellulose Nanoparticles during Freeze-Drying: Effect of Suspension Concentration, Particle Size, Crystal Structure, and Surface Charge. Biomacromolecules. 14:1529–1540.

Harper, B.J., Clendaniel, A., Sinche, F., Way, D., Hughes, M., Schardt, J., Simonsen, J., Stefaniak, A.B., et al. 2016. Impacts of chemical modification on the toxicity of diverse nanocellulose materials to developing zebrafish. Cellulose. 23:1763–1775.

Hasan, N., Rahman, L., Kim, S.H., Cao, J., Arjuna, A., Lallo, S., Jhun, B.H. & Yoo, J.W. 2020. Recent advances of nanocellulose in drug delivery systems. Journal of Pharmaceutical Investigation. 50:553–572.

Haque, E. & Ward, A.C. 2018. Zebrafish as a Model to Evaluate Nanoparticle Toxicity. Nanomaterials. 8:561.

He, Y., He, Z., He, F. & Wan, H. 2012. Determination of quercetin, plumbagin and total flavonoids in Drosera peltata Smith var. glabrata Y .Z.Ruan. Pharmacognosy Magazine. 8:263–267.

Hein, C.D., Liu, X.M. & Wang, D. 2008. Click chemistry, a powerful tool for pharmaceutical sciences. Pharmaceutical Research. 25:2216–2230.

Higuchi, T. 1963. Mechanism of Sustained-Action Medication. Theoretical analysis of rate of release of solid drugs dispersed in solid matrices. Journal of Pharmaceutical Sciences. 52:1145–1149.

Hollman, P.C.H. & Katan, M.B. 1999. Dietary Flavonoids: Intake, Health Effects and Bioavailability. Food and Chemical Toxicology. 37:937–942.

Hoo, C.M., Starostin, N., West, P. & Mecartney, M.L. 2008. A comparison of atomic force microscopy (AFM) and dynamic light scattering (DLS) methods to characterize nanoparticle size distributions. Journal of Nanoparticle Research. 10:89–96.

Howe, K., Clark, M.D., Torroja, C.F., Torrance, J., Berthelot, C., Muffato, M., Collins, J.E., Humphray, S., et al. 2013. The zebrafish reference genome sequence and its relationship to the human genome. Nature. 496:498–503.

Hubbe, M.A. 2007. Flocculation and redispersion of cellulosic fiber suspensions: a review of effects of hydrodynamic shear and polyelectrolytes. Bioresources. 2:296–331.

Hubbe, M.A., Rojas, O.J. & Lucia, L.A. 2015. Green modification of surface characteristics of cellulosic materials at the molecular or nano scale: A review. BioResources. 10:6095-6206.

International Standards Organization. 2017. ISO 22412:2017 - Particle size analysis - Dynamic light scattering (DLS). Available: https://www.iso.org/standard/65410.html [Accessed November 2021].

Jackson, J.K., Letchford, K., Wasserman, B.Z., Ye, L., Hamad, W.Y. & Burt, H.M. 2011. The use of nanocrystalline cellulose for the binding and controlled release of drugs. International Journal of Nanomedicine. 6:321–330.

Jagur-Grodzinski, J. 2010. Polymeric gels and hydrogels for biomedical and pharmaceutical applications. Polymers for Advanced Technologies. 21:27–47.

Jiang, F. & Hsieh, Y. lo. 2013. Chemically and mechanically isolated nanocellulose and their self-assembled structures. Carbohydrate Polymers. 95:32–40.

de Jong, W.H. & Borm, P.J. 2008. Drug delivery and nanoparticles: Applications and hazards. International Journal of Nanomedicine. 3:133–149.

Kamaly, N., Yameen, B., Wu, J. & Farokhzad, O.C. 2016. Degradable Controlled-Release Polymers and Polymeric Nanoparticles: Mechanisms of Controlling Drug Release. Chemical Reviews. 116:2602–2663.

Kane, A.S., Salierno, J.D. & Brewer, S.K. 2005. Fish models in behavioral toxicology: Automated techniques, updates and perspectives. In Methods in Aquatic Toxicology. V. 2. G.K. Ostrander, Ed. Boca Raton, FL: Lewis Publishers. 559–590.

Kar, B. & Subbiah, S. 2013. Zebrafish: An in vivo model for the study of human diseases. International Journal of Genetics and Genomics. 1:6–11.

Karadag, A., Ozcelik, B. & Huang, Q. 2014. Quercetin nanosuspensions produced by high-pressure homogenization. Journal of Agricultural and Food Chemistry. 62:1852–1859.

Karmakar, S. 2019. Particle Size Distribution and Zeta Potential Based on Dynamic Light Scattering: Techniques to Characterize Stability and Surface Charge Distribution of Charged Colloids. In Recent Trends in Materials: Physics and Chemistry. 117–159.

Khaled, K.A., El-Sayed, Y.M. & Al-Hadiya, B.M. 2003. Disposition of the flavonoid quercetin in rats after single intravenous and oral doses. Drug Development and Industrial Pharmacy. 29:397–403.

Khine, Y.Y. & Stenzel, M.H. 2020. Surface modified cellulose nanomaterials: A source of non-spherical nanoparticles for drug delivery. Materials Horizons. 7:1727–1758.

Khursheed, R., Singh, S.K., Wadhwa, S., Gulati, M. & Awasthi, A. 2020. Enhancing the potential preclinical and clinical benefits of quercetin through novel drug delivery systems. Drug Discovery Today. 25:209–222.

Korsmeyer, R.W., Gurny, R., Doelker, E., Buri, P. & Peppas, N.A. 1983. Mechanisms of solute release from porous hydrophilic polymers. International Journal of Pharmaceutics. 15:25–35.

Kumari, A., Yadav, S.K. & Yadav, S.C. 2010. Biodegradable polymeric nanoparticles based drug delivery systems. Colloids and Surfaces B: Biointerfaces. 75:1–18.

Kupnik, K., Primožič, M., Kokol, V. & Leitgeb, M. 2020. Nanocellulose in drug delivery and antimicrobially active materials. Polymers. 12:1–40.

Lavoine, N., Desloges, I., Dufresne, A. & Bras, J. 2012. Microfibrillated cellulose - Its barrier properties and applications in cellulosic materials: A review. Carbohydrate Polymers. 90:735–764.

Lee, K.Y., Jang, G.H., Byun, C.H., Jeun, M., Searson, P.C. & Lee, K.H. 2017. Zebrafish models for functional and toxicological screening of nanoscale drug delivery systems: promoting preclinical applications. Bioscience Reports. 37:1–13.:

Li, H.L., Zhao, X. bin, Ma, Y.K., Zhai, G.X., Li, L.B. & Lou, H.X. 2009. Enhancement of gastrointestinal absorption of quercetin by solid lipid nanoparticles. Journal of Controlled Release. 133:238–244.

Li, M.C., Wu, Q., Song, K., Lee, S., Qing, Y. & Wu, Y. 2015. Cellulose Nanoparticles: Structure-Morphology-Rheology Relationships. ACS Sustainable Chemistry and Engineering. 3:821–832.

Li, X., Liu, Y., Yu, Y., Chen, W., Liu, Y. & Yu, H. 2019. Nanoformulations of quercetin and cellulose nanofibers as healthcare supplements with sustained antioxidant activity. Carbohydrate Polymers. 207:160–168.

Lie, E., Ålander, E. & Lindström, T. 2017. Possible toxicological effects of nanocellulose - An updated literature study, No 2. Innventia Report No. 916. 1–12.

Lieschke, G.J. & Currie, P.D. 2007. Animal models of human disease: Zebrafish swim into view. Nature Reviews Genetics. 8:352–367.

Liu, Q., Che, M., Huang, R., Ding, G., Qi, W., He, Z. & Su, R. 2021. Quercetin Enhanced Cellulose Nanocrystals for the Removal of Harmful Algae Phaeocystis Globosa. Chemical Engineering Transactions. 88:1039–1044.

Löbmann, K. & Svagan, A.J. 2017. Cellulose nanofibers as excipient for the delivery of poorly soluble drugs. International Journal of Pharmaceutics. 533:285–297.

Lu, P. & Hsieh, Y. lo. 2012. Preparation and characterization of cellulose nanocrystals from rice straw. Carbohydrate Polymer. 87:564–573.

Lunardi, V.B., Soetaredjo, F.E., Putro, J.N., Santoso, S.P., Yuliana, M., Sunarso, J., Ju, Y.-H., Ismadji, S., et al. 2021. Nanocelluloses: Sources, Pretreatment, Isolations, Modification, and Its Application as the Drug Carriers. Polymers. 13:2052.

Lundqvist, M., Stigler, J., Elia, G., Lynch, I., Cedervall, T. & Dawson, K.A. 2008. Nanoparticle size and surface properties determine the protein corona with possible implications for biological impacts. Proceedings of the National Academy of Sciences of the United States of America. 105:14265–14270.

Lundqvist, M., Augustsson, C., Lilja, M., Lundkvist, K., Dahlbäck, B., Linse, S. & Cedervall, T. 2017. The nanoparticle protein corona formed in human blood or human blood fractions. PLoS ON. 12:1–15.

Macchione, M.A., Biglione, C. & Strumia, M. 2018. Design, synthesis and architectures of hybrid nanomaterials for therapy and diagnosis applications. Polymers. 10:1–34.

Mahon, E., Salvati, A., Baldelli Bombelli, F., Lynch, I. & Dawson, K.A. 2012. Designing the nanoparticle-biomolecule interface for "targeting and therapeutic delivery." Journal of Controlled Release. 161:164–174.

McGrath, P. & Li, C.Q. 2008. Zebrafish: a predictive model for assessing drug-induced toxicity. Drug Discovery Today. 13:394–401.

Meerum Terwogt, J.M., Ten, W.W., Huinink, B., Schellens, J.H., Schot, M., Mandjes, I.A., Zurlo, M.G., Rocchetti, M., et al. 2001. Phase I clinical and pharmacokinetic study of PNU166945, a novel water-soluble polymer-conjugated prodrug of paclitaxel. Anti-Cancer Drugs. 12:315–323.

Menas A.L., Yanamala, N., Farcas, M.T., Russo, M., Friend, S., Fournier, P.M., Star, A., Iavicoli, I., Shurin, G.V., Vogel, U.B., Fadeel, B., Beezhold, D., Kisin, E.R. & Shvedova, A.A. 2017. Fibrillar vs crystalline nanocellulose pulmonary epithelial cell responses: Cytotoxicity or inflammation? Chemosphere. 171: 671–680

Modi, S. & Anderson, B.D. 2013. Determination of Drug Release Kinetics from Nanoparticles: Overcoming Pitfalls of the Dynamic Dialysis Method. Molecular Pharmaceutics. 10:3076–3089.

Moghimi, S.M., Hedeman, H., Muir, I.S., Ilium, L. & Davis, S.S. 1993. An investigation of the filtration capacity and the fate of large filtered sterically-stabilized microspheres in rat spleen. Biochimica et Biophysica Acta. 1157:233–240.

Montgomery, D.C. 2012. Design and analysis of experiments. 8th ed. Hoboken, NJ: John Wiley & Sons, Ltd.

Moon, R.J., Martini, A., Nairn, J., Simonsen, J. & Youngblood, J. 2011. Cellulose nanomaterials review: Structure, properties and nanocomposites. Chemical Society Reviews. 40:3941–3994.

Moon, R.J., Schueneman, G.T. & Simonsen, J. 2016. Overview of Cellulose Nanomaterials, Their Capabilities and Applications. JOM. 68:2383–2394.

Mosier, N., Wyman, C., Dale, B., Elander, R., Lee, Y.Y., Holtzapple, M. & Ladisch, M. 2005. Features of promising technologies for pretreatment of lignocellulosic biomass. Bioresource Technology. 96:673–686.

Müller, L.K., Simon, J., Rosenauer, C., Mailänder, V., Morsbach, S. & Landfester, K. 2018. The Transferability from Animal Models to Humans: Challenges Regarding Aggregation and Protein Corona Formation of Nanoparticles. Biomacromolecules. 19:374–385.

Myers, R.H, Montgomery, D.C. & Anderson-Cook, C.M. 2009. Response Surface Methodology. 3rd ed. Hoboken, NJ: John Wiley & Sons, Ltd.

Nasevicius, A. & Ekker, S.C. 2000. Effective targeted gene "knockdown" in zebrafish. Nature Genetics. 26:216–220.

NIST & SEMATECH. e-Handbook of Statistical Methods. Available: https://www.itl.nist.gov/div898/handbook/ [Accessed July 2022].

Owida, H.A., Al-Nabulsi, J.I., Alnaimat, F., Al Sharah, A., Al-Ayyad, M., Turab, N.M. & Abdullah, M. 2022. Advancement of Nanofibrous Mats and Common Useful Drug Delivery Applications. Advances in Pharmacological and Pharmaceutical Sciences. 2022:1–14.

Pachuau, L. 2017. Application of Nanocellulose for Controlled Drug Delivery. In Nanocellulose and Nanohydrogel Matrices. Hoboken, NJ: John Wiley & Sons, Ltd. 1–19.

Padalkar, S., Capadona, J.R., Rowan, S.J., Weder, C., Won, Y.-H., Stanciu, L.A. & Moon, R.J. 2010. Natural Biopolymers: Novel Templates for the Synthesis of Nanostructures. Langmuir. 26:8497–8502.

Pal, S. & Saha, C. 2017. Solvent effect in the synthesis of hydrophobic drug-loaded polymer nanoparticles. IET Nanobiotechnology. 11:443–447.

Penfold, J., Tucker, I., Petkov, J. & Thomas, R.K. 2007. Surfactant Adsorption onto Cellulose Surfaces. Langmuir. 23:8357–8364.

Peng, Y., Gardner, D.J. & Han, Y. 2012. Drying cellulose nanofibrils: In search of a suitable method. Cellulose. 19:91–102.

Peterson, R.T. & MacRae, C.A. 2012. Systematic approaches to toxicology in the zebrafish. Annual Review of Pharmacology and Toxicology. 52:433–453.

Pinto, F., Lourenço, A.F., Pedrosa, J.F.S., Gonçalves, L., Ventura, C., Vital, N., Bettencourt, A., Fernandes, S.N., et al. 2022. Analysis of the In Vitro Toxicity of Nanocelluloses in Human Lung Cells as Compared to Multi-Walled Carbon Nanotubes. Nanomaterials. 12:1432.

Poletto, M., Ornaghi Júnior, H.L. & Zattera, A.J. 2014. Native cellulose: Structure, characterization and thermal properties. Materials. 7:6105–6119.

Priyadarsini, K.I. 2014. The chemistry of curcumin: From extraction to therapeutic agent. Molecules. 19:20091–20112.

Qing, W., Wang, Y., Wang, Y., Zhao, D., Liu, X. & Zhu, J. 2016. The modified nanocrystalline cellulose for hydrophobic drug delivery. Applied Surface Science. 366:404–409.

Qu, J., Yuan, Z., Wang, C., Wang, A., Liu, X., Wei, B. & Wen, Y. 2019. Enhancing the redispersibility of TEMPO-mediated oxidized cellulose nanofibrils in N,Ndimethylformamide by modification with cetyltrimethylammonium bromide. Cellulose. 26:7769–7780.

Raghav, N., Mor, N., Gupta, R.D., Kaur, R., Sharma, M.R. & Arya, P. 2020. Some cetyltrimethylammonium bromide modified polysaccharide supports as sustained release systems for curcumin. International Journal of Biological Macromolecules. 154:361–370.

Raghav, N., Sharma, M.R. & Kennedy, J.F. 2021. Nanocellulose: A mini-review on types and use in drug delivery systems. Carbohydrate Polymer Technologies and Applications. 2:1–10.

Rattaz, A., Mishra, S.P., Chabot, B. & Daneault, C. 2011. Cellulose nanofibres by sonocatalysed-TEMPO-oxidation. Cellulose. 18:585–593.

Razmara, R.S., Daneshfar, A. & Sahraei, R. 2010. Solubility of Quercetin in Water + Methanol and Water + Ethanol from (292.8 K to 333.8 K). Journal of Chemical and Engineering Data. 55:3934–3936.

Roman, M., Dong, S., Hirani, A. & Lee, Y.W. 2010. Cellulose nanocrystals for drug delivery. Polysaccharide Materials: Performance by Design. ACS Symposium Series. V. 1017. K. Edgar et al, Eds. Washington, DC: American Chemical Society.

Romberg, B., Hennink, W.E. & Storm, G. 2008. Expert Review Sheddable Coatings for Long-Circulating Nanoparticles. Pharmaceutical Research. 25:55–71.

Rosen, J.N., Sweeney, M.F. & Mably, J.D. 2009. Microinjection of zebrafish embryos to analyze gene function. Journal of Visualized Experiments. 25:1–4.

Rossi, M., Rickles, L.F. & Halpin, W.A. 1986. The Crystal and Molecular Structure of Quercetin: A Biologically Active and Naturally Occurring Flavonoid. Bioorganic Chemistry. 14:55–69.

Rothwell, J.A., Day, A.J. & Morgan, M.R.A. 2005. Experimental Determination of Octanol−Water Partition Coefficients of Quercetin and Related Flavonoids. Journal of Agricultural and Food Chemistry. 53:4355–4360.

Roy, D., Semsarilar, M., Guthrie, J.T. & Perrier, S. 2009. Cellulose modification by polymer grafting: A review. Chemical Society Reviews. 38:2046–2064.

Santoriello, C. & Zon, L.I. 2012. Hooked! modeling human disease in zebrafish. Journal of Clinical Investigation. 122:2337–2343.

Selvaraj, S., Shanmugasundaram, S., Maruthamuthu, M., Venkidasamy, B. & Shanmugasundaram, S. 2021. Facile Synthesis and Characterization of Quercetin-Loaded Alginate Nanoparticles for Enhanced In Vitro Anticancer Effect Against Human Leukemic Cancer U937 Cells. Journal of Cluster Science. 32:1507–1518.

Shaikh, H.K., Kshirsagar, R. v & Patil, S.G. 2015. Mathermatical models for drug release and characterisation: A review. World Journal of Pharmacy and Pharmaceutical Sciences. 4:324–338.

Shang, Z., An, X., Seta, F.T., Ma, M., Shen, M., Dai, L., Liu, H. & Ni, Y. 2019. Improving dispersion stability of hydrochloric acid hydrolyzed cellulose nano-crystals. Carbohydrate Polymers. 222:1–6.

Shen, J. & Burgess, D.J. 2013. In vitro dissolution testing strategies for nanoparticulate drug delivery systems: recent developments and challenges. Drug Delivery and Translational Research. 3:409–415.

Sieber, S., Grossen, P., Bussmann, J., Campbell, F., Kros, A., Witzigmann, D. & Huwyler, J. 2019. Zebrafish as a preclinical in vivo screening model for nanomedicines. Advanced Drug Delivery Reviews. 151–152:152–168.

Siepmann, J. & Siepmann, F. 2009. Modern Pharmaceutics: Application and Advances. 5th ed. V. 2. A.T. Florence & J. Siepmann, Eds. New York: Informa Healthcare.

Silva, A.M., Alvarado, H.L., Abrego, G., Martins-Gomes, C., Garduño-Ramirez, M.L., García, M.L., Calpena, A.C. & Souto, E.B. 2019. In Vitro Cytotoxicity of Oleanolic/Ursolic Acids-Loaded in PLGA Nanoparticles in Different Cell Lines. Pharmaceutics. 11:362.

Simone, E.A., Dziobla, T.D. & Muzykantov, V.R. 2008. Polymeric carriers - role of geometry in drug delivery. Expert Opinion Drug Delivery. 5:1283–1300.

Song, Y., Zhang, L., Gan, W., Zhou, J. & Zhang, L. 2011. Self-assembled micelles based on hydrophobically modified quaternized cellulose for drug delivery. Colloids and Surfaces B: Biointerfaces. 83:313–320.

Soppimath, K.S., Aminabhavi, T.M., Kulkarni, A.R. & Rudzinski, W.E. 2001. Biodegradable polymeric nanoparticles as drug delivery devices. Journal of Controlled Release. 70:1–20.

Sun, J., Wang, F., Sui, Y., She, Z., Zhai, W., Wang, C. & Deng, Y. 2012. Effect of particle size on solubility, dissolution rate, and oral bioavailability: evaluation using coenzyme Q10 as naked nanocrystals. International Journal of Nanomedicine. 7:5733–5744.

Syverud, K., Xhanari, K., Chinga-Carrasco, G., Yu, Y. & Stenius, P. 2011. Films made of cellulose nanofibrils: Surface modification by adsorption of a cationic surfactant and characterization by computer-assisted electron microscopy. Journal of Nanoparticle Research. 13:773–782.

Taguchi, G. 1987. System of Experimental Design: Engineering Methods to Optimize Quality and Minimize Cost. White Plains, NY: UNIPUB.

Tardy, B.L., Yokota, S., Ago, M., Xiang, W., Kondo, T., Bordes, R. & Rojas, O.J. 2017. Nanocellulose–surfactant interactions. Current Opinion in Colloid and Interface Science. 29:57–67.

Thoorens, G., Krier, F., Leclercq, B., Carlin, B. & Evrard, B. 2014. Microcrystalline cellulose, a direct compression binder in a quality by design environment - A review. International Journal of Pharmaceutics. 473:64–72.

Wagner, V., Dullaart, A., Bock, A.-K. & Zweck, A. 2006. The emerging nanomedicine landscape. Nature Biotechnology. 24:1211–1217.

Wallace, S.J., Li, J., Nation, R.L. & Boyd, B.J. 2013. Drug release from nanomedicines: Selection of appropriate encapsulation and release methodology. Drug Delivery and Translational Research. 2:284–292.

Wang, J. & Zhao, Xi.H. 2016. Degradation kinetics of fisetin and quercetin in solutions affected by medium pH, temperature and co-existing proteins. Journal of the Serbian Chemical Society. 81:243–253.

Wang, Y., Li, P., Tran, T.T.D., Zhang, J. & Kong, L. 2016. Manufacturing techniques and surface engineering of polymer based nanoparticles for targeted drug delivery to cancer. Nanomaterials. 6:1–18.

Weng, J., Tong, H.H.Y. & Chow, S.F. 2020. In Vitro Release Study of the Polymeric Drug Nanoparticles: Development and Validation of a Novel Method. Pharmaceutics. 12:732.

White, R.M., Sessa, A., Burke, C., Bowman, T., LeBlanc, J., Ceol, C., Bourque, C., Dovey, M., et al. 2008. Transparent Adult Zebrafish as a Tool for In Vivo Transplantation Analysis. Cell Stem Cell. 2:183–189.

van Wijk, R.C., Krekels, E.H.J., Hankemeier, T., Spaink, H.P. & van der Graaf, P.H. 2016. Systems pharmacology of hepatic metabolism in zebrafish larvae. Drug Discovery Today: Disease Models. 22:27–34.

Williams, G.R., Raimi-Abraham, B.T. & Luo, C.J. 2018. Nanofibers in Drug Delivery. London: UCL Press. 1–23.

Wohlhauser, S., Delepierre, G., Labet, M., Gaëlle Morandi, Thielemans, W., Weder, C. & Zoppe, J.O. 2018. Grafting Polymers from Cellulose Nanocrystals: Synthesis, Properties, and Applications. Macromolecules. 51:6157–6189.

Xhanari, K., Syverud, K., Chinga-Carrasco, G., Paso, K. & Stenius, P. 2011. Reduction of water wettability of nanofibrillated cellulose by adsorption of cationic surfactants. Cellulose. 18:257–270.

Yahya, M., Chen, Y.W., Lee. H.V., Hock, C.C. & Hassan, W.H.W. 2019. A New Protocol for Efficient and High Yield Preparation of Nanocellulose from Elaeis guineensis Biomass: A Response Surface Methodology (RSM). Journal of Polymers and the Environment. 27:678–702.

Yu, M., Yuan, W., Li, D., Schwendeman, A. & Schwendeman, S.P. 2019. Predicting drug release kinetics from nanocarriers inside dialysis bags. Journal of Controlled Release. 315:23–30.

Zainuddin, N., Ahmad, I., Kargarzadeh, H. & Ramli, S. 2017. Hydrophobic kenaf nanocrystalline cellulose for the binding of curcumin. Carbohydrate Polymers. 163:261–269.

Zalipsky, S. & Milton Harris, J. 1997. Introduction to Chemistry and Biological Applications of Poly (ethylene glycol). In Poly(ethylene glycol): Chemistry and Biological Applications. Washington, DC: American Chemical Society. Symposium Series. 1–13.

Zhang, X., Yang, W. & Blasiak, W. 2011. Modeling study of woody biomass: Interactions of cellulose, hemicellulose, and lignin. Energy and Fuels. 25:4786–4795.

Zhang, Y., Yang, Y., Tang, K., Hu, X. & Zou, G. 2008. Physicochemical characterization and antioxidant activity of quercetin-loaded chitosan nanoparticles. Journal of Applied Polymer Science. 107:891–897.

Zheng, M., Li, Z. & Huang, X. 2004. Ethylene glycol monolayer protected nanoparticles: Synthesis, characterization, and interactions with biological molecules. Langmuir. 20:4226–4235.

Zheng, T., Bott, S. & Huo, Q. 2016. Techniques for Accurate Sizing of Gold Nanoparticles Using Dynamic Light Scattering with Particular Application to Chemical and Biological Sensing Based on Aggregate Formation. Applied Materials & Interfaces. 8:21585–21594.

Zhou, Y., He, C., Chen, K., Ni, J., Cai, Y., Guo, X. & Wu, X.Y. 2016. A New Method for Evaluating Actual Drug Release Kinetics of Nanoparticles inside Dialysis Devices via Numerical Deconvolution. Journal of Controlled Release. 243:11–20.

Zielinska, A., Carreiró, F., Oliveira, A.M., Neves, A., Pires, B., Nagasamy Venkatesh, D., Durazzo, A., Lucarini, M., et al. 2020. Polymeric Nanoparticles: Production, Characterization, Toxicology and Ecotoxicology. Molecules. 25:1–20.

Appendix A: Experimental methods

Figure A.1: Quercetin (5.5 mg/mL) solubilised in 75 wt% ethanol (left) and distilled water (right)

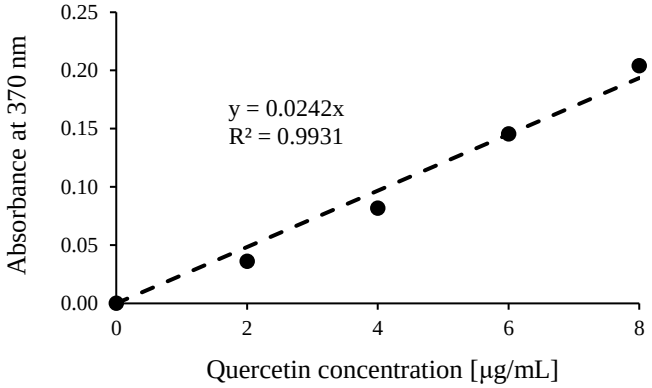

Figure A.2: Calibration curve produced for the absorbance of quercetin at 370 nm, used to calculate binding efficiency (BE) for the experimental design

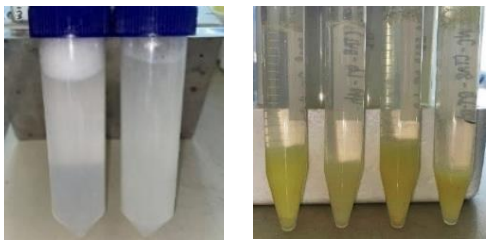

Figure A.3: Prepared cellulose nanocrystals (CNC) and cellulose nanofibrils (CNF) 0.4 wt% suspensions (left), and their respective formulations with surfactant (CTAB) and quercetin (right)

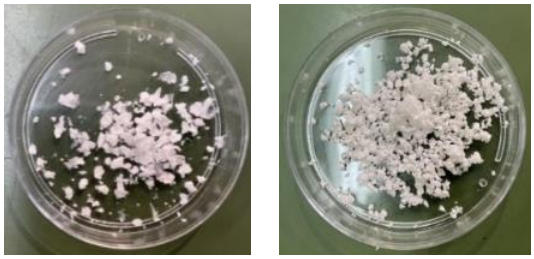

Figure A.4: Freeze-dried cellulose nanocrystals (CNC) and cellulose nanofibrils (CNF)

Appendix B: Experimental design analysis

Table B.1: Coded and uncoded full design matrix, with the corresponding response values recorded at each factor combination, for each experimental run in the cellulose nanocrystals (CNC) system

Space		Run	Factor				Response			
			X_1	X_2	CTAB (mM)	QT (mg/mL)	Z (nm)	PdI	Zeta (mV)	BE (%)
1	F	1	-1	-1	2	1	6022	0.32	-32.6	40.9
1	F	2	-1	-1	2	1	5080	1.00	-38.0	29.5
1	F	3	-1	-1	2	1	9111	0.05	-31.2	36.0
1	F	4	1	-1	6	1	3261	1.00	-23.1	43.5
1	F	5	1	-1	6	1	5610	0.62	-13.9	60.3
1	F	6	1	-1	6	1	3599	0.54	-12.9	30.6
1	F	7	-1	1	2	10	2918	1.00	-22.2	97.6
1	F	8	-1	1	2	10	3785	1.00	-19.6	91.0
1	F	9	-1	1	2	10	3581	1.00	-14.5	90.8
1	F	10	1	1	6	10	6010	0.94	-16.0	99.3
1	F	11	1	1	6	10	2647	0.74	-15.3	96.8
1	F	12	1	1	6	10	2467	0.31	-20.4	97.2
1	C	13	0	0	4	5.5	3266	0.52	-15.9	88.7
1	C	14	0	0	4	5.5	2658	1.00	-17.2	86.0
1	C	15	0	0	4	5.5	3102	0.70	-23.6	86.9
2	A	16	-1	0	2	5.5	4492	0.76	-20.7	89.7
2	A	17	-1	0	2	5.5	7768	1.00	-17.2	90.4
2	A	18	-1	0	2	5.5	8646	1.00	-19.5	92.5
2	A	19	1	0	6	5.5	6261	1.00	-16.0	90.9
2	A	20	1	0	6	5.5	9107	1.00	-14.2	88.7
2	A	21	1	0	6	5.5	5917	0.88	-13.2	92.0
2	A	22	0	-1	4	1	7202	0.11	-21.7	54.1
2	A	23	0	-1	4	1	7078	0.34	-22.0	47.5
2	A	24	0	-1	4	1	9881	0.47	-11.8	47.9
2	A	25	0	1	4	10	6350	0.97	-7.0	95.8
2	A	26	0	1	4	10	5798	0.92	-8.6	94.0
2	A	27	0	1	4	10	4100	0.66	-9.7	96.9
2	C	28	0	0	4	5.5	8099	0.02	-12.2	87.0
2	C	29	0	0	4	5.5	5512	0.29	-5.8	81.9
2	C	30	0	0	4	5.5	6665	0.68	-9.4	83.3

1 = Block 1; 2 = Block 2; F = Factorial; C = Centre; A = Axial

Table B.2: Coded and uncoded full design matrix, with the corresponding response values recorded at each factor combination, for each experimental run in the cellulose nanofibrils (CNF) system

Space		Run	Factor				Response			
			X_1	X_2	CTAB (mM)	QT (mg/mL)	Z (nm)	PdI	Zeta (mV)	BE (%)
1	F	1	-1	-1	2	1	5278	0.51	-24.7	20.2
1	F	2	-1	-1	2	1	5587	1.00	-25.9	42.1
1	F	3	-1	-1	2	1	4515	0.37	-27.2	26.0
1	F	4	1	-1	6	1	5286	0.92	-17.4	24.4
1	F	5	1	-1	6	1	3071	0.53	-3.7	36.0
1	F	6	1	-1	6	1	3584	1.00	-9.4	26.0
1	F	7	-1	1	2	10	4263	1.00	-13.4	95.0
1	F	8	-1	1	2	10	3452	1.00	-15.4	91.2
1	F	9	-1	1	2	10	2924	0.88	-11.5	90.6
1	F	10	1	1	6	10	5984	1.00	-8.3	98.4
1	F	11	1	1	6	10	2975	0.67	-16.3	97.7
1	F	12	1	1	6	10	4187	0.86	-11.2	98.3
1	C	13	0	0	4	5.5	5726	1.00	-13.1	87.9
1	C	14	0	0	4	5.5	3224	0.50	-13.7	88.2
1	C	15	0	0	4	5.5	2726	0.56	-15.3	85.0
2	A	16	-1	0	2	5.5	6782	0.85	-4.6	93.0
2	A	17	-1	0	2	5.5	2991	0.42	-8.2	92.1
2	A	18	-1	0	2	5.5	4128	0.40	-6.8	94.1
2	A	19	1	0	6	5.5	4284	0.59	5.2	92.7
2	A	20	1	0	6	5.5	5052	0.21	3.3	92.3
2	A	21	1	0	6	5.5	4494	0.18	-3.7	94.9
2	A	22	0	-1	4	1	2659	0.77	-2.4	71.9
2	A	23	0	-1	4	1	7588	0.41	-12.5	74.4
2	A	24	0	-1	4	1	3920	0.68	-9.8	67.8
2	A	25	0	1	4	10	5538	0.95	0.7	94.7
2	A	26	0	1	4	10	5175	0.75	-1.2	93.8
2	A	27	0	1	4	10	4510	0.74	2.5	96.7
2	C	28	0	0	4	5.5	3860	0.43	-10.0	84.7
2	C	29	0	0	4	5.5	2243	1.00	-7.1	84.1
2	C	30	0	0	4	5.5	3020	0.64	-15.2	83.2

1 = Block 1; 2 = Block 2; F = Factorial; C = Centre; A = Axial

Table B.3: ANOVA tables for the quadratic models fitted to mean hydrodynamic diameter (Z), polydispersity index (PdI), zeta potential (ζ), and binding efficiency (BE) for cellulose nanocrystals (CNC)

Response	Source	DF	Adj SS	Adj MS	F-Value	P-Value
Z	CTAB	1	2364588	2364588	1.08	0.310
	CTAB*CTAB	1	3585174	3585174	1.63	0.214
	QT	1	20454408	20454408	9.32	0.006
	QT*QT	1	1359456	1359456	0.62	0.439
	CTAB*QT	1	6138991	6138991	2.80	0.108
	Lack of fit	3	2955126	985042	0.41	0.744
	Pure error	20	47535632	2376782		
	Total	29	137085977			
PdI	CTAB	1	0.0006	0.0006	0.01	0.931
	CTAB*CTAB	1	0.3873	0.3873	4.98	0.036
	QT	1	0.5233	0.5233	6.73	0.016
	QT*QT	1	0.0659	0.0659	0.85	0.367
	CTAB*QT	1	0.2706	0.2706	3.48	0.075
	Lack of fit	3	0.4777	0.1592	2.43	0.095
	Pure error	20	1.3118	0.0656		
	Total	29	3.0508			
Zeta potential	CTAB	1	276.13	276.13	18.55	0.000
	CTAB*CTAB	1	94.28	94.28	6.33	0.019
	QT	1	303.65	303.65	20.40	0.000
	QT*QT	1	2.35	2.349	0.16	0.695
	CTAB*QT	1	186.44	186.44	12.52	0.002
	Lack of fit	3	71.35	23.78	1.75	0.188
	Pure error	20	271.04	13.55		
	Total	29	1589.79			
Binding efficiency	CTAB	1	94.20	94.20	2.54	0.125
	CTAB*CTAB	1	3.40	3.40	0.09	0.766
	QT	1	12233.40	12233.40	329.56	0.000
	QT*QT	1	1778.00	1778.00	47.90	0.000
	CTAB*QT	1	16.40	16.40	0.44	0.513
	Lack of fit	1	249.70	83.20	2.76	0.069
	Pure error	3	604.10	30.20		
	Total	20	15807.40			

Table B.4: ANOVA tables for the quadratic models fitted to mean hydrodynamic diameter (Z), polydispersity index (PdI), zeta potential (ζ), and binding efficiency (BE) for cellulose nanofibrils (CNF)

Response	Source	DF	Adj SS	Adj MS	F-Value	P-Value
Z	CTAB	1	55889	55889	0.03	0.863
	CTAB*CTAB	1	341689	341689	0.19	0.670
	QT	1	744692	744692	0.41	0.531
	QT*QT	1	2372337	2372337	1.29	0.267
	CTAB*QT	1	2946243	2946243	1.60	0.218
	Lack of fit	3	5431327	1810442	0.98	0.420
	Pure error	20	36810112	1840506		
	Total	29	49101803			
PdI	CTAB	1	0.0115	0.0115	0.22	0.642
	CTAB*CTAB	1	0.1524	0.1524	2.96	0.099
	QT	1	0.0702	0.0702	1.37	0.255
	QT*QT	1	0.1649	0.1649	3.21	0.087
	CTAB*QT	1	0.0715	0.0715	1.39	0.251
	Lack of fit	3	0.1294	0.0431	0.82	0.499
	Pure error	20	1.0538	0.0527		
	Total	29	1.9130			
Zeta potential	CTAB	1	321.82	321.82	17.09	0.000
	CTAB*CTAB	1	192.72	192.72	10.24	0.004
	QT	1	16.17	16.17	0.86	0.364
	QT*QT	1	0.71	0.71	0.04	0.848
	CTAB*QT	1	152.80	152.80	8.12	0.009
	Lack of fit	3	145.33	48.44	3.37	0.039
	Pure error	20	287.69	14.39		
	Total	29	1937.07			
Binding efficiency	CTAB	1	14.50	14.50	0.12	0.729
	CTAB*CTAB	1	12148.10	12148.10	102.73	0.362
	QT	1	102.20	102.20	0.86	0.000
	QT*QT	1	1194.10	1194.10	10.10	0.004
	CTAB*QT	1	32.10	32.10	0.27	0.607
	Lack of fit	3	2332.40	777.50	40.13	0.000
	Pure error	20	387.50	19.40		
	Total	29	19271.30			

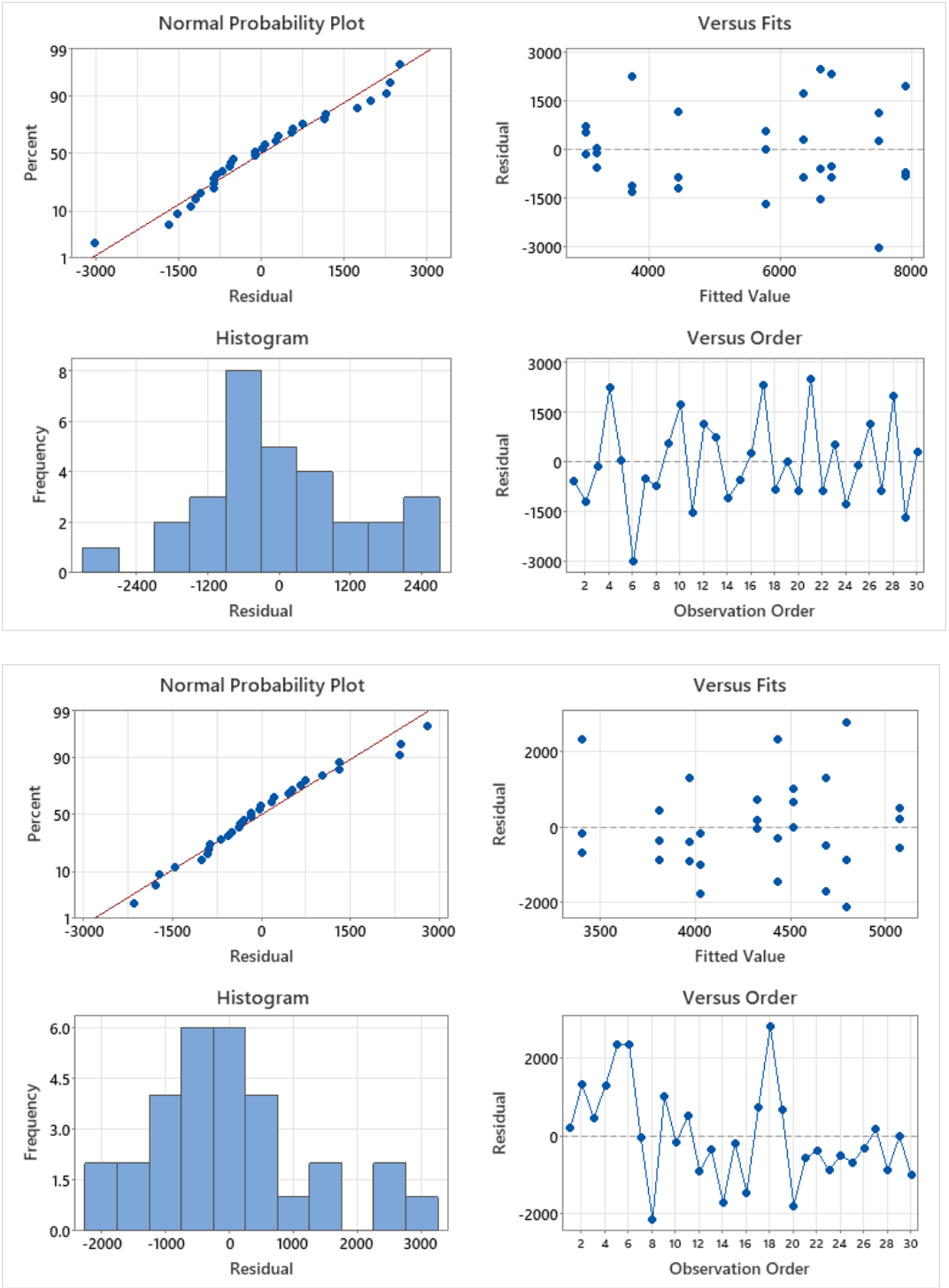

Figure B.1: Four-by-four residual plot analysis outputs for the mean hydrodyanmic daimeter (Z) of the cellulose nanocrystals (CNC) (top) and cellulose nanofibrils (CNF) (bottom) system

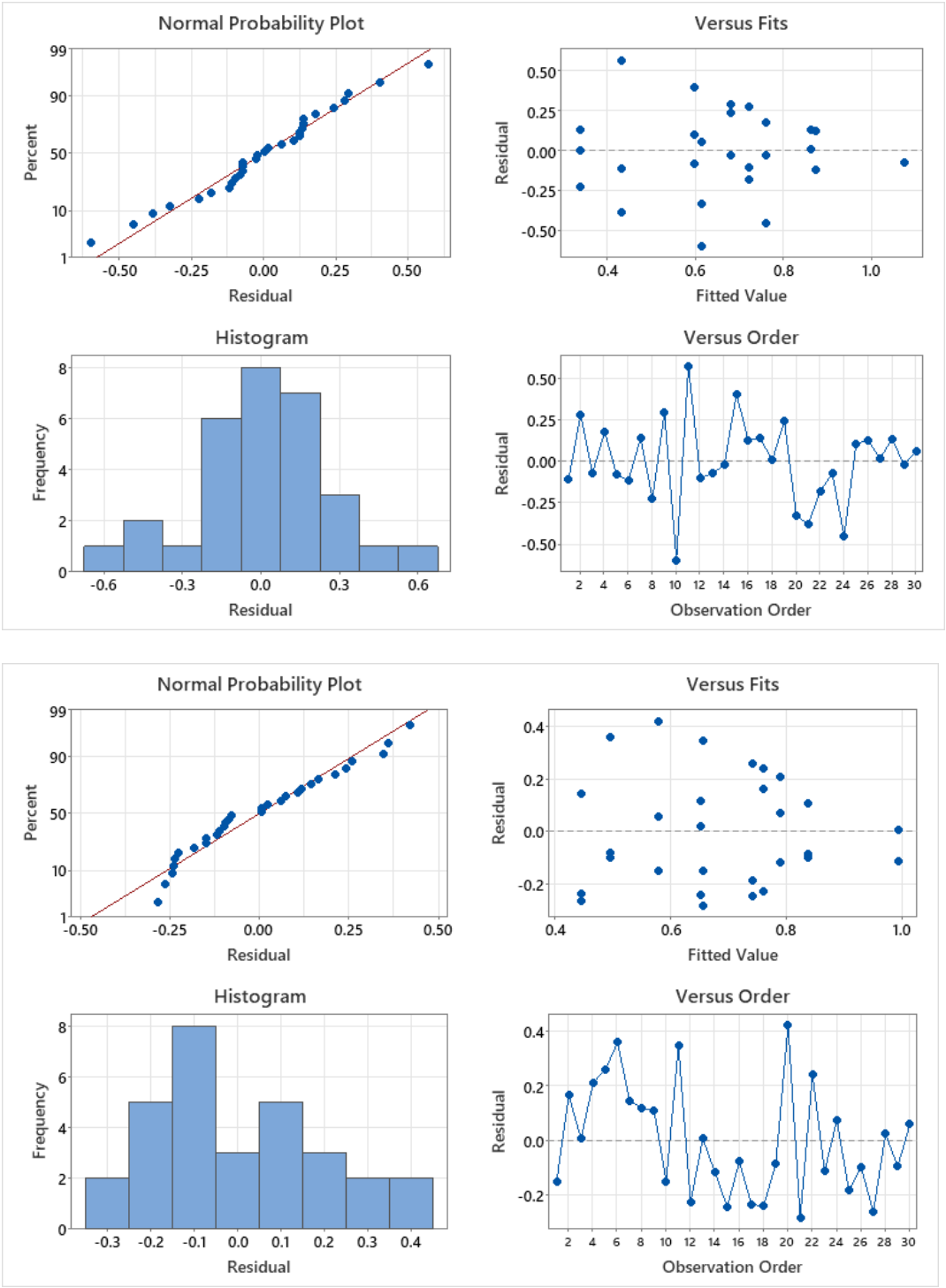

Figure B.2: Four-by-four residual plot analysis outputs for the polydispersity index (PdI) of the cellulose nanocrystals (CNC) (top) and cellulose nanofibrils (CNF) (bottom) system

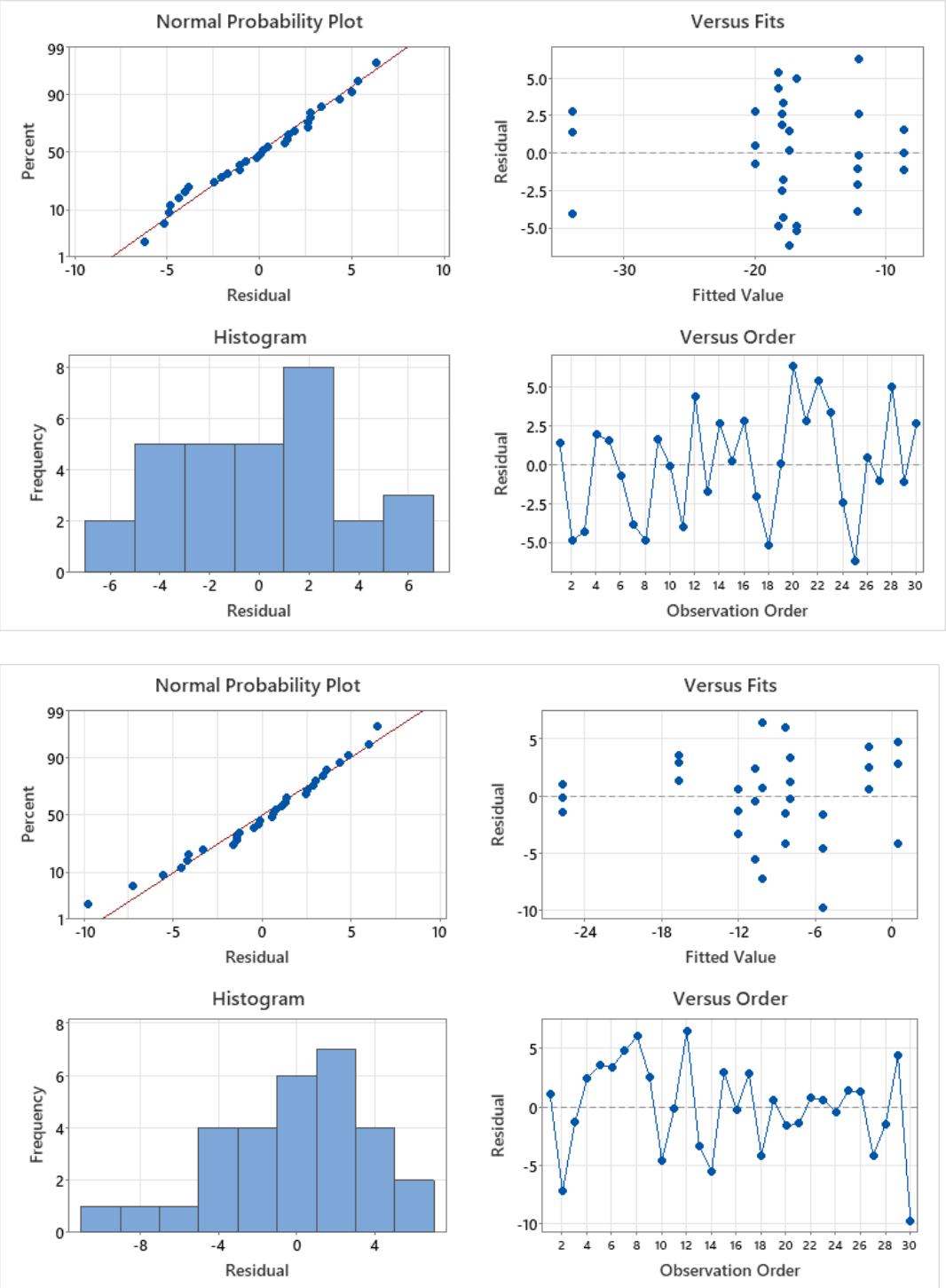

Figure B.3: Four-by-four residual plot analysis outputs for the zeta potential (ζ) of the cellulose nanocrystals (CNC) (top) and cellulose nanofibrils (CNF) (bottom) system

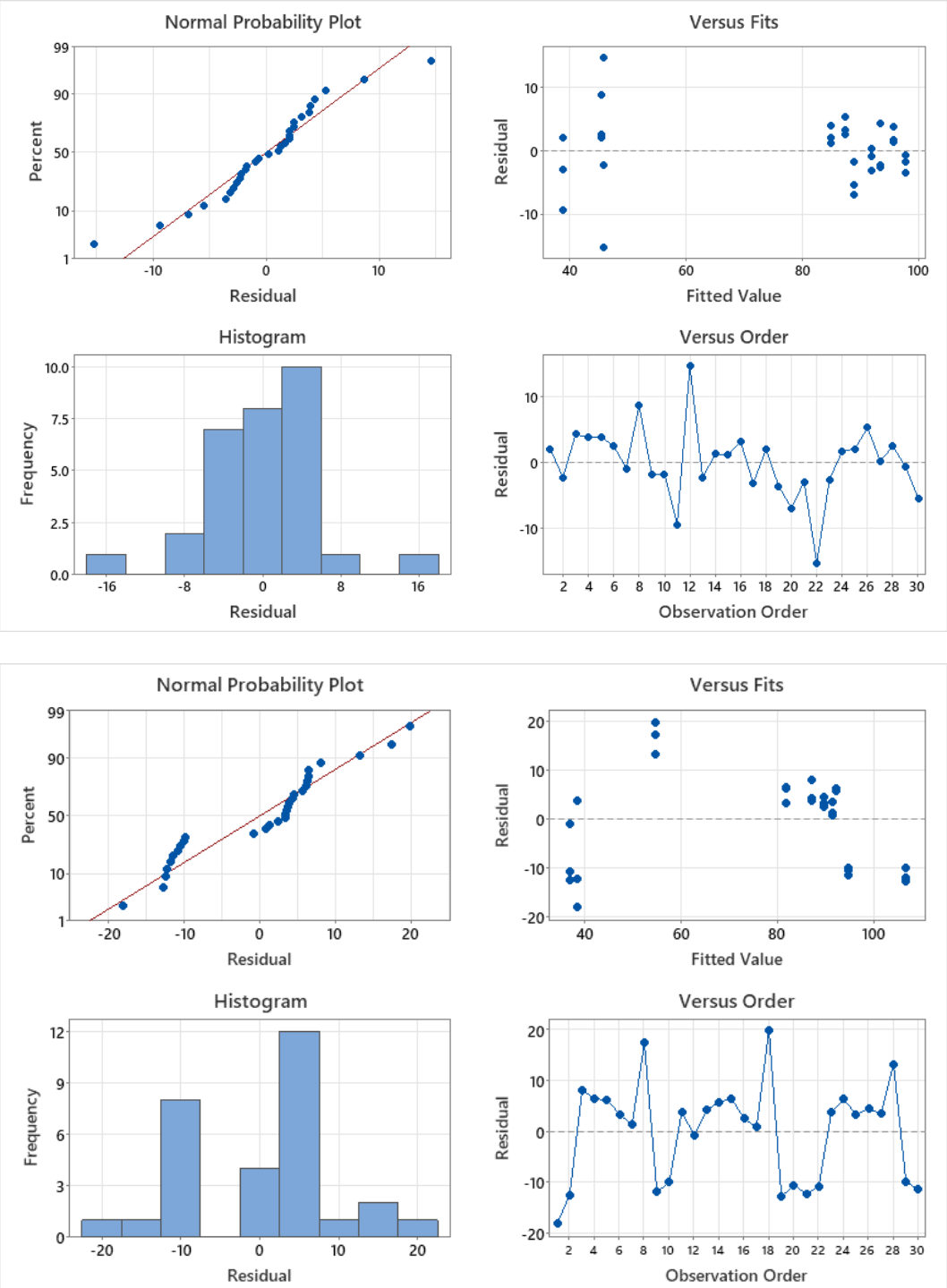

Figure B.4: Four-by-four residual plot analysis outputs for the binding efficiency (BE) of the cellulose nanocrystals (CNC) (top) and cellulose nanofibrils (CNF) (bottom) system

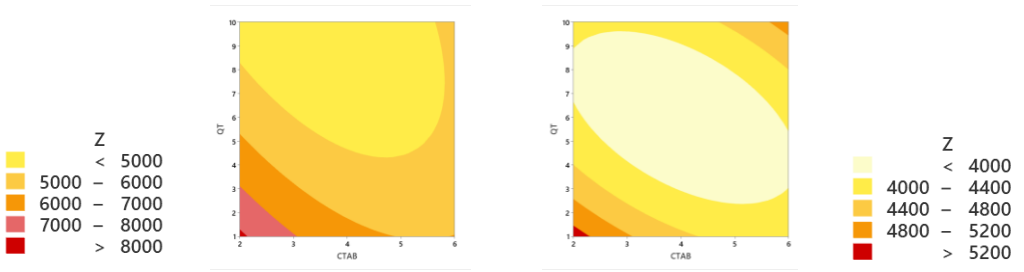

Figure B.5: Contour plots of the cellulose nanocrystals (CNC) (left) and cellulose nanofibrils (CNF) (right) predicting the mean hydrodynamic diameter (Z) with surfactant (CTAB) and quercetin (QT) concentration as independent variables

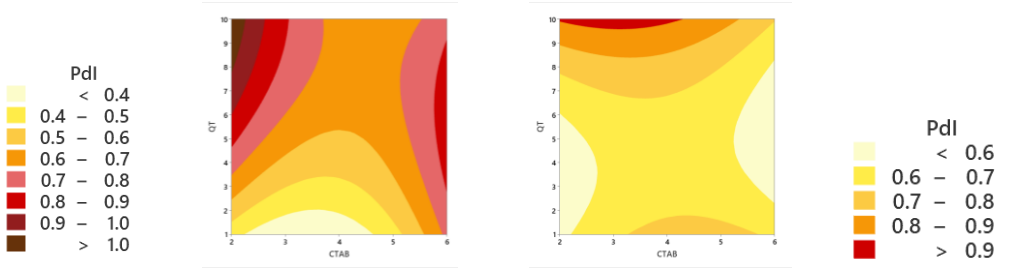

Figure B.6: Contour plots of the cellulose nanocrystals (CNC) (left) and cellulose nanofibrils (CNF) (right) predicting the polydispersity index (PdI) with surfactant (CTAB) and quercetin (QT) concentration as independent variables

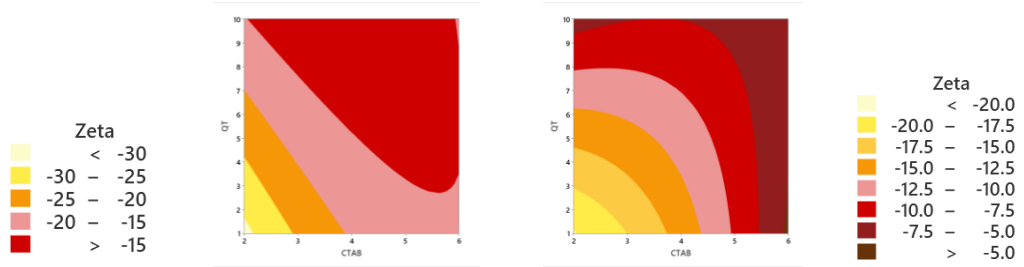

Figure B.7: Contour plots of the cellulose nanocrystals (CNC) (left) and cellulose nanofibrils (CNF) (right) predicting the zeta potential (ζ) with surfactant (CTAB) and quercetin (QT) concentration as independent variables

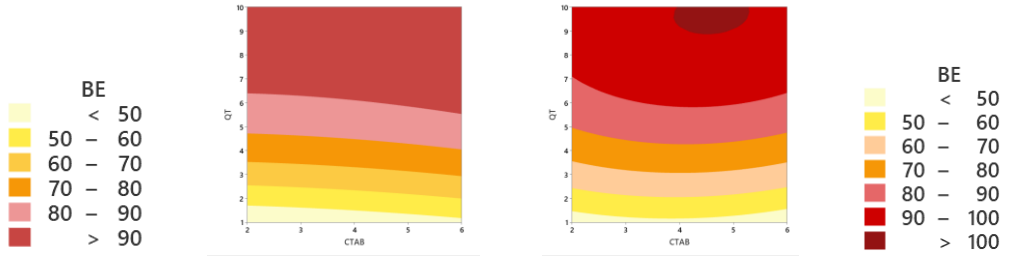

Figure B.8: Contour plots of the cellulose nanocrystals (CNC) (left) and cellulose nanofibrils (CNF) (right) predicting the binding efficiency (BE) with surfactant (CTAB) and quercetin (QT) concentration as independent variables

Appendix C: Microscopy

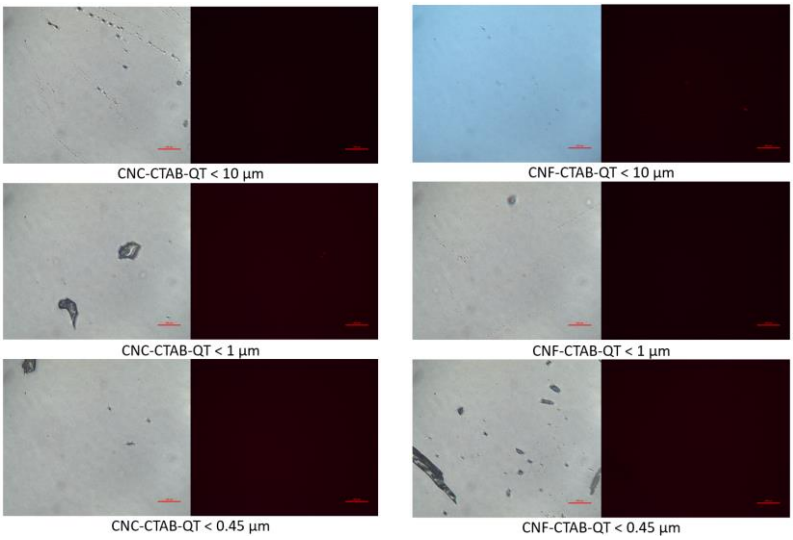

Figure C.1: Brightfield and flourescent micrographs of formulations of cellulose nanocrystals (CNC) (left) and cellulose nanofibrils (CNF) (right) with surfactant (CTAB) and quercetin (QT), filtered by 10 µm (top), 1 µm (middle) and 0.45 µm (bottom) nylon syringe filters (scale bar 100 µm)

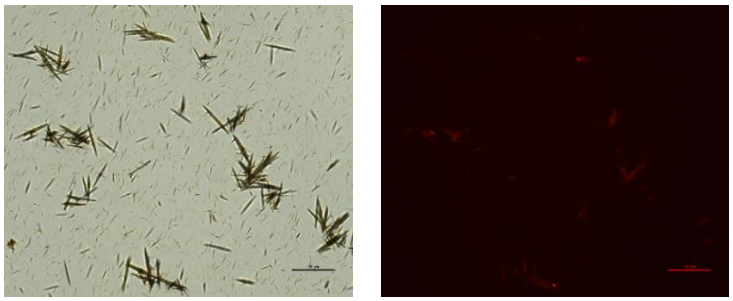

Figure C.2: Brightfield (left) and flourescent (right) micrographs of unfiltered quercetin, solubilised at 5.5 mg/mL in 75 wt% ethanol (scale bar 100 µm)

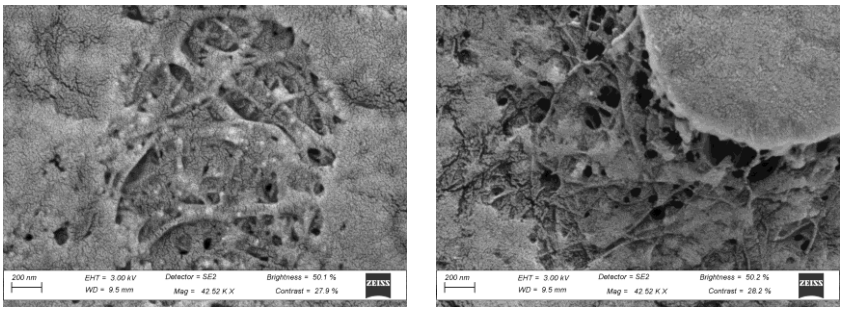

Figure C.3: SEM micrographs of an unmodified (left) and homogenised (right) 0.4 wt% cellulose nanocrystals (CNC) suspension, potentially having undergone insufficient acid hydrolysis (scale bar 200 nm)

Appendix D: Release kinetics

Table D.1: Cumulative percent release vs time data produced by dialysis bag release tests on the formulation of cellulose nanocrystals (CNC), modified at a surfactant (CTAB) and quercetin (QT) concentration of 4 mM and 5.5 mg/mL, respectively, as well as a control run performed using free QT

Time (min)	Cumulative release (%)			
	CNC-CTAB-QT		Free QT	
	μ	σ	μ	σ
0	0.0	0.0	0.0	0.0
20	3.7	2.0	8.4	2.6
40	12.7	3.3	27.6	7.0
60	29.4	4.5	62.0	11.8
80	54.1	4.5	99.3	14.1
100	78.9	4.6		

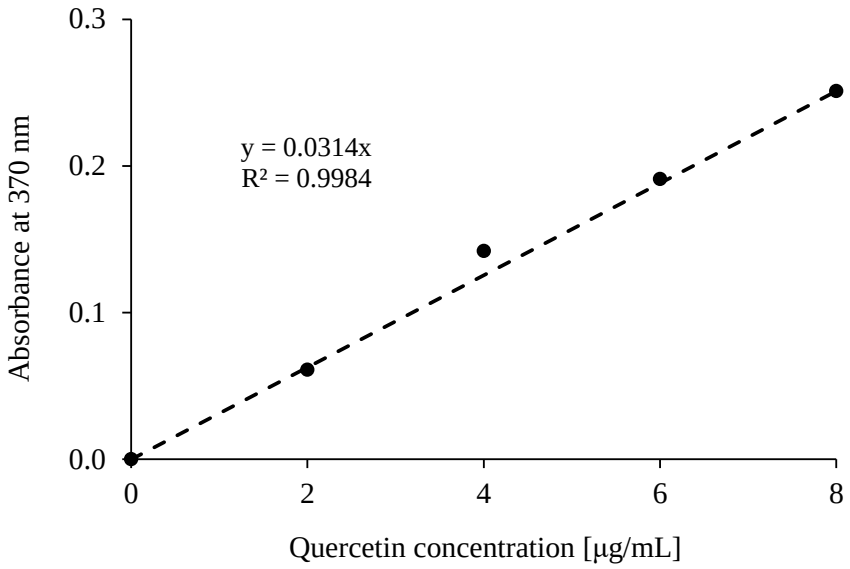

Figure D.1: Repeated calibration curve produced for the absorbance of quercetin at 370 nm, used to calculate percent release for the dialysis release tests